

DISSERTATION

STRAIN SENSORS AND CHEMIRE SISTORS MADE
FROM CROSS-LINKED GOLD NANOPARTICLES:
FABRICATION, CHARACTERIZATION AND
APPLICATIONS

Dissertation zur Erlangung des Doktorgrades
an der Fakultät für Mathematik, Informatik und
Naturwissenschaften

Fachbereich Chemie
Universität Hamburg

vorgelegt von
Bendix Ketelsen

Hamburg

2022

Dissertation

Titel:	Strain Sensors and Chemiresistors Made From Cross-Linked Gold Nanoparticles: Fabrication, Characterization and Applications
Titel (deu.):	Dehnungssensoren und Chemiresistoren aus quervernetzten Goldnanopartikeln: Herstellung, Charakterisierung und Anwendungen
Eingereicht von:	Bendix Ketelsen
Matrikelnummer:	6423829
Email:	bendix.ketelsen@gmx.net
Arbeitsgruppe:	Prof. Dr. Horst Weller
Institut:	Institut für Physikalische Chemie
Universität:	Universität Hamburg
Datum der Einreichung:	25. August 2022
Erstgutachter:	Dr. Tobias Vossmeier
Zweitgutachter:	Prof. Dr. Alf Mews
Datum der Disputation:	04. November 2022
Vorsitz d. Prüfungskommission:	Prof. Dr. Horst Weller

Diese Arbeit wurde im Zeitraum vom April 2018 bis Juni 2022 in der Arbeitsgruppe von Prof. Dr. Horst Weller, im Team von Dr. Tobias Vossmeier, am Institut für Physikalische Chemie im Fachbereich Chemie der Universität Hamburg, durchgeführt.

I List of Publications

The following list contains chronologically ordered peer-reviewed journal articles published within the framework of this research project. An equal contribution of two authors is denoted by a ‡ symbol.

1. Chun-Hao Su, Hsien-Lung Chiu, Yen-Chi Chen, Mazlum Yesilmen, Florian Schulz, Bendix Ketelsen, Tobias Vossmeier, Ying-Chih Liao, "Highly Responsive PEG/Gold Nanoparticle Thin-Film Humidity Sensor via Inkjet Printing Technology", *Langmuir* **2019**, 35, 3256–3264.

2. Bendix Ketelsen,[‡] Patrick P. Tjarks,[‡] Hendrik Schlicke, Ying-Chih Liao, Tobias Vossmeier, "Fully Printed Flexible Chemiresistors with Tunable Selectivity Based on Gold Nanoparticles", *Chemosensors* **2020**, 8, 1–14.

II Contents

I	List of Publications	vii
II	Contents	ix
III	List of Abbreviations	xiii
1	Zusammenfassung	1
2	Summary	4
3	Introduction	7
4	Objectives	9
5	Theoretical Background	11
5.1	Gold Nanoparticle Synthesis	11
5.2	Gold Nanoparticle Composite Materials	12
5.2.1	Fabrication of GNP Films	12
5.2.2	Charge Transport	17
5.2.3	Resistive Strain Sensing	20
5.2.4	Resistive Chemical Sensing	25
5.2.5	Mechanical Properties of Nanomembranes	26
5.2.6	Stability of Gold Nanoparticles	31

5.3	Applications of Gold Nanoparticles as Flexible Wearable Sensors	34
5.3.1	Chemical Sensors	35
5.3.2	Strain Sensors	36
6	Experimental Section	38
6.1	Gold Nanoparticle Synthesis	38
6.1.1	Synthesis according to Leff et al.	38
6.1.2	Synthesis according to Peng et al.	39
6.2	Fabrication of Gold Nanoparticle-Based Sensors	40
6.2.1	Fabrication of Resistive Strain Sensors	41
6.2.2	Fabrication of Chemiresistors	46
6.3	General Characterization	48
6.3.1	UV-Vis Absorbance Spectroscopy	48
6.3.2	Transmission Electron Microscopy (TEM)	49
6.3.3	Scanning Electron Microscopy (SEM)	49
6.3.4	Atomic Force Microscopy (AFM)	49
6.3.5	X-Ray Diffractometry (XRD)	49
6.3.6	Small Angle X-Ray Scattering (SAXS)	50
6.3.7	X-Ray Photoelectron Spectroscopy (XPS)	50
6.3.8	Charge Transport Measurements	50
6.4	Chemiresistor Measurements	51
6.5	Strain Measurements	52
6.6	Nanomembrane Bulging	54

6.7	Pulse Wave and Gesture Measurements	56
7	Results and Discussion	58
7.1	Strain Sensors	58
7.2	Chemiresistors	72
7.3	Mechanical Resilience	82
7.4	Durability	88
8	Bibliography	101
A	Appendix	112
A.1	Cryocell Setup	112
A.2	Four Point Flexural Bending Setup	113
A.3	Strain Measurements of Rectangular Sensors with 400 μm and 800 μm Gap	114
A.4	Comsol Strain Simulation for Shear Strain	114
A.5	Response Transients Before and After Bending Fully Printed Chemiresistors	115
A.6	Custom-Built Multiplexer Setup for Chemiresistor Readout	116
A.7	Response Isotherms and Response Transients of Fully Printed Chemiresistors	117
A.8	Stress/Strain Curves	119
A.9	Validation of Climate Chamber Parameters	120
A.10	Informed Consent Form Template for Research with Human Participants .	121
B	Safety	124
C	Danksagung	129

D Eidesstattliche Versicherung	131
---------------------------------------	------------

III List of Abbreviations

3MPA	3-mercaptopropionic acid
4DT	1,4-butanedithiol
4M1OH	4-mercapto-1-butanol
4M2P	4-methylpentan-2-one
6DT	1,6-hexanedithiol
9DT	1,9-nonanedithiol
12T	1-dodecanethiol
12A	1-dodecylamine
16DT	1,16-hexadecanedithiol
ADT	alkanedithiol
AFM	atomic force microscope
AT	alkanethiol
BDT	1,4-benzenedithiol
CIJ	continuous inkjet-printing
CTAB	cetyltrimethylammonium bromide
DoD	drop-on-demand
DRIE	deep reactive ion etching
DS	Dragon Skin 30™
DT	dithiol
DUV	deep ultraviolet
FEM	finite element modeling
GNP	gold nanoparticle
HOMO	highest occupied molecular orbital
LbL	layer-by-layer
LDA	linear discriminant analysis

III. List of Abbreviations

LUMO	lowest unoccupied molecular orbital
PCA	principle component analysis
PDMS	polydimethylsiloxane
PE	polyethylene
PET	polyethylene terephthalate
PI	polyimide
PMMA	poly(methyl methacrylate)
PSA	principal strain axis
PTFE	polytetrafluoroethylene
PVD	physical vapor deposition
rH	relative humidity
SAXS	small angle X-Ray scattering
SBH	sodium borohydride
SEM	scanning electron microscopy
SMD	surface mount device
SMU	source measurement unit
SPR	surface plasmon resonance
TBAB	tert-butylamine-borane complex
TEM	transmission electron microscopy
TG	1-thioglycerol
TOAB	tetraoctylammonium bromide
UV	ultraviolet
VOC	volatile organic compound
XPS	x-ray photoelectron spectroscopy
XRD	x-Ray diffractometry

1 Zusammenfassung

In dieser Arbeit wurden Dehnungssensoren und Chemiresistoren aus quervernetzten Goldnanopartikeln vorgestellt. Außerdem wurden kritische mechanische Parameter sowie die Langlebigkeit der Goldnanopartikelkomposite unter kontrollierten Alterungsbedingungen untersucht.

In der ersten Studie wurden flexible Dehnungssensoren, bestehend aus Nonandithiol (9DT) quervernetzten Goldnanopartikeln auf Polyimidfolie, hergestellt. Die Partikel hatten einen mittleren Durchmesser von ~ 7 nm. Die Sensoren wurden genutzt, um die Anisotropie des Dehnungsverhaltens von Metallnanopartikel basierten Sensoren zu untersuchen. Um dies zu bewerkstelligen, wurden rechteckig strukturierte Sensoren von 0 – 180° rotiert und jeweils mittels eines eigens gebauten Dehnungsmessstandes gedehnt.

Finite Elemente Analyse Simulationen wurden mit einem analytischen Modell kombiniert, welches anschließend an die Messdaten gefittet wurde. Parallele (g_{11}) und senkrechte (g_{12}) Gaugekoeffizienten, welche den piezoresistiven Anteil der Sensorantwort beschreiben, wurden ermittelt. Es wurden Werte von ~ 32 und ~ 21 für g_{11} bzw. g_{12} erhalten. Aufbauend auf diesen Erkenntnissen wurden zwei mögliche Anwendungen im Bereich der Gesundheitsüberwachung vorgestellt. Für die Durchführung dieser Messungen wurde ein Goldnanopartikel Signalgeber lithographisch strukturiert und in ein Polymer (Dragon Skin 30) eingebracht, um einen hochflexiblen Sensor zu erhalten.

Zunächst wurden Pulswellenmessungen durchgeführt, bei denen hochaufgelöste Pulswellen gemessen werden konnten. Außerdem wurden Messungen zur Bewegungserkennung durchgeführt. Hierfür wurde zunächst eine Lineare Diskriminanten Analyse (LDA) mit einem Set aus Testmessungen zu verschiedenen Gesten trainiert. Ein weiteres Set an Daten wurde dann mithilfe der LDA gefittet, wobei eine gute Unterscheidbarkeit der verschiedenen Gesten beobachtet werden konnte.

In der zweiten Studie wurden vollständig gedruckte Chemiresistoren aus Goldnanopartikeln hergestellt. Die Nanopartikel wurden mit 9DT und Mischungen aus 9DT mit diversen Monothiolen (1-Thioglycerol, 3-Mercaptopropionsäure, 4-Mercapto-1-Butanol) quervernetzt. Hierfür wurden zunächst Elektroden aus Silberpaste mittels Dispenserdrucks auf Polyimidfolie aufgetragen und im Anschluss Goldnanopartikel/Thiol Tinten mithilfe eines Inkjet Druckers aufgebracht. Chemiresistorantworten wurden mit einer Anordnung von sieben Sensoren gemessen und verschiedene Analytgase wurden genutzt.

Hierbei wurden hydrophile (Ethanol, Wasser), amphiphile (1-Butanol, 1-Propanol) und hydrophobe (n-Oktan, Toluol, 4-Methylpentan-2-on) Analyte verwendet und es wurden Analytkonzentrationen im Bereich von 100-2000 ppm eingestellt. Die Selektivität der Sensoren ließ sich hierbei durch die Monothiole einstellen, da diese mit zusätzlichen Carboxyl- und Hydroxylgruppen ausgestattet waren, welche zusätzliche Sorptionstellen für hydrophile Analytgase bereitstellten. Mithilfe dieser Sensoren konnte zwischen den einzelnen Analyten gut differenziert werden.

Hydrophobe Analyten wie z.B. Toluol wurden am besten von dem Sensor detektiert, der ausschließlich 9DT enthielt. Hydrophile Analyten wie z.B. Wasser erzeugten die stärkste Sensorantwort bei dem Sensor, der 50 % vol 1-Thioglycerol enthielt. Die Sensoren zeigten außerdem eine hohe mechanische Belastbarkeit, da diese auch nach mehrmaligem Biegen über Krümmungsradien von bis zu ~5 mm immer noch eine unveränderte Sensorantwort lieferten.

In der dritten Studie wurden dünne Filme aus Goldnanopartikeln (Durchmesser: 4 und 7 nm) hergestellt. Die Partikel wurden mit Alkandithiolen verschiedener Längen und 1,4-Benzendithiol vernetzt. Anschließend wurden die Filme auf löchrige Siliziumsubstrate übertragen, welche einen Lochdurchmesser von ~80 μm hatten, um freistehende Nanomembranen zu erhalten. Mithilfe eines hauseigenen Messaufbaus wurden die Filme bis zum Zerreißen gewölbt und aus den Messdaten kritische Spannungs- und Dehnungsparameter ermittelt. Elastizitätsmoduln von ~3–5 GPa und ~2.5–8 GPa wurden für Nanomembranen, bestehend aus Partikeln mit Durchmessern von 4 bzw. 7 nm erhalten. Die Elastizitätsmoduln konnten durch die jeweils gewählten Quervernetzer eingestellt werden. Kritische Dehnungen von ~0.3–1.5 % wurden für Nanomembranen, bestehend aus Partikeln mit einem Durchmesser von 7 nm, ermittelt. Filme aus Nanopartikeln, die mit dem aromatischen Quervernetzer hergestellt wurden, wiesen hierbei die geringsten kritischen Parameter auf, was auf die Steifigkeit des Linkers zurückzuführen ist. Die höchsten kritischen Dehnungen wurden für Nanomembranen gefunden, welche 9DT als Quervernetzer enthielten. Für die Filme aus Nanopartikeln mit einem Radius von 4 nm wurden kritische Dehnungen von ~1.2–2.5 % gefunden. Bei beiden Partikelsystemen setzte sich der Trend von abnehmenden kritischen Parametern mit abnehmender Linkerlänge durch. Auch die mit 1,4-Benzendithiol hergestellten Nanomembranen aus Partikeln mit 4 nm Durchmesser erwiesen sich als am wenigsten dehnbar im Vergleich zu den anderen Proben.

Schließlich wurden noch Alterungsmessungen durchgeführt für Partikel mit einem Durchmesser von 3–4 nm und 7 nm. Die Partikel wurden ausschließlich mit 9DT vernetzt und für jeweils 28 Tage bei 65 °C und 65 %rH bzw. 85 °C und 85 %rH in einer Klimakammer gelagert. Eine Vielzahl an elektrischen, elektromechanischen, bildgebenden und spektroskopischen Untersuchungsmethoden wurde angewandt, um den Alterungsprozess

der Partikelsysteme zu analysieren. Die Messungen zeigten, dass die Filme, welche aus kleineren Partikeln hergestellt wurden, generell eine höhere Beständigkeit unter den genannten Alterungsbedingungen aufwiesen als jene, die aus größeren Partikeln bestanden. Hierbei wurde z.B. ein geringerer Anstieg der Leitfähigkeit, als auch eine geringere Agglomeration der Partikel festgestellt. Röntgenphotoelektronenspektroskopische Messungen zeigten, dass diese Änderungen möglicherweise mit dem Verdampfen von freien Linkermolekülen aus der organischen Matrix zusammenhängen. Alle Proben beider Partikelsysteme wiesen jedoch erstaunliche Beständigkeiten auf, da sich ihre elektromechanischen Eigenschaften auch nach dem Lagern unter 85/85 Konditionen nicht dramatisch änderten. Weitere Arbeiten in diesem Bereich könnten außerdem längere Lagerungszeiträume beinhalten und die Suche nach Möglichkeiten, die Effekte, die durch die Lagerung auftraten, vollständig einzugrenzen, um die erhaltenen elektrischen und mechanischen Eigenschaften der Goldnanopartikelsensoren zu bewahren.

2 Summary

In this work, strain sensors and chemiresistors made from cross-linked gold nanoparticles (GNPs) composites were presented. Furthermore, critical mechanical parameters as well as the GNP composites' durability under defined storing conditions were analyzed. In the first project, flexible strain sensors on polyimide (PI) foil made from GNPs with a mean core diameter of ~ 7 nm cross-linked with 1,9-nonanedithiol (9DT) were fabricated. These sensors were used to characterize the anisotropic response to strain, a phenomenon observed for metal nanoparticle based sensors. To this end, rectangular shaped sensors were rotated from 0 – 180° and strained with a custom-built flexural test setup. Finite element modeling (FEM) simulations were combined with an analytic model to fit the obtained measurement data and to separate geometric and piezoresistive effects. Parallel (g_{11}) and perpendicular (g_{12}) gauge coefficients were extracted describing the composite's anisotropic piezoresistive response. Values of ~ 32 and ~ 21 were obtained, respectively, indicating that charge carriers percolate through the material taking detours through the nanoparticle network.

Based on these findings, two possible applications of such sensors were presented in the field of health care monitoring. For this purpose, a lithographically patterned GNP transducer was transferred onto and embedded in a silicon polymer (Dragon Skin 30) yielding a highly flexible triaxial sensor. First, pulse wave measurements were conducted exhibiting well resolved pulse waves. Second, gesture recognition measurements were performed. To this end, a linear discriminant analysis (LDA) was trained with a set of test data from sensors with different orientations. An additional set was recorded and fitted using the LDA which led to a good assignment of identical gestures.

In the second study, fully printed chemiresistors were fabricated using GNPs (mean diameter: ~ 7 nm) cross-linked with 9DT and mixtures of 9DT with a variety of monothiols (1-thioglycerol, 3-mercaptopropionic acid, 4-mercapto-1-butanol). The printing process comprised of two steps, first, dispenser-printing silver paste for electrode structures and second inkjet-printing GNP/thiol inks to form the transducers. Chemiresistive response measurements with a sensor array consisting of seven different sensors to a variety of hydrophilic (ethanol, water), amphiphilic (1-butanol, 1-propanol) and hydrophobic (n-octane, toluene, 4-methylpentan-2-one (4M2P)) analytes at concentrations ranging from 100 to 2000 ppm were performed. Here, the addition of monothiols with carboxyl and

hydroxyl end groups tuned the selectivity of the sensors by providing sorption sites for polar analytes. The sensor array allowed good discrimination between the different analytes. Sensors fabricated with pure 9DT showed the highest sensitivity for hydrophobic analytes such as toluene, whereas the sensor containing 50 vol% of 1-thioglycerol showed higher responses to polar analytes, e.g., water. The sensors were still functional even after bending repetitively around radii of curvature down to 5 mm.

In the third project, composite thin films made from GNPs with different core diameters (~ 4 nm and ~ 7 nm) cross-linked with alkane dithiols of different chain lengths and 1,4-benzenedithiol (BDT) were fabricated. The films were transferred onto holey silicon substrates containing a circular aperture (diameter: ~ 80 μm) to obtain freestanding nanomembranes, which were bulged until rupture using a custom built bulge setup with an atomic force microscope (AFM) detection readout. From the measurements stress/strain curves were calculated and Young's moduli of ~ 3 – 5 GPa and ~ 2.5 – 8 GPa were obtained for nanomembranes made from 4 nm and 7 nm GNPs in size, respectively, depending on the cross-linking agent. Critical strains (strain at which the membrane ruptured) of ~ 0.3 – 1.5 % were found for particles with a mean core diameter of 7 nm. Here, GNP nanomembranes fabricated with the aromatic cross-linker exhibited the lowest average values due to the rigid nature of the cross-linking molecule. The highest critical strains were observed for GNPs cross-linked with 9DT. For GNPs with a mean diameter of 4 nm critical strains of ~ 1.2 – 2.5 % were observed. For both particle systems a decrease of the critical parameters with decreasing alkane linker chain length was observed. In agreement with the results from experiments with larger GNPs, nanomembranes made from 4 nm GNPs cross-linked with BDT as well exhibited the lowest critical strain for this particle system.

Finally, durability measurements were performed for 9DT cross-linked GNPs with mean diameters of 3–4 nm and 7 nm. To this end, the samples were artificially aged for 28 days in a climate chamber at 65 %rH and 65 °C and 85 %rH and 85 °C. Here, a variety of electrical and electromechanical measurements as well as imaging and spectroscopic measurements were performed. These measurements revealed that films made from smaller particles exhibited an overall higher durability to the artificial aging conditions. This was observed in electrical measurements and microscopic images showing less increase in conductivity and less agglomeration of particles over time, respectively. X-ray photoelectron spectroscopy (XPS) measurements might indicated that the changes observed in the electrical and microscopic measurements find their origin in the evaporation of excessive cross-linker. All samples made from both particles systems remained astonishingly operative with respect to their electromechanical properties after the full aging period even under 85/85 conditions. However, future work might address appropriate sealing of the

2. Summary

GNP films with suited materials to further prevent aging effects on the GNP transducers caused by humidity and other external influences and to preserve their initial or tuned electrical and mechanical properties.

3 Introduction

Within the past century the reports on syntheses for colloidal gold nanoparticles (GNPs) emerged rapidly. Starting with an aqueous synthesis presented by Turkevich et al. in the early fifties,^[1] the variety of presented synthesis routes increased dramatically. Different approaches to tune size,^[2–4] shape^[5–7] and stabilizing ligands^[1,8–10] were presented and improved continuously. The strong interest for this type of particle system finds its origin in the unique material properties making them highly attractive in the fields of catalysis,^[11] optics,^[12] electronics,^[13] clean energy^[14] and medicine.^[15,16]

However, especially for the latter field, it is favorable to arrange GNPs in composite materials. For this purpose different approaches such as spray-coating,^[17] drop-casting^[18] or spin-coating^[19] are described in literature, yielding composites with unique tunable optical^[20–23] and electronic^[18,23–25] properties. These materials have proven themselves as highly precise resistive strain sensors^[18,26,27] and, because of their ability to sorb analyte molecules, chemiresistors.^[28,29] Due to their excellent and tunable mechanical properties^[30–33] these composites can be supported by various substrates such as glass, wafers or flexible polymers. Though the vast majority of such sensors is substrate supported, the robustness of such composites allows further the fabrication of freestanding nanomembranes to analyze mechanical properties of the as fabricated GNP composites.

Commercially available strain sensors are commonly made from metal alloy foils embedded in thin sheets of polymers and usually have sensitivities of ~ 2 .^[34] Contrary to these commercial sensors, the charge transport in sensors made from GNPs is based on tunneling of charge carriers. This phenomenon makes such sensors highly perturbation sensitive and is especially prone to the change in interparticle distance which greatly increases their sensitivities to some tens up to some hundreds.^[35,36] This renders such sensors possible to be applied in fields where faint deformations need to be detected, e.g., in health care applications. In this field of science it is also of importance to discriminate between different directions of the applied strain, as it was already shown in literature.^[37,38]

The anisotropic sensitivity to strain exhibited by GNP-based strain sensors can be exploited to detect different strain directions. It is caused by charge carriers percolating through the GNP composite by not taking the direct path between two opposing electrodes but taking detours perpendicular to the overall current direction. This behavior was well described by Jiang et al.^[39] However, since contradicting results have been presented

3. Introduction

in literature^[39,40] the first part of this work presents an in-depth study of the anisotropic strain sensitivity behavior and exploits this feature to fabricate resistive strain sensors for pulse wave monitoring and gesture detection devices. Here, the spin-coating method was used to fabricate highly homogeneous thin film composites on glass made from solutions of colloidal gold and alkanedithiols cross-linking the GNPs. To employ these composites as strain sensors, the GNP films were transferred onto flexible polymer foils using contact printing.^[41,42]

As described above, the tunability of such GNP composites has been described well in literature. However, to enable an eased and effective fabrication of low-cost sensor devices made from GNPs, new deposition and patterning methods have to be investigated. Since GNPs are commonly obtained in colloidal solutions, especially inkjet-printing proved itself as a straight-forward method for deposition and was firstly used approximately ten years ago with commonly accessible technology,^[43] to fabricate printed nanoparticle sensors.^[44-46] However, since most of the devices contain only sensor parts printed, it is of great interest to deposit all sensor components with printing techniques. This would further ease the fabrication of sensor arrays for the detection of volatile organic compounds (VOCs), so called "electronic noses". To this end GNPs are equipped with different ligands and linkers to exhibit individual sensor responses to different analytes. In the second part of this work it is intended to fully pattern and print chemiresistor devices made from chemically differently tuned GNPs on flexible substrates to build a sensor array to discriminate between various analyte molecules.

Since GNP-based sensors are investigated as wearable sensors, numerous applications demand the attachment to different parts of the human body. Depending on the application, the sensors need to endure different mechanical stresses and strains^[47,48] as well as exhibit a good durability to constantly provide the same electrical responses to similar stimuli. In industry so called "85/85 tests" are usually conducted for electronic devices, such as LCD displays, in climate chambers at 85 %rH and 85 °C for several 1000 hours to artificially age the materials and record the change of their properties testing their long-term stability. Since only few studies have been presented in the past years on the aging behavior of GNP composites only few information are present about the change of electrical and structural parameters of such material.

Hence, the third part of this work covers the investigation of critical mechanical parameters of freestanding nanomembranes made from differently sized GNPs stabilized with a variety of dithiol linkers to classify the operating range of sensors comprising cross-linked GNPs. Furthermore, the influence of artificial aging to several electrical and structural parameters of substrate supported 9DT stabilized GNP composites is discussed.

4 Objectives

Gold nanoparticle (GNP) composite materials made with organically stabilized or cross-linked nanoparticles exhibit unique features due to their electrical properties such as the highly perturbation-sensitive charge transport via tunnelling junctions and the sorption of analyte molecules into the composite's organic matrix. These features enable a variety of possible applications which have been demonstrated in manifold studies, emphasizing the great potential of thin nanoparticle films supported on flexible substrates or, even without any support, being employed as freestanding nanomembranes.

In this thesis, studies were conducted with the focus on three different subjects: deepen the analysis on strain sensitivity properties and exploit these features by designing new health care sensors, demonstrate novel fabrication methods for flexible chemiresistive devices as well as analyze critical mechanical parameters and durability properties.

1. Direction Dependent Strain Sensing

The first study of this thesis aims to thoroughly analyze the anisotropy of the strain sensitivity of GNPs cross-linked with α, ω -alkanedithiols. In these composites charge carriers do not percolate in straight lines from one electrode to another but take detours across the nanoparticle network. This behavior strongly affects the sensitivity to strain imposed to the composite in different directions. Here, the combination of simulations and experimental data should thoroughly characterize the anisotropic response to strain of such GNP-based sensors. Furthermore, this phenomenon should be exploited to fabricate highly robust and sensitive strain gauges, which can be employed for human health care measurement sensors.

2. Fully Printed Chemiresistive Devices with Tuned Selectivity

This project's objective was to fabricate fully printed chemiresistors, which can be tuned in their selectivity to preferably detect different analyte molecules. To this end, electrode structures as well as GNP transducers should be printed onto flexible polymer foils and their selectivity should be tuned by varying the composition of the organic matrix with different dithiol/monothiol blends. By arranging such sensors in an array, the overall sensor responses should lead to unique response patterns for different analytes to enable the discrimination between hydrophilic and hydrophobic molecules.

3. Critical Mechanical Parameters and Durability

The third part of the study focuses on the characterization of critical mechanical parameters for such GNP composites. Therefore, bulge experiments with freestanding nanomembranes leading to the membranes' collapse aim to yield critical stress and strain parameters, to estimate the fields of applications at which these composites can possibly be employed.

Furthermore, artificial aging under defined conditions should give insights on the long-term stability of such nanomaterials.

5 Theoretical Background

5.1 Gold Nanoparticle Synthesis

The history of gold nanoparticles (GNPs) dates back to the Roman empire, where GNPs, though unwittingly, were used to stain glasses for decorative purposes.^[49] The resulting red glasses, commonly known as ruby glass, were originally fabricated by including colloidal gold and stannic hydroxide, so called "Purple of Cassius", into molten glass.^[50] However, in modern approaches for stained glass tetrachloroauric acid is mixed to the base-glass, which is annealed at 500–700 °C.^[51] One of the most prominent examples of incorporating metal nanostructures is the Lycurgus Cup exhibited in the British Museum.^[52]

Nowadays, GNPs can be synthesized using two different approaches, namely top-down or bottom-up approaches, though bottom-up methods are far more commonly used.^[53,54] Among the most popular representatives concerning the development of GNP synthesis is Turkevich et al., who reported in 1951 the reduction of HAuCl_4 in water using citrate as both, stabilizing and reducing agent.^[1] In 1981 Schmid et al. reported on gold clusters with a very narrow size distribution by reducing gold halides with diborane.^[55] The Brust-Shiffrin method, published in 1994, had a vast impact on the scientific community, because it allowed a fast and easy two-phase synthesis of thermally stable GNPs in organic solvents.^[56] Here, the two phases consist of water and toluene and the GNP precursors were transferred to the organic phase by using tetraoctylammonium bromide (TOAB) as a phase transfer agent before the gold was reduced by sodium borohydride (SBH).

In the following, two synthesis routes are presented, which were used in this work to obtain differently sized amine-stabilized GNPs. The synthesis according to Leff et al. yields particles with a core diameter of ~4 nm and a relatively broad size distribution.^[57] This synthesis is performed in a two-phase system containing water and toluene, based on the method reported by Brust et al.^[56] After dissolving HAuCl_4 precursor in water, the $[\text{AuCl}_4]^-$ ions are transferred into the organic phase by using TOAB. Subsequently, they are reduced by SBH in the presence of 1-dodecylamine (12A) as stabilizing agent. Since amine ligands show a weaker bonding to the GNPs, further ligand exchanges with different thiols are facilitated.^[57,58] The size control of the obtained GNPs is conducted by simply altering the metal-to-surfactant ratio.

Here, higher amounts of metal lead to larger particles.^[59,60]

The synthesis according to Peng et al. yields particles with a diameter of ~2–10 nm, which is controlled by the reaction temperature.^[61] In this work, particles with a mean diameter of ~7–8 nm were synthesized to obtain particles with a diameter approximately twice as large as the smaller particles obtained from the method according to Leff et al. Contrary to the synthesis presented by Leff et al., the method by Peng et al. is performed in one (liquid) phase. Here, a solution of the gold precursor and an amine ligand is prepared in an organic solvent. Next, a reducing solution containing tert-butylamine-borane complex (TBAB) is quickly added to the precursor and nanoparticles are formed. This synthesis yields particles of a very narrow size distribution of < 10 % and their mean diameter can be adjusted by varying the reaction temperature.^[61]

5.2 Gold Nanoparticle Composite Materials

Since composites made from GNPs exhibit novel, unique properties, that can be easily adjusted, these materials are promising candidates for many possible applications.^[29,62–65] To this end, a variety of approaches was developed in the recent years.^[66,67] Depending on the specific purpose, GNPs are variously stabilized^[68,69] or cross-linked^[70,71] and different deposition methods have been developed for manifold target substrates.^[62,63,72]

5.2.1 Fabrication of GNP Films

This section gives an overview on the variety of deposition methods to obtain metal nanoparticle-based composite films. Most approaches include the modification of the size and shape of the nanoparticles as well as the composition of the embedding organic matrix to fulfill certain requirements.

Since nanoparticles are often obtained as colloidal solutions, various low-cost and straight forward deposition techniques can be applied for their deposition on different substrates. These techniques include, e.g., spray coating,^[73–75] drop-casting,^[76,77] Langmuir-Blodgett deposition,^[78] inkjet-printing,^[79–81] layer-by-layer (LbL) self assembly,^[82,83] and LbL spin-coating.^[84,85] Depending on the deposition method, size, shape, solvent, ligand shell, and concentration one can precisely tune the thickness (mono-/multilayers), crystallinity (ordered/disordered films) and spatial dimensions of such composite materials. With these methods in hand, different devices were reported in literature.

Le et al. reported on CsPbI based solar cells which were fabricated by an all-spray-coating process.^[86] Wang et al. fabricated an ZnO-based ultraviolet (UV) light photo detector via inkjet-printing.^[87] Since these technologies offer low-cost and easy deposition approaches, nanoparticle composite materials became promising candidates for flexible wearable electronics, a highly emerging field of science. Jayathilaka et al. give a comprehensive review on recent progress made on the fabrication of nanoparticle-based flexible devices.^[88]

Most fabrication methods yield composites containing GNPs stabilized by an organic matrix. By using such composites as resistive sensors, electrical current flows through the particles via tunnel junctions made of these organic molecules. Depending on the composition of the matrix it is possible to tune the properties of the sensor material. To this end, two approaches of the above mentioned techniques were used in this work, first LbL spin-coating and second inkjet-printing.

Inkjet-Printing. Especially the latter method allows the facile and alternating deposition of different solutions on a variety of substrates and the deposition of different materials such as bio-components,^[89] ceramics,^[90] metal nanoparticles,^[91] and polymers.^[43] Furthermore, digital communication with the printer enables a facile change of the geometries of the printable material reducing material usage and waste.^[92] It also allows changing the deposition parameters on the fly without fabricating new master patterns or photomasks to restructure the printed composites.

As shown in figure 5.1 there are two main operating modes for inkjet-printers, continuous inkjet-printing (CIJ) printing and drop-on-demand (DoD) inkjet-printing.^[93] While CIJ produces a continuous jet of droplets steered by an electric field, DoD printers control the droplet deposition by moving the substrate relatively to a static nozzle.^[94] Since, DoD printers are more commonly used and were also used in this work, CIJ printers will not be further discussed in this scope. As can be seen in figure 5.1 b) the droplets are formed on demand by either a thermally or piezo driven print head.

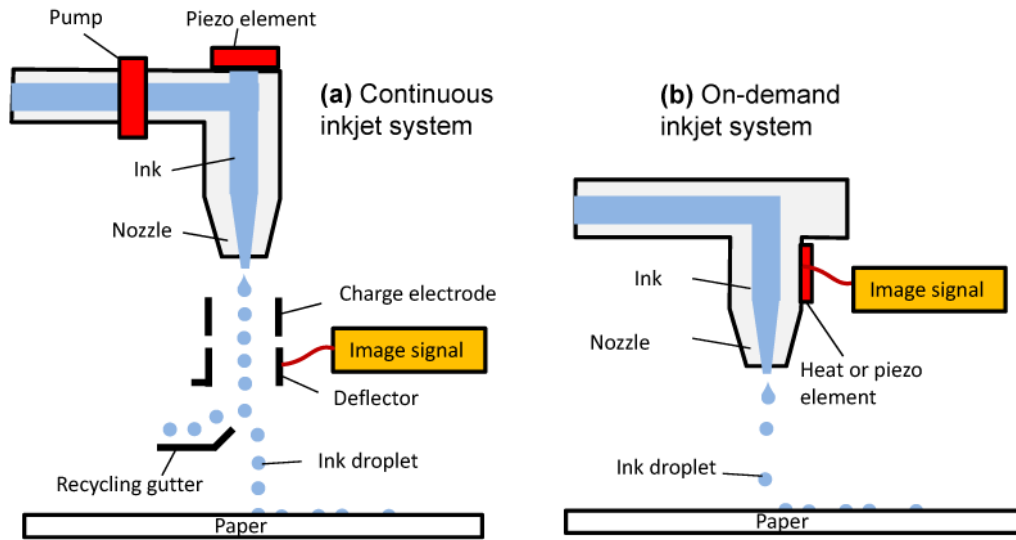


Figure 5.1: Schematics of the two different operating modes for inkjet-printers. a) CIJ printing system, which continuously ejects droplets controlled by electric fields. b) DoD printing system, ejecting droplets by piezo or thermally driven printer heads on a moving substrate. Reprinted with permission from Ref. [93]

In case of the thermally driven print head a heating element located in the print head heats the inks and causes a formation of vapor bubbles pushing the fluid through the nozzle. However, this approach is far less common as the piezo driven print head. Piezo-driven heads use a voltage-induced deformation of a piezoelectric transducer to form mechanical stress in the walls of the fluid chamber. By that, the liquid is forced in the nozzle and accelerated, leading to an ejection of the droplet.^[95]

The ejection is commonly achieved by applying a single pulse wave to the piezo-resistive print head (cf. figure 5.2 a) including a rise time t_{rise} and a fall time t_{fall} determining the periods until a target voltage is reached starting at a baseline voltage and vice versa. The dwell time t_{dwell} describes the period at which the voltage applied to the piezo element is kept constant. However, as done in this work, bipolar pulse waves (cf. figure 5.2 b) are also applied to the print head to further tune the droplet shape.^[95] Here, a positive as well as a negative voltage are applied to the print head to excite the piezo element in certain periods. The times needed to lower the voltage to a negative bias and return to the baseline voltage are called t_{fall} and $t_{\text{finalrise}}$, respectively. The period at which the negative voltage is kept constant is called t_{echo} (cf. figure 5.2 b).

Besides the forces acting during the ejection of the liquid, also its viscosity plays an important role for the printing process. It alters the diffusion and evaporation when the nanoparticle solution is deposited on the substrate and is crucial for the overall quality of the printed patterns.^[96,97] Furthermore, inkjet-printing requires accurate adjustment of

additional parameters, such as ink concentration and printing temperature.^[97] An exemplary GNP film inkjet-printed onto a glass substrate is shown in figure 5.2 c).

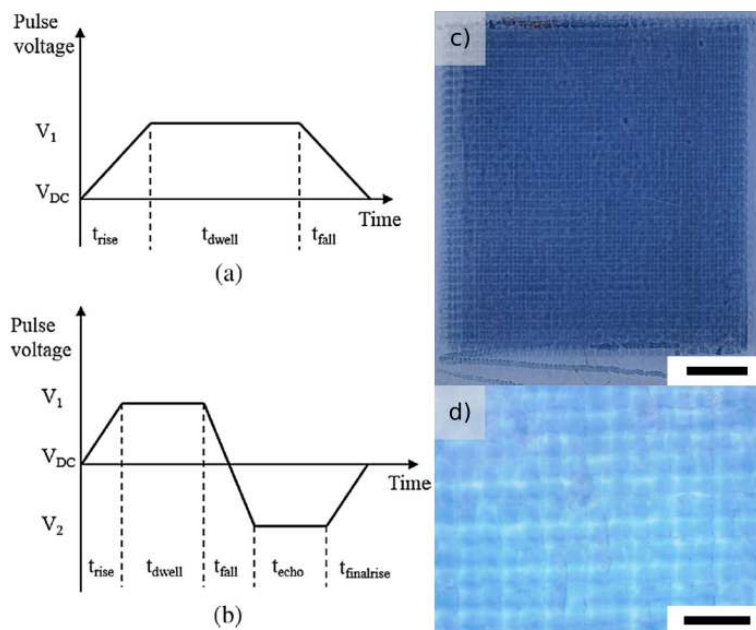


Figure 5.2: a) Depiction of a single pulse waveform. b) Depiction of a bipolar pulse waveform. c) Micrograph of an inkjet-printed GNP film cross-linked with 9DT. A consecutive zoom in to the center region of the sample is shown in d). Scale bars: c) : 1 mm, d) : 200 μm . Figure parts a) and b) were reprinted from publication Ref. [95] with permission from Elsevier (2022).

Layer-by-Layer (LbL) Self Assembly. Another deposition method to fabricate thin films of GNPs is the LbL self assembly. To this end, first, a target substrate's surface is functionalized (solution A) to offer binding sites for the first particle layer and immersed into a solution of nanoparticles (solution B) to be deposited. Second, a washing cycle is conducted, to remove unbound material and to prevent to contaminate solution A. Third, the substrate is again immersed in solution A to start a new cycle for multilayer material deposition.^[98] Though the LbL self assembly yields highly ordered nanoparticle structures,^[99] it has several drawbacks if the obtained structures need to be transferred to another substrate. Since the first particle layer is covalently bound to the surface of its original substrate, lift-off and transfer procedures are hampered.

Spin-Coating. Next to the LbL self assembly, the spin-coating is a useful technique for the fast and reproducible deposition of liquids. In 2011 a procedure to fabricate thin films made from GNPs and alkanedithiols was published by our group and is described in detail in chapter 6.2.1.^[100] Briefly, concentrated amine stabilized GNP solutions and dithiol/methanol solutions were deposited onto rotating glass substrates in an alternating

manner. The amine is thereby exchanged by the cross-linking dithiol and films of interconnected GNPs are formed on the glass substrate. After immersing the fabricated films in the respective dithiol solutions for several hours the films were rinsed in acetone and dried under nitrogen flow. The solvents of the cross-linkers and GNP stock solutions were chosen in a way, that the nanoparticles are not soluble in the solvent of the cross-linkers to prevent the GNPs from being washed away during spin-coating. By varying the number of deposition cycles, films with various thicknesses could be obtained.^[100]

This fabrication method has several advantages compared to other deposition approaches as for example the LbL self assembly. For spin-coating the functionalization of the initial substrate is not needed, which enables a facile removal of the obtained composites. Another advantage of the spin-coating is time efficient deposition of the nanomaterial, while several immersion and washing cycles need to be performed at the LbL self assembly process to obtain films with reasonable thicknesses. Finally, it is not necessary to immerse the substrate into the particle solutions. Hence, only small volumes (several μL) are needed for each deposition cycle. GNP films obtained with the spin-coating approach show a homogeneous morphology on a larger scale (figure 5.3 a). With increasing particle layers, however, they form disordered stacks (cf. figure 5.3 b), whereas the layer closest to the substrate shows highly ordered domains (cf. figure 5.3 c).

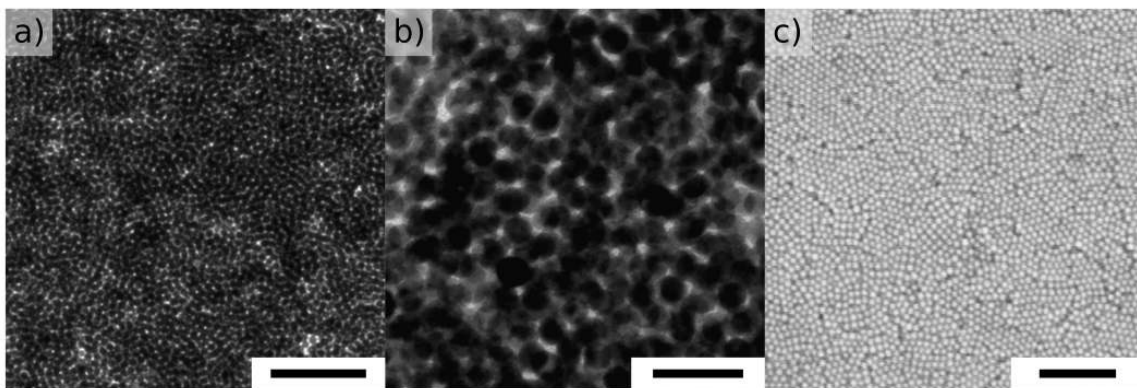


Figure 5.3: Micrographs of 9DT interconnected GNPs with an average diameter of ~ 7 nm. a) , b) Transmission electron microscopy (TEM) micrographs. c) Scanning electron microscopy (SEM) micrograph of the bottom layer of an 9DT interconnected GNP film. The sample was obtained by skimming the GNP film as described in chapter 6.6. Scale bars: a) 100 nm, b) 25 nm, c) 100 nm.

Since the GNPs are not covalently bond to the carrier substrate used for spin-coating, GNP films can be removed with a flexible polymer stamp, e.g. polydimethylsiloxane (PDMS) and transferred onto a variety of different target substrates.^[62] Methods to transfer nanoparticle patterns were reported by Li et al.^[41] and Choi et al.^[42] and their approaches were adapted in this work as explained in chapter 6.2.1. In brief, the GNP

thin film is structured and coated with a sacrificial poly(methyl methacrylate) (PMMA) layer. Next, a PDMS stamp is gently pressed on top of the coated pattern and peeled off carefully. The PDMS stamp carrying the GNP/PMMA structure is then pressed onto the (flexible) target substrate and could be removed after applying a heating/cooling procedure. Finally, the sacrificial PMMA layer was removed by dissolving the target substrate in acetone.

By this process nanoparticle films can be transferred onto different flexible polymers i.e. PI^[62] or polyethylene terephthalate (PET)^[101] with low effort. Our group could further show that nanoparticle patterns remained unchanged in geometry and morphology after transfer onto the target substrate.^[62]

5.2.2 Charge Transport

This section describes the fundamentals to understand the sensing mechanism of resistive strain sensors and chemiresistors based on GNPs. In a composite material, e.g. made of GNPs and alkane(di)thiols, GNPs act as conductive cores, whereas their surrounding organic matrix (comprising of ligands or cross-linkers) forms tunneling barriers for the charge carriers. Due to that, the electric properties of GNP composite materials are governed by tunneling of charge carriers through the organic matrix and can be described with a thermally activated tunneling process. According to this model, these materials exhibit a non-metallic behavior, i.e., increased conductivity when heated.^[102] To describe the electrical behavior different studies showed that the conductivity exponentially depends on the inverse of the temperature, showing the thermal activation of the tunneling process.^[103–106] Furthermore, the distance of the particles to each other plays a major role for the tunneling of charge carriers, hence the resistance of the composite material.^[30,100,107]

As a first approach to model the tunneling process Neugebauer and Webb developed a simple model to describe the conductivity of evaporated metal films consisting of many discrete metal island.^[108] They derived an Arrhenius-type correlation between the conductivity and the inverse temperature T^{-1} including an activation energy term E_A^* :

$$\sigma = \sigma_0^* \exp\left(-\frac{E_A^*}{k_b T}\right) \quad (5.1)$$

Here, σ_0^* is a preexponential factor, E_A^* is the activation energy and k_b, T are the Boltzmann constant and the temperature, respectively.

These findings were later adapted by Terrill et al. to develop their model as it is presented in equation 5.2. The activation energy E_A is needed, because the transfer of an electron between two neutral particles results in a charging energy. Due to the low capacitances of the nanoparticles, this amount of energy is non-negligible. In addition to the activation energy E_A they added a tunneling term to include the conductivity's dependence on the interparticle distance δ . They proposed following commonly accepted model to describe the conductivity of alkanethiol (AT) stabilized or alkanedithiol (ADT) cross-linked GNP materials:^[76]

$$\sigma(\delta, T) = \sigma_0 \exp(-\beta\delta) \exp\left(-\frac{E_A}{k_b T}\right) \quad (5.2)$$

Here, σ_0 describes a preexponential factor, β is the tunneling decay constant, E_A is the activation energy, k_b is the Boltzmann constant and T is the temperature. As one can see, equation 5.2 comprises of two exponential terms. The first term describes the tunneling of charge carriers between two particles. It has to be noted that the tunneling probability depends on the width and height of the tunneling barrier. In this model, the width of the tunneling barrier is given by the distance of the GNPs to each other and the height of the barrier is given by the chemical composition of the organic matrix surrounding the particles and affects the tunneling decay constant.^[103] According to that, the tunneling efficiency is strongly dependent on the fermi level of the metal nanoparticles and the arrangement of the highest occupied molecular orbital (HOMO) and lowest unoccupied molecular orbital (LUMO) of the organic molecules in the surrounding matrix.^[109] If the fermi level of the nanoparticles is in the gap between the HOMO and LUMO, the conductivity strongly depends on the length of matrix molecules. However, if the fermi levels of both the nanoparticles and the matrix molecules are on similar levels a weak distance dependence can be observed.^[103] It is possible to experimentally determine the tunneling decay constant according to equation 5.2 using an Arrhenius type plot ($\ln(\sigma(\delta, T))$ vs. $1/T$) and extracting the y -intercepts. These can then be plotted against the interparticle distance δ to obtain a good estimation of the tunneling decay constant.^[83,110]

For ADT cross-linked GNPs a tunneling decay constant of $\beta_N = 0.61 \pm 0.1$ was observed by Joseph et al.^[83] It has to be noted that the tunneling decay constant in that study is measured in reciprocal numbers methylene units of the ADT chains. These finding were in good agreement with a study performed by Lindsay and co-workers, finding values of 0.57 for β_N .^[111] However, higher values of 1.2 were found for β_N for particles embedded in an AT matrix.^[110]

The second term of equation 5.2 describes the above-mentioned temperature dependence and activation energy. The activation energy can be described using two different models. In a simple approach, one can consider neighboring nanoparticles as a conducting continuum separated from a central nanoparticle by an insulating shell.^[112] According to this model, the capacitance of the nanoparticle is given by:

$$C = 4\pi\epsilon_0\epsilon_r \left(\frac{1}{R} - \frac{1}{R + \delta} \right)^{-1} \quad (5.3)$$

Here, R is the particle radius, δ is the interparticle distance and ϵ_0 and ϵ_r are the permittivity of the vacuum and the relative permittivity of the organic matrix, respectively. According to fundamental electrostatics the capacitance is given by

$$C = q/U \quad (5.4)$$

Here, q and U are the charge and the applied voltage, respectively. Further, the energy saved in a capacitor is given by

$$E = \frac{1}{2}qU \quad (5.5)$$

By substituting U in equation 5.5 with an expression from equation 5.4 and considering only single electrons with a charge of e tunneling between the nanoparticle and the conducting continuum following formula is obtained:

$$E = \frac{e^2}{2C} \quad (5.6)$$

By now inserting the capacitance obtained from Abeles et al. (equation 5.3) in equation 5.6, one obtains an expression for the activation energy of granular metals given by:^[113]

$$E = \frac{e^2}{8\pi\epsilon_0\epsilon_r} \left(\frac{1}{R} - \frac{1}{R + \delta} \right) \quad (5.7)$$

According to this equation, the activation energy depends on the particle radius as well as on the permittivity of the surrounding organic matrix. Increasing the permittivity of the organic matrix results in a decreased activation energy, since charge carriers are more

stabilized. However, a reduction in particle radius results in an increase of the activation energy. Below a certain particle radius the activation energy for a charge carrier to tunnel between two particles is larger than the thermal energy defined by k_bT . Hence, charge transport is inhibited until the thermal energy is high enough to overcome this so called Coulomb blockade, resulting in non-linear current–voltage characteristics.^[114]

The second model to describe the activation energy of the tunneling process was presented by Marcus.^[115,116] According to this theory, the free energy of activation for an electron–transfer reaction ΔG_A is given by:

$$\Delta G_A = \frac{\lambda}{4} \left(1 + \frac{\Delta G^*}{\lambda} \right)^2 \quad (5.8)$$

Here, ΔG^* is the standard free energy of the reaction and λ is an "outer–sphere" reorganization energy due to the repolarization of the surrounding dielectric medium. A charge transfer between two spheres can be expressed by:

$$\Delta G_A = \frac{\lambda}{4} = \frac{e^2}{16\pi\epsilon_0} \left(\frac{1}{2R_1} + \frac{1}{2R_2} - \frac{1}{R_1 + R_2 + \delta} \right) \left(\frac{1}{\epsilon_{op}} - \frac{1}{\epsilon_s} \right) \quad (5.9)$$

Here, R_1 and R_2 are the radii of the spheres, $R_1 + R_2 + \delta$ is the center-to-center separation and ϵ_{op} and ϵ_s are the optical and static dielectric constants of the surrounding medium, respectively. Similar to the granular metal theory, this model also describes a dependency of the activation energy on the particle radius and the permittivity of the organic matrix. However, Wuelfing et al. found that, although the trends found for the activation energy can be described by equation 5.9, this model yields values much smaller than those observed.^[110,117] The activation energy can experimentally be obtained from the slope of an Arrhenius-type plot ($\ln\sigma(\delta, T)$ vs. $1/T$) using equation 5.2.^[118]

5.2.3 Resistive Strain Sensing

As discussed above, the resistance of the GNP composite materials strongly depends on the interparticle distance. This feature makes such materials highly interesting for sensing applications. To express the response of such sensor, one measures the relative change in resistance $\Delta R/R_0$, where R_0 is the baseline resistance. Assuming, that the relative

changes in resistance are equivalent to the relative changes in resistivity, equation 5.2 can be rearranged to:^[74]

$$\frac{\Delta R}{R_0} = \exp(\beta\Delta\delta) \exp\left(\frac{\Delta E_A}{k_b T}\right) - 1 \quad (5.10)$$

Microscopic Model. Wieczorek and coworkers were the first to report on the fabrication of highly sensitive GNP films using an airbrush system. The diameter of the particles used was ~ 18 nm and they were stabilized using 4-nitrothiophenol.^[119] The group stated that for nanoparticles with an average diameter of ~ 10 nm or larger and an surface-to-surface distance of ~ 1 nm the Arrhenius term of the activated tunneling becomes negligibly small compared to the tunneling term. Hence, equation 5.10 can be simplified to equation 5.11, so that the relative change in resistance solely depends on the change in interparticle distance:^[119]

$$\frac{\Delta R}{R_0} = \exp(\beta\Delta\delta) - 1 \quad (5.11)$$

The group further presents a model, to transfer the macroscopic strain ϵ applied to the material to the change in the interparticle distance $\Delta\delta$, which is described in the following. By applying mechanical stress to the material along the length L parallel to the current flow, the change in length can be expressed as ΔL . The resulting change in the length of the film corresponds to a strain of $\epsilon = \Delta L/L$. The length of the material in one direction can be expressed as $L = N(d + \delta_0)$, where N is the number of particles along a certain direction and d and δ_0 are the particles' diameter and the initial interparticle distance, respectively. The organic molecules between the nanoparticles are deformed much more easily than the nanoparticles themselves. So, the applied macroscopic strain is assumed to fully translate into the increase in interparticle distance, as it is schematically shown in figure 5.4, yielding $\Delta L = N\Delta\delta$. According to these assumptions an expression can be derived relating the interparticle distance to the macroscopic strain:^[119]

$$\Delta\delta = (d + \delta_0) \frac{\Delta L}{L} = (d + \delta_0)\epsilon \quad (5.12)$$

Therefore, equation 5.11 can be rearranged to an expression related to the strain ϵ :^[119]

$$\frac{\Delta R}{R_0} = \exp(\beta(d + \delta_0)\epsilon) - 1 \quad (5.13)$$

From this equation it can be derived, that the resistive response of GNP composite materials upon an applied strain is generally non-linear. Equation 5.13 further shows, that the resistive response can be tuned by changing the interparticle distance, as well as the size of the GNPs. However, in the limit of small strains equation 5.13 can be simplified using a Taylor approximation, yielding a linear correlation between $\Delta R/R_0$ and ϵ according to:

$$\frac{\Delta R}{R_0} = \beta(d + \delta_0)\epsilon = g\epsilon \quad (5.14)$$

Here, $g = \beta(d + \delta_0)$ and is called gauge factor, a measure for the linear sensitivity of resistive strain gauges.

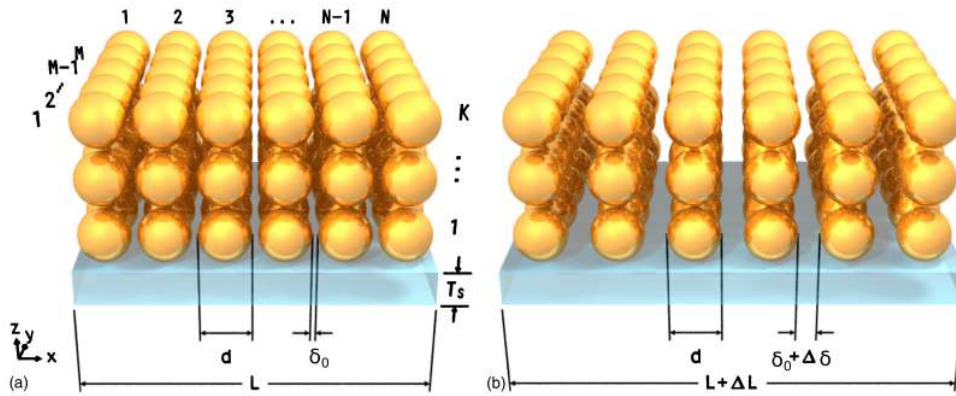


Figure 5.4: a) Schematics of GNPs in a relaxed state on a substrate with an initial interparticle distance δ_0 . b) Strained GNPs with an interparticle distance $\delta_0 + \Delta\delta$. Reprinted from Ref. [119] with the permission of AIP Publishing (2022).

For typical metal foil strain sensors gauge factors of ~ 2 are found,^[120] whereas Wieczorek and coworkers found gauge factors between 50 and 200 for their GNP systems.^[119] These findings were in good agreement with values obtained from the calculations, using a tunneling decay constant of $\beta = 10 \text{ nm}^{-1}$ and $d + \delta_0 = 10 \text{ nm}$, yielding gauge factors of ~ 100 . However, in recent studies of our group performed with GNPs cross-linked with 9DT and fabricated via LbL spin-coating gauge factors between 10 – 25 were found.^[62,63,118] The relative low sensitivities found in these studies were suggested to originate from the highly disordered GNP networks formed during spin-coating process as TEM images indicate.^[62] Farcau et al. fabricated wires of GNPs with 18 nm in diameter and widths of a few

micrometers. They could show that the sensitivity of such sensors increased when the amount of monolayers was reduced.^[121]

Furthermore, Olichwer et al. found structural changes in the film's morphology when strained, resulting in reversible crack formation during bending as well as irreversible crack formation, resulting in a permanent increase in resistance.^[63] These changes in the structure of the GNP films might also affect the overall sensitivity to strain due to strain-induced rupture of interconnects in the GNP network.

Huang et al. fabricated sensors comprising of GNPs with an average diameter of 25 nm and tetra(ethylene glycol) dithiol as cross-linking agent. The sensors were fabricated using consecutive batch deposition. To this end fresh amounts of GNP and cross-linker solution were cast multiple times onto a substrate. Gauge factors of ~ 126 were found for this type of sensor.^[122] The group attributed these high gauge factors to the highly flexible linker system as well as to the number of deposition cycles, finding similar results as observed by Farcau et al.^[121]

Anisotropy and Percolation. Though Herrmann et al. developed a commonly accepted microscopic model for GNP-based strain sensors, they did not mention the often overlooked (an)isotropic strain sensitivity observed for this type of sensors. This material behavior, however, is highly important, especially considering sensor arrays to determine strain directionalities.^[37,123] The sensor response, i.e., the relative change in resistance $\frac{\Delta R}{R_0}$, is attributed to two phenomena. They are called piezoresistive and geometric effect and are described in equation 5.15 for a sensor with an applied bias along the x direction.^[124]

$$\frac{\Delta R}{R_0} = \frac{\Delta \rho}{\rho_0} + \epsilon'_{xx} - \epsilon_{yy} - \epsilon'_{zz} \quad (5.15)$$

$$\text{with } \frac{\Delta \rho}{\rho_0} = g_{11}\epsilon'_{xx} + g_{12}\epsilon'_{yy} + g_{12}\epsilon'_{zz}$$

Here, the change of the material's resistivity upon applied strain is described by the piezoresistive effect and is expressed by the relative change of the specific resistance $\Delta \rho / \rho_0$. The relative resistance change of the material due to changes in the sensing elements geometry upon applied strain is described by the terms ϵ'_{xx} , ϵ'_{yy} , ϵ'_{zz} . These latter terms denote the applied strain in x , y and z direction, respectively.^[124] Compared to typical metal foil strain gauges, where the change in resistance is mainly related to the geometric effect, for semiconductor-based strain sensors both effects mentioned above play a major role.^[124,125]

Assuming a linear correlation between strain and relative change in resistance, equation 5.15 shows, that the piezoresistive effect can be described by a sum of products of a gauge coefficient and a strain along one dimension. The gauge coefficients g_{11} and g_{12} represent two different contributions to the relative change in resistance, depending on the orientation of the strain axis to the overall current direction (current flows across the electrode gap). In this model, g_{11} describes the piezoresistive sensitivity to strains applied in parallel to the overall current direction and g_{12} describes the piezoresistive sensitivity to strains oriented perpendicular to the overall current direction.

Another highly important aspect for the precise description of the responses to strain of GNP-based sensors is percolation. If a voltage bias is applied to a GNP film, the charge carriers follow preferred percolation pathways through the material, meaning that they do not traverse from one electrode to another in a straight line, but take detours across lower impedance junctions. Since these detours do not follow the overall current direction, they give rise to significantly influence sensitivities to strains applied perpendicular to the overall current direction. This phenomenon is described by Jiang et al. and is schematically depicted in figure 5.5.^[39]

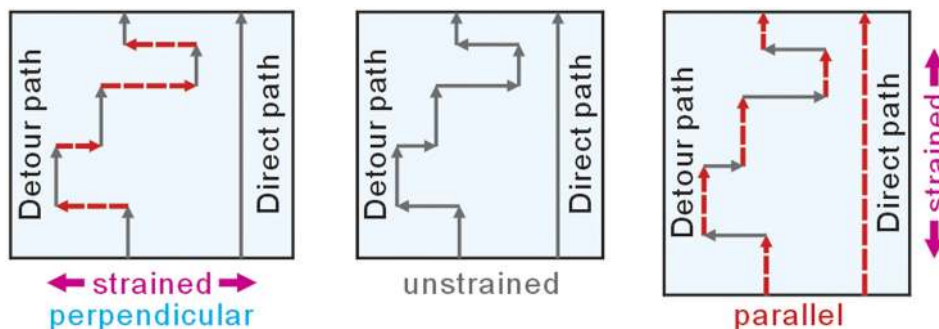


Figure 5.5: Schematic illustration of a percolation pathway through a GNP strain sensor between two electrodes with parallel and perpendicular sections. The illustration shows the effects of parallel and perpendicular strain on the percolation sections compared to a theoretical direct path. Reprinted with permission from Ref. [39].

However, in literature studies report inconsistent response characteristics of GNP-based strain sensors to strain applied in different directions. In contrast to the work presented by Jiang et al.,^[39] reporting on relatively small influences of perpendicular strains on the overall sensor response, Zhao et al. stated that GNP-based sensors exhibit highly anisotropic sensitivities.^[40] They found responses to orthogonal strains which are up to two orders of magnitude higher than such to parallel strain with respect to the overall current direction. Zhao et al. used GNPs with mean diameters of 2–5 nm, whereas Jiang et al. used GNPs with diameters of 7–12 nm. However from equation 5.14 one would

expect, that sensor made from particles with larger diameters exhibit higher sensitivities to strain, which is contradictory comparing both of the afore mentioned studies.

As GNP-based strain sensors offer high flexibility and can be fabricated using various deposition and patterning methods and due to their increased sensitivity compared to metal foil strain gauges this work further emphasizes the impact of GNP-based devices for the usage as strain sensors. They are promising candidates to be implemented in a variety of applications such as health-monitoring, human-machine interfaces, smart robots and entertainment. Zhang et al. give a state of the art overview of nanoparticles as sensor systems used in these fields.^[126] However, as shown in equation 5.10 GNP strain sensors exhibit cross sensitivities to temperature changes. These cross sensitivities can be overcome by choosing dithiocarbamates as linkers^[103] or arranging such sensors in Wheatstone bridges.

5.2.4 Resistive Chemical Sensing

Composite materials made from GNPs are also well-suited for the detection of gases, as it will be explained below. In the 1990s Wohltjen and Snow discovered, that organically stabilized GNPs exhibit a change in resistance when exposed to volatile organic compounds (VOCs).^[73] In their studies they fabricated sensors made from 2 nm sized GNP clusters stabilized by octanethiol monolayers, deposited on interdigitated microelectrodes. These chemiresistors were exposed to vapors of toluene, tetrachloroethylene, 1-propanol and water.

The resistive chemical sensing mechanism of GNP-based materials underlies two major phenomena that occur when analyte molecules interact with the matrix surrounding the GNPs. First, due to analyte sorption, the GNP films swell, which results in an increased interparticle distance. This leads, according to equation 5.10, to an increase in resistance. Second, the adsorption of analyte in the organic matrix affects its permittivity ϵ_r . In the case, that the organic matrix, surrounding and interconnecting the GNPs, consists of saturated carbon dithiols, the permittivities of most analyte vapors are higher compared to the matrix.^[127] According to the granular metal theory (equation 5.7) the activation energy decreases with increasing ϵ_r . Concluding to that, the overall conductivity increases (cf. equation 5.2) and hence this effect leads to a resistance decrease.

To investigate these two effects, Joseph et al. fabricated GNP films made with ADT cross-linkers as well as from staffene dithiols.^[128] The latter are more rigid linkers compared to ADTs, meaning the swelling of the GNP film is mostly suppressed upon analyte sorption. They showed that for staffene linkers the resistivity decreases upon analyte sorption,

presumably because the increase in permittivity becomes the dominating phenomenon, since the swelling was less pronounced. However, as can be seen from many studies, the increase in resistance due to swelling is the predominant effect, when using cross-linked GNP films as chemiresistors.^[63,128–130]

For several applications, however, the detection and recognition of VOCs is often required within mixtures of various compounds. These circumstances demand for chemiresistors which can discriminate between different analytes from mixtures, meaning they can selectively detect certain analyte molecules in such mixture. This is required, e.g. for pollutant detection,^[131] disease detection,^[132] food quality management^[133] and the detection of explosives.^[77] A common approach to detect single analytes from mixtures, is to build arrays, so called "electronic noses", made from sensors with different selectivities, which exhibit distinct response patterns upon exposure to different mixtures of analytes. As an example, Persaud and Dodd were the first to develop a sensor array to mimic the mammalian olfactory system in the 1980s.^[134] This array was made of various copper-doped tin oxide semiconductors, having distinct sensitivities to different analytes.

With ongoing technological development, the responses from the later called "electronic noses" could be interpreted very effectively using principle component analysis (PCA) and LDA.^[135] To adapt this approach in the case of sensors made from cross-linked GNPs, a crucial aspect about building a sensor array is to replace parts of the cross-linking dithiol matrix with linkers or ligands containing different functional groups, like hydroxyls, amines or carboxyls.^[81,136,137] These groups expose sorption sites for more polar analytes, while the cross-linking matrix mostly interacts with non-polar molecules. An overview of recent developments for electronic noses comprising of nanoparticle materials is given by Hu et al.^[28]

5.2.5 Mechanical Properties of Nanomembranes

In the following chapter, the term "nanomembrane" will be introduced. This term refers to freestanding layers of cross-linked GNP composite materials with thicknesses in the sub micrometer range and lateral dimensions of a few micrometers, which exhibit remarkable strength and robustness. This section gives an introduction on different fabrication methods as well as different approaches to determine the mechanical properties of such materials.

A first fabrication method is presented by Jaeger and coworkers, who developed a two-phase self assembling process. Here, GNPs stabilized with 1-dodecanethiol (12T) dissolved in toluene were spread across a water droplet, deposited on a holey substrate. After the

evaporation of the water, a freestanding monolayer of GNPs is formed over the holes.^[138] Tsukruk and coworkers used spin-assisted LbL assembly together to build up multilayer nanoparticle composite materials as it was presented in various studies.^[82,139] Together with a sacrificial layer approach reported by Mamedov et al.,^[140,141] where a cellulose acetate membrane served as supporting layer and was subsequently dissolved in acetone, they fabricated nanocomposite membranes suspended over circular microcavities with diameters of up to several hundreds of micrometers.^[142,143]

Kowalczyk et al. presented a strategy to obtain freestanding nanoparticle membranes comprising of mono- and multilayers. First, GNPs self assembled on a glass substrate (cf. figure 5.6 a),b) and were subsequently cross-linked (cf. figure 5.6 c). Next, sodium hydroxide solution was used to undercut the glass substrate and weaken the electrostatic interactions between the nanoparticles and the substrate. After floating the substrates in the NaOH solution for a few minutes, thin free floating membranes could be picked up with a PDMS stamp (cf. figure 5.6 c).^[144]

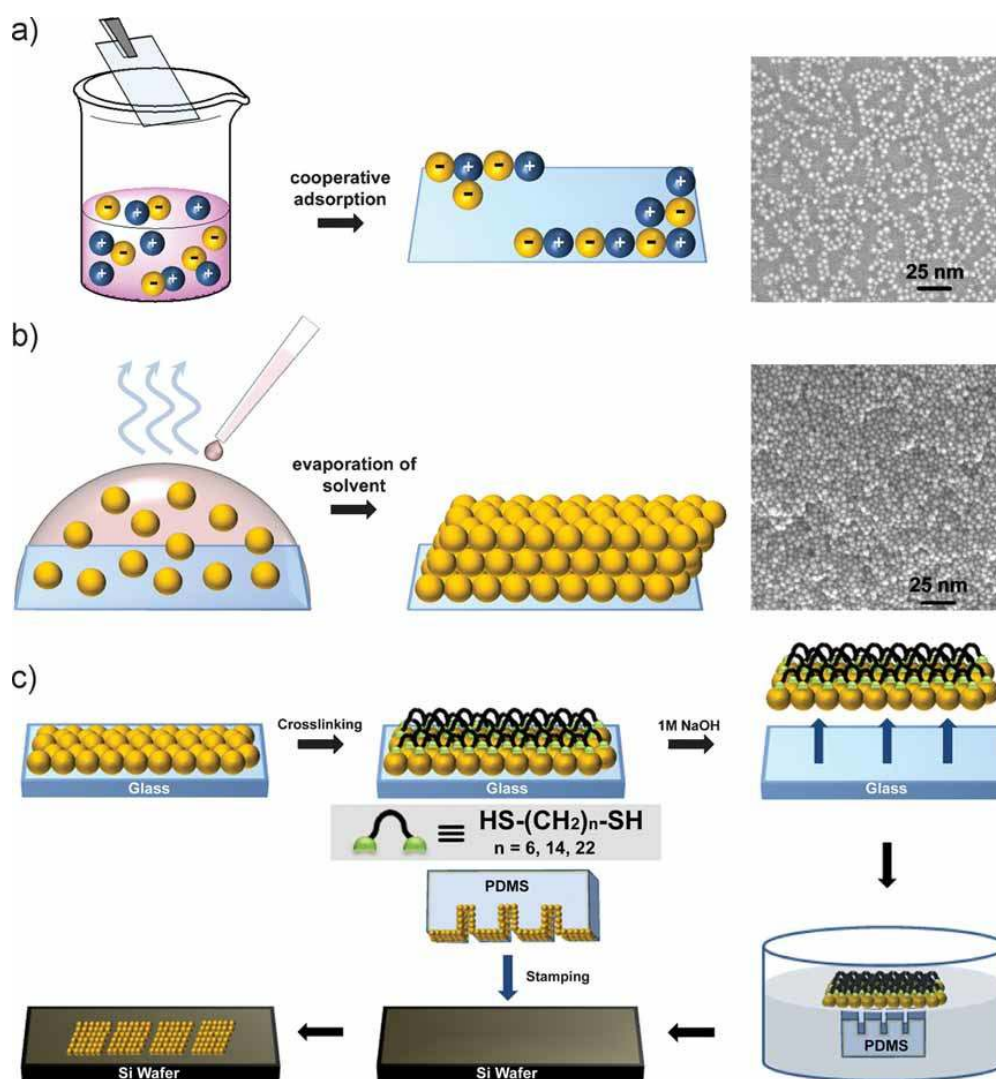


Figure 5.6: a) Fabrication of monolayers of GNPs on a plasmaoxidized glass substrate. b) Fabrication of GNP multilayers via solvent evaporation. The right columns give representative SEM images of the mono-/multilayers. c) Depiction of the cross-linking, lift-off and transfer process of GNP nanomembranes. Reprinted from Ref. [144] with permission from Wiley-VCH (2022).

This approach was also adapted and slightly modified by our group to fabricate GNP membranes as presented in different studies.^[30,31,64] Instead of PDMS stamps, 3D structured wafers were used to skim the membranes from the liquid/air interface. While the above mentioned publications presented studies based on non-crosslinked nanoparticle membranes, studies mentioned from our group reported on cross-linked multilayer GNP membranes.

Furthermore, Hartmann et al. presented a study, where they adapted a transfer mechanism for nanoparticle thin films published by Li et al.^[41] to obtain GNP nanomembranes transferred onto 3D structured silicon wafers.^[71] Briefly, small PDMS stamps were pressed

onto GNP films on glass. Next, the stamps were gently peeled off and pressed onto the structured target substrate following a heating and cooling procedure. Subsequently, the PDMS stamp was removed and freestanding nanomembranes were obtained.

Since nanoparticle composite membranes exhibit numerous new properties, there is a variety of possible applications in the fields of sensing, wearable and flexible electronics. To better estimate in which applications such GNP composites can be used, this work aims to determine critical mechanical parameters such as stresses and strains until the materials collapses.

There are different approaches for substrate-supported and freestanding composites reported in literature to probe their mechanical properties, such as nanoindentation, buckling and bulging. Even though the focus in this work laid on bulge experiments the first two approaches are briefly explained.

Nanoindentation experiments are conducted using an AFM. The AFM is not only a powerful tool for imaging, it is also capable of examining mechanical properties of nanomaterials, i.e. with indentation experiments.^[145-148] During the indentation the AFM probe is used to deflect the nanomaterial and a force-displacement curve is recorded. Later, mechanical properties can be extracted from such measurement using suitable models.^[145] Various groups studied GNP membranes via nanoindentation finding elastic moduli of several GPa.^[138,143] These findings are in good agreement with simulations.^[33,149] Furthermore Pileni and coworkers observed, that the elastic modulus decreases with increasing particle size as well as with increasing ligand length.^[150] This unintuitive behavior is explained by the increase in curvature for smaller particles compared to larger ones. Here, the arrangement of the ligand molecules is affected, causing different ligand-ligand interactions, resulting in different elastic moduli.^[150,151]

Another approach to investigate the mechanical properties of nanoparticle composite materials is the buckling method. A typical measurement includes a soft polymer like PDMS with a known elastic modulus and Poisson ratio.^[152] After transferring the nanomaterial onto the polymer substrate a compressive force is applied to it. This compression leads to a microbuckled pattern. The buckling wavelength λ can be obtained from either optical microscopy or AFM measurements. According to equation 5.16 one can calculate the elastic modulus of the nanomaterial.^[152]

$$\lambda = 2\pi d \left(\frac{\bar{E}_f}{3\bar{E}_s} \right)^{1/3} \quad (5.16)$$

5. Theoretical Background

Here, d is the thickness of the nanomaterial, $\bar{E} = E/(1 - \nu^2)$ is the plain-strain modulus and E and ν are the elastic modulus and the Poisson ratio, respectively. The subscripts f and s refer to the nanomaterial and the substrate, respectively.

The bulging approach employed in this work aimed to determine the elastic moduli, critical strains and critical stresses of GNP nanomembranes interconnected with different dithiol linkers and is schematically shown in figure 5.7.

To perform bulging experiments, a nanomembrane is transferred onto a wafer substrate containing an aperture. These apertures are typically circular shaped and in the micrometer range. Next, pressure differences of up to several kPa are applied and can even cause the nanomembranes to collapse. The resulting deflection of the nanomembranes can be measured via interferometry^[142,143,153] or via AFM,^[30,154,155] as it was done in this work. In a simple bulging approach, a nanomaterial with a pre-stress σ_0 is placed onto such afore mentioned substrate with a circular aperture having the radius a . The material is then bulged by applying different overpressures P . The shape of the bulge can then be calculated by applying a spherical cap model with a radius of curvature R_c .^[156] Because the thickness t of the material is much lower than its lateral extent, the bending stiffness of the material can be neglected by only considering the in-plane stress. Hence, the nanomembrane can be considered as a thin-walled pressure vessel and its biaxial stress σ can be calculated according to equation 5.17.^[31,156]

$$\sigma = \frac{PR_c}{2t}. \quad (5.17)$$

The biaxial stress is directly related to the biaxial strain ϵ in the linear regime with the biaxial modulus Y and the Poisson ratio ν according to equation:^[31]

$$\sigma = Y\epsilon = \frac{E}{1 - \nu}\epsilon \quad (5.18)$$

The biaxial strain ϵ of the nanomaterial can be obtained from equation 5.19:^[31]

$$\epsilon = \frac{s - s_0}{s_0} \quad (5.19)$$

Here, s is the bulge's arc length measured upon application of an overpressure and s_0 is the bulge's arc length at infinitesimal applied stress. The arc length s can be calculated according to:

$$s = 2R_c \arcsin \frac{a}{R_c} \quad (5.20)$$

The radius of curvature R_c is extracted using the circular-fit method. To this end, circles were fitted to the dome section of the line profiles of the nanomembrane's bulge taken with the AFM under varying pressure.^[31]

In this work, the nanomembranes' critical stress and strain parameters were recorded. For that purpose, the nanomembranes were bulged until they ruptured and from the last obtained set of measurement points for an intact nanomembrane, critical stress and strain values were calculated. In order to protect the AFM's cantilever from being damaged by rupturing nanomembranes, underpressures were applied to the back side of the nanomembranes by using a vacuum pump. However, it should be noted, that all calculations shown above can be conducted for either positive or negative pressure differences.

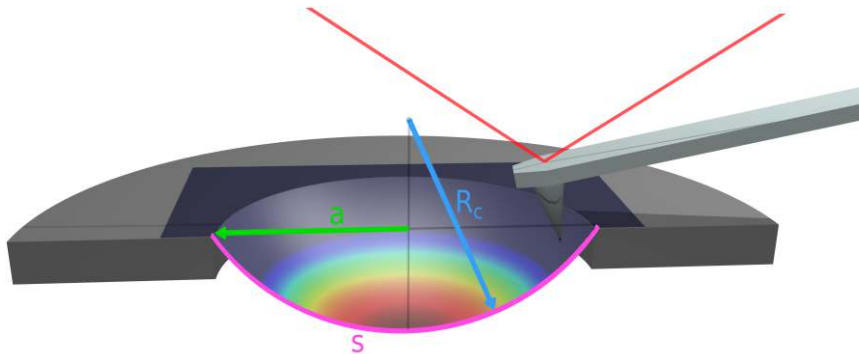


Figure 5.7: Schematic illustration of a bulge measurement as it was conducted in this work. An underpressure was applied to the nanomembrane. The blue and green arrows indicate the radius of curvature R_c and the aperture radius a , respectively. The purple outline marks the bulge's arc length s . Line profiles of the nanomembrane's topography were obtained via AFM measurements. Adapted from Schlicke.^[157]

5.2.6 Stability of Gold Nanoparticles

Despite the progress in understanding the manifold possible applications of GNP composite materials, another crucial aspect regarding their implementation in commercial devices is the evaluation of their aging behavior. Here, it is of high importance to understand under which conditions and time scales GNP composites are stable in a way that crucial

properties such as the perturbation sensitive charge transport remain unchanged. Otherwise sensor responses would change and hence false interpretations might be the cause. Dasog et al. presented a study in 2007, showing that halide ions play a crucial role in oxidizing GNPs in solution when exposed to air.^[158] They found that Ostwald ripening mechanisms lead to an increased particle size and that thiol oxidation decreased with increasing particle size. Hou et al. investigated the oxidation of monothiolate and dithiolate capped GNPs with a diameter of ~ 2 nm. They surprisingly found that dithiolate-capped GNPs have a higher oxidation rate than monothiolate-capped GNPs. They attribute these findings to the higher accessibility for oxygen ions to reach the metal core in a disordered dithiolate matrix, whereas monothiolates form highly ordered monolayers on the particles' surface.^[159]

In a recent work, Kraus and coworkers found that the storage of 12T stabilized GNPs under different ambient and inert conditions alters the particles' colloidal stability and optical properties. They state that only particles stored under argon gas are mostly protected from aging effects and quantified their results with dynamic light scattering (DLS) and UV/vis absorption spectroscopy measurements.^[160]

However, most of the above presented studies investigated particles in solution. Since the sensor applications of GNPs relevant in this work are based on substrate-supported composite materials, aging experiments performed with cross-linked GNP films would be more meaningful. Here, Joseph et al. presented a first study about the long-term stability of 9DT and 1,16-hexadecanedithiol (16DT) cross-linked GNPs aged for 44 months.^[161] They compared the gas sensing properties towards a variety of analytes before and after the storage under different conditions (ambient and inert). Their findings were supported by XPS and resistance measurements. The group showed, that composites stored under ambient conditions mainly change their sensing properties due to oxidation of the gold-bound sulfur, resulting in lower responses to hydrophobic and higher responses to hydrophilic gas analytes after 44 months. Furthermore they found decreased baseline resistances after storing, as well as coalescent particles. This is in agreement with a study mentioned above.^[158] However, contradictory results were found in studies by Hou et al. and Lacava et al., because no particle agglomeration was observed after aging.^[159,160] Even considering its importance, only little on GNP aging was found literature. Hence, aging experiments were conducted in the scope of this work, focusing on artificial aging, as commonly employed in industry.^[162] Here, 9DT cross-linked GNPs of different sizes were aged at high temperature and high humidity for four weeks in a climate chamber to promote higher reaction speeds. As an approximation the Q_{10} rule, which is commonly used for enzyme reactions, is applied to estimate a virtual aging time for the samples if aged under ambient conditions.^[163] Several experiments such as charge transport, mechanical,

x-Ray diffractometry (XRD), XPS, UV/vis spectroscopy and optical measurements were performed to monitor the aging of such composite nanomaterials.

5.3 Applications of Gold Nanoparticles as Flexible Wearable Sensors

In the past years, significant research efforts have been devoted to investigate GNP composites as wearable strain and chemical sensors. The possible applications are widely spread across a variety of topics, such as body motion monitoring,^[164] human-machine interfacing,^[165] breath and sweat analysis.^[166,167] GNPs are also commonly employed as colorimetric sensors, due to their strong plasmonic coupling. However, this aspect is not further discussed in the scope of this work.

Figure 5.8 schematically summarizes the different fields of applications for wearable GNP chemical and strain sensors. A huge benefit among other (metal) nanomaterials is the high biocompatibility of GNPs,^[168] a crucial aspect, since most devices are in direct contact with the human skin. In the following a state of the art overview is given for the categories chemical and strain sensing, in which GNPs find various applications.

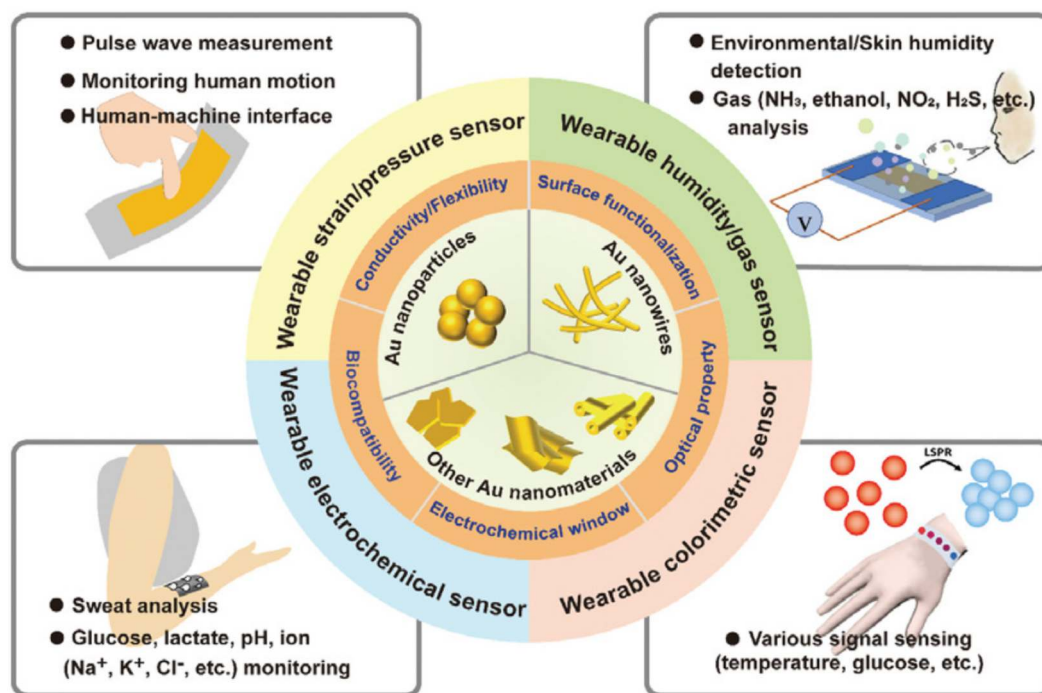


Figure 5.8: Schematics of the employment of GNP-based sensors for various applications. Reprinted from Ref. [67] with permission from Wiley-VCH (2022).

5.3.1 Chemical Sensors

Wearable chemical sensors capable of monitoring humidity from human skin in real time can provide information on the individual health status.^[169] In a recent work, Su et al. presented a highly sensitive humidity sensor based on GNPs/graphene oxide/3-mercaptopropyltrimethoxysilane. The sensor was fabricated via a sol-gel process and self assembly. The sensor showed high flexibility, low hysteresis and relative humidity (rH) detection from 20 %–90 %.^[170] Liao and coworkers also presented a highly responsive humidity sensor with a detection range of ~2 %–95 % rH and fast recovery times of 1–3 s.^[45] To fabricate highly homogeneous humidity sensors, Zhang et al. adapted inkjet-printing technology to fabricate flexible humidity sensors made of GNPs/reduced graphene oxide composites on PET substrates. The sensor exhibited high optical transparency and a wide detection range from 11 %–98 %rH.^[171] Samori and coworkers reported on a sensor based on GNPs interconnected with oligoethylene glycol dithiols showing high response times (~26 ms) and short recovery times (~250 ms) without hysteresis or fatigue effects.^[172]

Despite the exhaled water, the human being transpires a myriad of biomarkers and VOCs while sweating or breathing. Hence, the development of chemical sensors to detect and discriminate such biomarkers is of high interest for disease diagnosis to improve health care monitoring applications.^[173] As for example NH_3 is a biomarker for kidney and stomach diseases, Li et al. developed a sensor comprised of gold/polypyrrole electrospun nanofibrous films. Here, NH_3 can easily penetrate into the porous structure. The GNPs play a crucial role in promoting the reactions between the polypyrrole and the NH_3 leading to high sensitivity, fast response and recovery behavior at room temperature.^[174] GNPs can further help to reduce the operating temperature of state-of-the-art semiconductor metal-oxide based gas sensors. Ma et al. fabricated $\text{SiO}_2\text{-WO}_3$ composites decorated with GNPs (diameter: 5 nm) capable of sensing ethanol gas with high sensitivity at an operating temperature of 150 °C.^[166]

Glucose sensing also plays a major role in the field of chemical sensing, since diabetes is a chronic illness that has high impact on human health and can lead to a variety of complications in many organs.^[175] To ease diabetes monitoring, electrochemical glucose sensors can overcome these challenges. Park and coworkers presented a graphene oxide/PtGNP alloy sensor having great potential to detect glucose in the human sweat. The alloy was electrochemically deposited onto the graphene oxide to increase the electroactive area. Here, the oxidation of glucose to gluconolactone and H_2O_2 was catalyzed and the glucose concentration was determined by the redox potential of the H_2O_2 .^[176] To improve the wearing comfort, Kim et al. developed a noninvasive wireless patch type glucose sen-

sor based on hyaluronate/GNP/graphene oxide.^[167] The complex provided high surface area, good stability, long-term sweat retention and enhanced enzyme reaction. The group showed, that the sensor exhibited fast response times (~ 5 s) and a low detection limit (0.5 mg dL^{-1}). By comparing this sensor to a commercially available blood glucometer, a good correlation was found.

5.3.2 Strain Sensors

Among many nanomaterials such as graphene, carbon nanotubes and carbon black, metal nanoparticles have proven to be effective for building high-performance wearable strain sensors. In this scope GNPs are excellent candidates to develop such sensors, as it will be discussed in the following.

As can be seen from chapter 5.2.2 GNP based sensors show an unwanted cross sensitivity towards changes in temperature. Here, Yi et al. developed a strain sensor fabricated on PET substrates in two thermal evaporation steps.^[104] The sensor showed high sensitivity with a detection limit for mechanical strain of 8.3×10^{-6} and temperature coefficients of almost zero. This suggests, that distortions of the sensor signal by changes in temperature are eliminated. The group presented a proof of concept application to use this sensor for pulse wave measurements, since the shape of the pulse wave patterns give insight to many diseases such as arterial stiffness and high blood pressure.^[177]

Another method to monitor pulse-related data to prevent cardiovascular diseases, is to record a cardiogram. You et al. reported on a flexible PDMS supported sensor, where GNPs were rubbed over the elastomer's surface.^[178] Liquid PDMS was subsequently poured onto the GNP pattern to form the final sensor. This sensor could be employed to measure real-time mechanocardiogram and hemodynamics of the heart.

Next to the above mentioned physiological parameters, it is also of high interest to monitor human motions with lightweight and high comfort sensors. Gong et al. developed flexible strain sensors on different substrates (PET, PDMS, Eco-flex, nitrile, latex) made from gold nanowires.^[179] The sensors exhibited high stretchability of $>305\%$, a wide strain range ($0.01\% - 200\%$), fast response times (<22 ms) and high robustness of over 5000 loading-unloading cycles. These sensor properties allowed for the movement detection of different muscle regions such as cheek motions and finger flexion at a moderate gauge factor of ~ 10 . Such nanowire-based sensors can also be employed as human-machine interfaces as presented by another of that group's studies.^[180] Here, gold nanowires were doped with polyaniline microparticles and drop-casted onto a latex rubber increasing the conductivity by a factor of 10 and improving the sensitivity by a factor of ~ 8 . The as

fabricated sensors were fixated onto a glove to allow the remote control of an robotic arm. Duan et al. presented another approach by forming a hybrid material of silver nanowires and gold nanowires. This composite material exhibited gauge factor values from 12 at 5 % strain to 2370 at 70 % strain and allowed for the detection of moving body parts, such as facial movements, drinking and saliva swallowing.^[181] Furthermore, An et al. presented a sensor made of gold nanowires partially embedded in PDMS, which were subsequently transferred onto polyvinyl alcohol paper and used as a human-machine interface.^[182] Among spherical nanoparticles and nanowires a third type of nanoparticle shapes, gold nanosheets, were employed as wearable strain sensors. Here, Lim et al. presented a sensor made from multilayers of nanosheets (thickness: 20 nm) stacked on an elastomeric substrate yielding a highly stretchable thin film.^[183] Gauge factors of up to 70 were measured and the sensor was capable of enduring strains of up to 70 %. The sensor response further remained reliable even after 10.000 stretching cycles and could be used for body motion detection such as walking, swallowing and breathing.

6 Experimental Section

6.1 Gold Nanoparticle Synthesis

In the following, two syntheses methods for the preparation of amine-stabilized GNPs with different particle diameters are described. Particles synthesized according to a method described by Leff et al.^[59] have a diameter of ~ 4 nm, whereas particles synthesized according to a method presented by Peng et al.^[61] have a diameter of ~ 8 nm. It has to be noted, that the synthesis according to Peng et al. was slightly modified by using n-hexane and 1-dodecylamine (12A) instead of tetralin and oleylamine, respectively.

6.1.1 Synthesis according to Leff et al.

Materials and Apparatus. *Materials:* Gold(III)chloride trihydrate (Alfa Aesar, 99.99 %), tetraoctylammonium bromide (TOAB), 12A (both Sigma Aldrich, 98 %), sodium borohydride (SBH) (Fluka, ≥ 99 %), toluene (VWR, 99.5 %), ethanol (VWR, 100 %), n-heptane (Honeywell, ≥ 99 %), 0.2 μm polytetrafluoroethylene (PTFE) syringe filters (Micropur), 12T (Sigma Aldrich, ≥ 98 %), demineralized water (18.2 M Ω cm, ELGA LabWater, PURELAB flex System).

Apparatus: Centrifuge (Sigma, 3-18K).

Synthesis. The reaction was conducted in 500 mL Schott flasks. All agents as well as their molar amounts and solvents used for the synthesis are listed in table 6.1. First, gold(III)chloride trihydrate was dissolved in demineralized water and added to the Schott-flask. Then, TOAB and 12A were separately dissolved in toluene and SBH was dissolved in demineralized water. All agents were heated to 30 °C in a water bath before usage. Due to the short half-life period of SBH it was dissolved just before adding it to the reacting solution. Under vigorous stirring TOAB, 12A and SBH were added to the reacting solution in this order. Here, the TOAB acts as a phase transfer agent to transfer the gold precursor to the organic toluene phase. After the phase transfer was completed, the 12A was added to stabilize the nanoparticles and the solutions changed its color to a turbid orange. After adding the SBH, which acts as a reducing agent, the reaction solution instantly turned

into a dark red indicating the formation of GNPs. The reaction was left under stirring for 16 h. Afterwards, the aqueous phase was discarded and 80 mL of ethanol were added to the organic phase to precipitate the GNPs. Subsequently, the solution was stored for at least 15 h at $-8\text{ }^{\circ}\text{C}$. After discarding most of the clear supernatant the remaining solution was centrifuged for 10 minutes at 4400 g and $0\text{ }^{\circ}\text{C}$. After subsequent drying the GNPs in a stream of nitrogen, the GNPs were redispersed in 4 mL of n-heptane and filtered using $0.2\text{ }\mu\text{m}$ PTFE syringe filters.

Table 6.1: Molar amounts of chemicals for Leff synthesis.

chemical	amount of substance [mmol]	solvent / volume [mL]
gold(III)chloride trihydrate	0.5	demin. water / 20
TOAB	1.2	toluene / 20
12A	6.4	toluene / 30
SBH	6.04	demin. water / 20

Ligand Exchange for TEM Analysis. GNPs stabilized with 12A tend to accumulate during exposure to high energy electron beams. To increase the stability of such GNPs during TEM analysis, a ligand exchange from 12A to 12T was conducted.^[100] Therefore, 500 μL of n-heptane were firstly mixed with 25 μL of 12T and 25 μL of the GNP stock solution were added. After agitating the mixture for 30 min, 1 mL of ethanol was added. The resulting suspension was centrifuged at room temperature (2000 g, 5 min) and the supernatant was discarded. The particles were subsequently dried in a stream of nitrogen and finally redispersed in toluene.

6.1.2 Synthesis according to Peng et al.

Materials and Apparatus. *Materials:* 12A (Sigma Aldrich, 98 %), n-hexane (Honeywell, $\geq 99\%$), gold(III)chloride trihydrate (Alfa Aesar, 99.99 %), TBAB (Sigma Aldrich, 97 %), n-heptane (Honeywell, $\geq 99\%$), 2-propanol (VWR, 97.8 %), ethanol (VWR, 100 %), oleylamine (Sigma Aldrich, 70 %, technical grade), $0.2\text{ }\mu\text{m}$ PTFE syringe filters (Micropur).

Apparatus: Centrifuge (Sigma, 3-18K).

Synthesis. Table 6.2 lists the required amounts of all agents needed for the synthesis. A typical synthesis was performed in a 50 mL three-neck flask by dissolving 12A in 10 mL of n-hexane and heating the solution to $30\text{ }^{\circ}\text{C}$. After the amine, used to stabilize the forming nanoparticles, fully dissolved, 1 mL was withdrawn and gold(III)chloride trihydrate was

added to the remaining solution in the three-neck flask under vigorous stirring. In a next step TBAB, acting as a reducing agent, was added to the separated 1 mL of 12A/n-hexane mixture. After dissolving the TBAB completely, the TBAB/12A/n-hexane mixture was rapidly added to the three-neck flask. The solution was kept under mild stirring for one hour. Subsequently the synthesis was stopped and 50 mL of ethanol were added to the solution and it was stored over night at 4 °C. Afterwards, the solution was centrifuged (20000 g, 10 min, 0 °C) and the precipitant was dried in a stream of nitrogen. The GNPs were redispersed in 4 mL of n-heptane. To remove excess ligands from the GNPs, 12 mL 2-propanol were added. The solution was centrifuged again according to the parameters mentioned above. The washing step cycle was carried out twice. Finally, the GNPs were redispersed in 4 mL n-heptane and filtered using 0.2 µm PTFE syringe filters.

Table 6.2: Molar amounts of chemicals for Peng synthesis.

chemical	amount of substance [mmol]
gold(III)chloride trihydrate	0.25
TBAB	0.5
12A	30

Ligand Exchange for TEM Analysis. To prevent agglomeration of such GNPs a ligand exchange from 12A to oleylamine was conducted. Therefore, 500 µL of n-heptane were mixed with 25 µL of oleylamine and 25 µL of GNP stock solution. After agitating the mixture for one hour, 1 mL of ethanol was added. The resulting suspension was centrifuged at room temperature (2000 g, 5 min) and the supernatant was discarded. The particles were subsequently dried in a stream of nitrogen and finally redispersed in toluene.

6.2 Fabrication of Gold Nanoparticle-Based Sensors

In this work, GNP strain and gas sensitive sensors comprised of differently sized GNPs cross-linked with 9DT were fabricated. For the chemiresistors, various monothiols were added to tune the sensors' selectivity. GNP thin films were fabricated and structured using different methods. Strain sensors were solely fabricated using a spin-assisted LbL deposition technique (cf. figure 6.1) as described in our groups earlier work.^[100] Chemiresistors were fabricated using ink-jet printing (cf. figure 6.5). For all applications, the sensors were transferred onto flexible supporting substrates.

6.2.1 Fabrication of Resistive Strain Sensors

Materials and Apparatus. *Materials:* Glass cover slips (Carl Roth, LH24.1, borosilicate, 22×22 mm², thickness 0.17 ± 0.005 mm), acetone (VWR, 100 %), methanol (VWR, 100 %), 2-propanol (VWR, ≥ 99.5 %), chlorobenzene (Honeywell, ≥ 99 %), PMMA (Sigma Aldrich, average molecular weight: 996 kDa), 4M2P (Sigma Aldrich, ≥ 98.5 %), 9DT (Alfa Aesar, 97 %), demineralized water (purified using a Purelab flex system, 18.2 M Ω cm), PDMS (Sigma Aldrich, Sylgard 184, ratio 10:1, w:w, base:curing agent), PI foil (DuPont, 200QR1), Dragon Skin 30TM (DS) polymer (KauPo), conductive silver paste (PE873).

Apparatus: Plasmasystem (Harrick Plasma, Plasma Cleaner PDC-32G), ultrasonic bath (PTIC-3-ES, Palsson), spin-coater (Süss MicroTec, LabSpin 6), hot plate (Harry Gestigkeit GmbH, PZ 28-2 SR), vacuum deposition system (Oerlikon Leybold Vacuum, UNIVEX 350G).

Substrate Preparation for Spin-Coating. Glass cover slips for GNP film preparation were first immersed into an acetone bath and sonicated for 15 min. Afterwards the glass substrates were washed with demineralized water and dried in a stream of nitrogen. Finally they were treated in air plasma for two minutes to remove residual organic components.

Fabrication of GNP Films. For a typical GNP film fabrication, GNPs were deposited onto the pre-treated glass cover slips using spin-coating LbL deposition rotating the cover slips at 3000 rpm. In a first step, 100 μ L of the 9DT/methanol cross-linker solution (7.4 mM) were deposited twice within a time interval of 30 s. Next, 10 μ L of the GNP stock solution were applied, followed by two deposition steps of the 9DT/methanol cross-linker solution. Between each deposition step an intermission of 30 s was adhered to. In this context one GNP stock solution and two cross-linker solution steps represent one layer of the GNP film. This sequence may be repeated for several times to vary the film's thickness. In this work, GNP films comprising of three or five layers were fabricated.

Subsequently, the cover slips were immersed in ~ 5 mL of the cross-linker solution for ~ 16 h. Next, the films were thoroughly rinsed with acetone and dried under nitrogen flow. Figure 6.1 depicts a schematic of the spin-coating process.

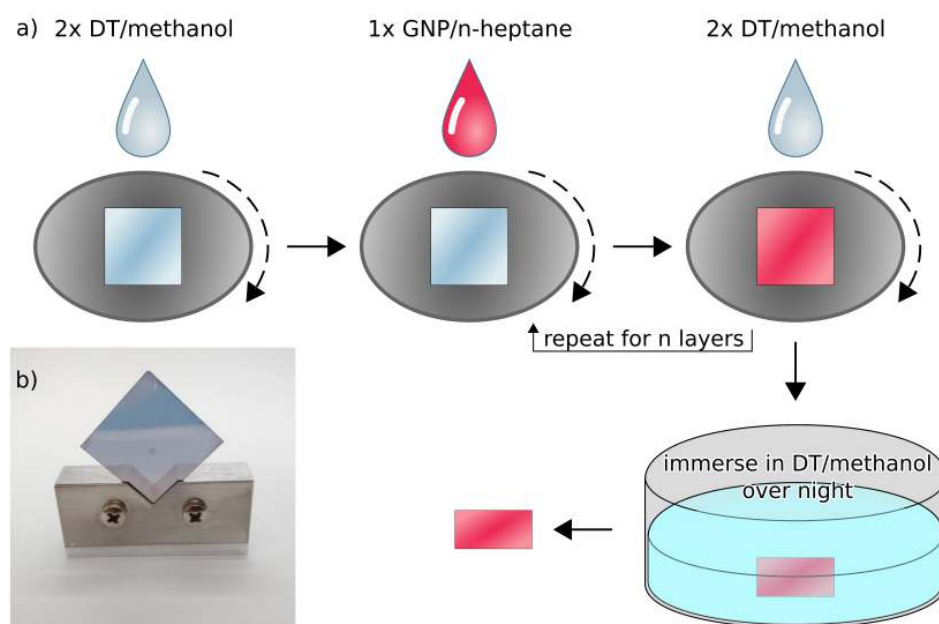


Figure 6.1: a) Schematic depiction of the spin-coating process.^[100] First, a dithiol (DT)/methanol solution was spin-coated twice onto the substrate. Next, the GNP solution was deposited followed by the cross-linking solution. The obtained GNP films were immersed in the respective DT/methanol solution for ~16 h. b) An exemplary GNP film deposited on glass is shown.

Fabrication of Lithographically Patterned GNP Films. To fabricate GNP films with elaborate geometries, they were patterned via deep ultraviolet (DUV) lithography in a lift-off method according to a procedure by Schlicke et al.^[84] First, the glass cover slip was plasma treated as described above. Next, the substrate was coated with PMMA dissolved in chlorobenzene (33 mg/mL) via spin-coating (4000 rpm, 60 s) and baked for 10 min at 60 °C (cf. figure 6.2 a) step i). Next, the PMMA-coated substrate was exposed to a custom-built DUV radiation source (λ 254 nm, dosis: 34,4 mW/cm²) through a custom-designed quartz photomask for 130 min (cf. figure 6.2 a) step ii). After irradiation, the PMMA was developed using a mixture of 2-propanol and 4M2P (ratio 3:1, v:v) for 70 s and rinsed with 2-propanol (cf. figure 6.2 a) step iii). After additional plasma cleaning the glass substrates for 2 min, GNPs were deposited via spin-coating as described above (cf. figure 6.1). The fabrication of the photomask is described below. The GNP films spin-coated onto PMMA-patterned substrates were immersed in 9DT/methanol solution for two hours. In a final step, a lift-off was performed by immersing the cover-slips into acetone to remove residual PMMA yielding a patterned GNP film (cf. figure 6.2 a) step iv). A representative image of a lithographically patterned GNP transducer on glass is shown in figure 6.2 b).

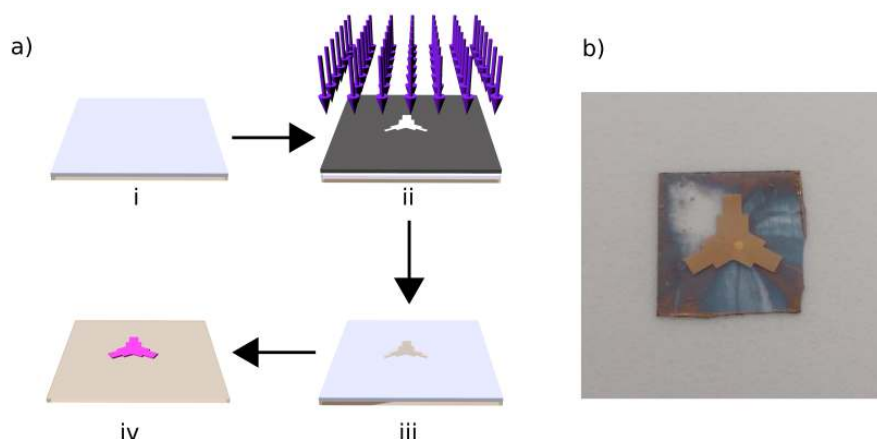


Figure 6.2: a) Schematics of the fabrication of lithographically patterned GNP films. Part i shows PMMA-coated glass substrates. Part ii depicts the DUV irradiation of the glass substrate through a photomask. Part iii-iv show the developed PMMA on the glass substrate and the GNP thin film after the lift-off, respectively. b) Image of a GNP film after the PMMA layer and excess GNPs were removed from the top side via lift-off. Residual GNP film still remains on the backside of the glass substrate.

Transfer onto Flexible Polyimide (PI) Substrates. Before transferring the as-prepared glass-supported GNP films onto a flexible polymer substrate, the films were mechanically structured using a scalpel. The GNP films were removed in such a way, that there was 1 mm space to the edges of the glass substrate and 2.5 mm x 4 mm rectangles were obtained (figure 6.3 a)). It has to be noted, that no further mechanical structuring for the GNP films fabricated using the lithography step was necessary. The mechanically structured rectangular films were cleaned under nitrogen flow and a sacrificial PMMA layer (100 μ L, 5 wt% in toluene) was spin-coated on the sample. The PMMA layer was also removed at the edges of the glass substrate as described above and the samples were cleaned under nitrogen flow (figure 6.3 b)).

A small piece of PDMS (\sim 4 mm x 4 mm, thickness: \sim 2 mm) was used as a stamp and gently pressed onto the GNP film (figure 6.3 c)). Next, a small amount of demineralized water (1-3 μ L) was applied to the glass substrate/PDMS interface. By thoroughly lifting the PDMS stamp with tweezers the water was guided between PDMS stamp and glass substrate and crept underneath the GNP film. Finally, the PDMS stamp could be removed with the GNP film on it (figure 6.3 d)).

Before transferring a GNP film onto the target PI substrate, the substrate was thoroughly cleaned in acetone, 2-propanol and demineralized water and subsequently treated with air plasma for two minutes. After plasma cleaning, the PDMS/GNP stamp was immediately placed onto the flexible PI substrate and it was ensured, that no air was trapped in the PI/GNP interface. In a next step, the PDMS stamp was pressed onto the PI substrate

6. Experimental Section

with a custom made press to ensure full contact between GNP film and target PI substrate 6.3 e). The substrate containing the PDMS stamp was then heated to 70 °C for seven minutes and subsequently cooled to 0 °C for another seven minutes to ease the removal of the PDMS stamp 6.3 f). After the PDMS stamp was detached, the sacrificial PMMA layer was removed by immersing the PI substrate into acetone and subsequent drying under nitrogen flow. In a final step, gold electrodes (thickness: 100 nm) were deposited via physical vapor deposition (PVD) onto the PI substrates using shadow masks 6.3 g)-h). Typically, canulas with diameters from 200 μm – 800 μm were used as shadow masks, however, for the lithographically structured GNP films custom designed shadow masks (fabricated by Beta LAYOUT GmbH, Germany) were used. Figure 6.3 i) shows an exemplary image of a GNP film with gold electrodes transferred onto PI.

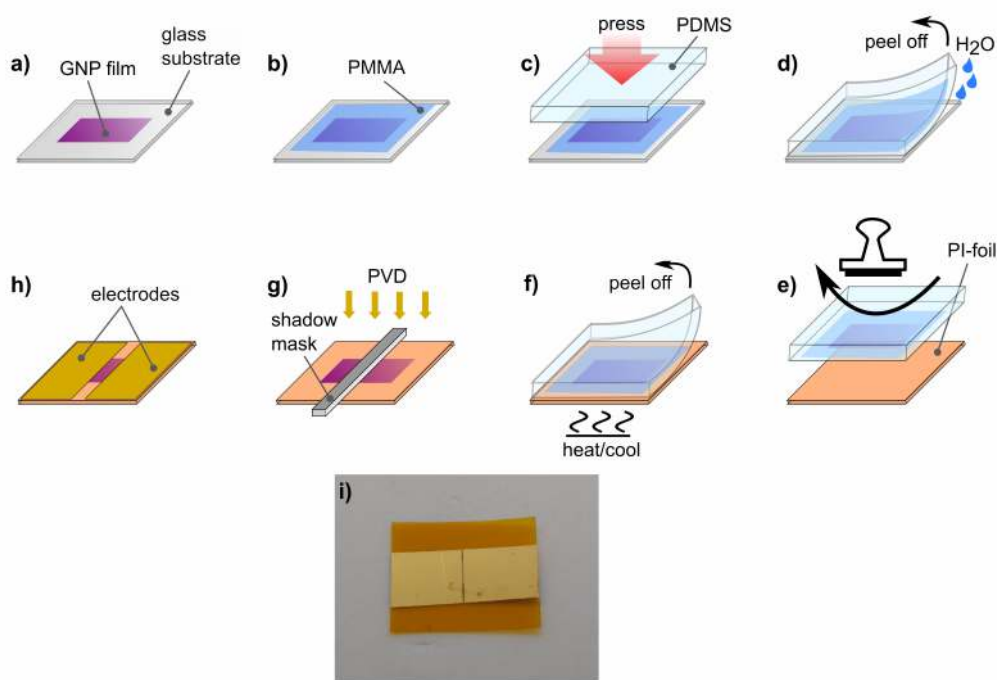


Figure 6.3: Schematics of the transfer process of GNP films onto PI flexible substrates. *a) – d)* depict the transfer mechanism from the glass cover slip to the PDMS stamp. *e), f)* show the transfer process onto the flexible PI substrate. *g), h)* depict the gold electrode deposition process via PVD. A representative image of a GNP film transferred onto PI foil with an electrode gap of 200 μm is shown in figure *i)*. Reprinted with permission from Ref. [62]. Copyright 2018 American Chemical Society.

Transfer onto Flexible Dragon Skin 30™ (DS) Substrates. First, flexible DS polymer substrates (thickness: 0.5 mm) were fabricated by mixing both silicon components (ratio 1:1, m:m) in a petri dish. To achieve the desired thickness, the petri dish was gently rotated at 500 rpm for 20 s using a spin-coater. After curing for 24 h, circular parts (diameter: 32 mm) were cut out and gold electrodes (thickness: 100 nm) were

deposited onto the DS substrate via PVD using custom designed shadow masks. Next, a glass piece containing a lithographically patterned GNP film was gently pressed onto the DS substrate containing the evaporated electrode structure. The glass substrate was thoroughly removed using a small amount of water as described above, yielding a GNP transducer transferred onto the electrode structure (6.4 a). Next, thin copper wires were fixated onto the electrode pads using silver conductive paste. After drying the paste for at least 2 h, a protective layer of liquid DS polymer was poured on top of the lower DS layer to fully cover the GNP thin film and the electrode structure, yielding a flexible sensor with a total thickness of ~ 2 mm (6.4 b).

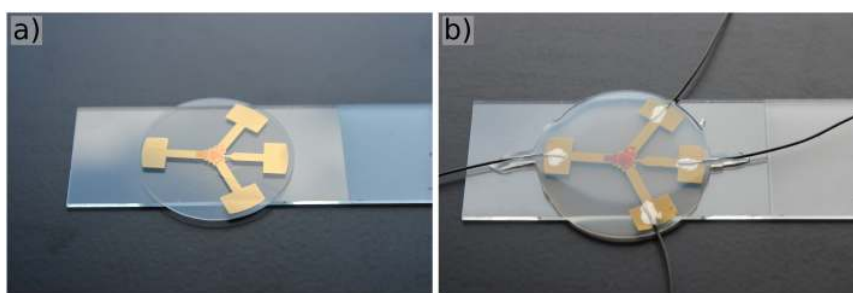


Figure 6.4: a) GNP film transferred onto flexible DS substrate with evaporated gold electrodes. b) Readily prepared DS sensor with GNP film transducer and wires fully embedded in the DS polymer. The wires are fixated onto the gold electrodes via silver conductive paste before embedding them in the DS polymer.

Fabrication of DUV Lithography Photomasks.

Materials and Apparatus. *Materials:* Quartz microscopy slides (Science Services, 25 mm \times 25 mm \times 1 mm), ammonia solution (Emsure, 28-30 %), hydrogen peroxide (Chemsolute, 30 %), AZnLOF 2020 (MicroChemicals), AZ 726 MF (MicroChemicals), potassium iodide (Merck, 99.5 %), iodine (own filling, 100 %), triammonium citrate (VWR, 99.4 %), TechniStrip NI555 (MicroChemicals).

Apparatus: Plasmasystem (Harrick Plasma, Plasma Cleaner PDC-32G), ultrasonic bath (PTIC-3-ES, Palsson), spin-coater (Süss MicroTec, LabSpin 6), hot plate (Harry Gestigkeit GmbH, PZ 28-2 SR), vacuum deposition system (Oerlikon Leybold Vacuum, UNIVEX 350G).

First, organic components were removed from quartz glass substrates by immersing them in a solution of $\text{H}_2\text{O}:\text{NH}_3:\text{H}_2\text{O}_2$ (5:1:1, v:v:v) for 20 min at 65 °C. Subsequently, 10 nm of titanium and 100 nm of gold were deposited onto the quartz substrate via PVD. Next, the substrate was coated with AZnLOF 2020 via spin-coating (3000 rpm, 60 s) and soft-baked for 60 s at 110 °C. The substrate was then selectively exposed to UV-light according to a pattern designed with Klayout (version 0.24.10). After exposure, a post-exposure

baking step was performed for 60 s at 110 °C. The photoresist was developed for 60 s using AZ 726 MF and rinsed with demineralized water. The gold layer at the exposed areas was removed in a solution of H₂O:KI:I₂ (400:4:1, v:v:v) for 5-7 min. The titanium layer was removed by immersing the quartz mask in a solution of 5 wt% triammonium citrate in H₂O₂ for 60 s at 40 °C. After rinsing the quartz mask with demineralized water, the residual photoresist was removed using TechniStrip NI555 at mild stirring (120 min, 80 °C).

6.2.2 Fabrication of Chemiresistors

Materials and Apparatus. *Materials:* 9DT (Alfa Aesar, 97 %), 4-mercapto-1-butanol (4M1OH) (Merck, 95 %), 3-mercaptopropionic acid (3MPA) (Merck, ≥ 99 %), 1-thioglycerol (TG) (Merck, ≥ 97 %), n-octane (Merck, 99 %), ethanol (VWR, 99.8 %), 1-propanol (Grüssing, 99.5 %), PI foil (Kapton, 200QR1; thickness: ~50 µm), conductive silver paste (PE873), nylon syringe filters (PureTech, Nylon030N0451, pore size: 0.45 µm). *Apparatus:* robotic dispensing system (Dispenser Tech Co., Ltd., DT-200F), homogeniser (Kennesaw, Omni Ruptor 4000), plasmasystem (Delta, TP04), inkjet printing system (MicroFab Technologies Inc., JetLab 4), multimeter (Hila, DM2630).

Fabrication of Fully Printed Flexible Chemiresistors. In a first step, conductive silver paste was homogenized for 3 min before an interdigitated electrode structure containing four fingers with a length of ~4.5 mm and a spacing of ~250 µm was printed on PI foil using a robotic dispenser system (nozzle diameter: 110 µm). Additionally, two electrode pads (3 mm × 3 mm, distance: 5 mm) were printed at the outer parts of the electrode fingers. After printing, the silver paste electrodes were sintered for 1 h at 100 °C. In a next step, the PI foil with the patterned electrodes was cleaned with air plasma for 90 s to allow a homogeneous deposition of the GNPs onto the substrate.

For the fabrication of fully printed GNP chemiresistors, two types of inks were used, namely a GNP ink and a cross-linker/ligand ink and deposited onto the substrate with an inkjet printing system (nozzle diameter: 50 µm). The nozzle was driven by a bipolar (positive, negative) pulse. For droplet ejection the rise time was set to 4 µs, dwell time, fall time and echo time were set to 3 µs, the final rise time was set to 2 µs, the dwell voltage was set to 20 and 25 V (for GNP ink and cross-linker ink, respectively) and echo voltage was set to -30 V. Before printing the GNP ink, it was filtered using nylon syringe filters. A variety of cross-linker inks consisting of either pure 9DT or 9DT with monothiols was used to interconnect the GNPs during the printing process (cf. table 6.3).

Table 6.3: Cross-linking mixtures used for inkjet printed GNP chemiresistors.

cross-linker/ligand	ratio [vol%]	solvent
9DT/-	100	n-octane
9DT/TG	50/50	1-propanol
9DT/TG	75/25	1-propanol
9DT/3MPA	50/50	1-propanol
9DT/3MPA	75/25	1-propanol
9DT/4M1OH	50/50	1-propanol
9DT/4M1OH	75/25	1-propanol

Both ink types were printed in an alternating sequence (i.e., GNP-(cross-linker)-GNP-(cross-linker), etc.). Each coating (GNP, cross-linker) consisted of four layers printed on the substrate (cf. figure 6.5). To obtain a fairly homogeneous coating the droplet spacing for each layer was set according to table 6.4. After each printed layer the moving direction of the printer stage was rotated 90°. To achieve the desired droplet spacings the moving speed of the printer stage was altered for each of the four layers (cf. table 6.4), because a constant ejection frequency of 500 Hz was maintained.

Table 6.4: Droplet spacing and movement speed for printed GNP and cross-linking layers.

layer	droplet spacing [μm]	moving speed [mm s^{-1}]
1	40	20
2	50	25
3	45	22.5
4	37	18.5

These parameters led to a droplet size of 45 to 65 μm in diameter at an ejection speed of 1-2 m s^{-1} . After each printed coating the resistance of the films were measured using a Hila DM2630 multimeter in order to monitor the formation of the GNP films during the printing process. Finally, after printing, the sensors containing only 9DT as cross-linker were immersed in the respective 9DT cross-linker ink for 12 h at room temperature. Sensors fabricated using mixtures of 9DT and a monothiol (cf. table 6.3) were immersed in the respective 9DT/monothiol ink for one hour. In a final step each sensor was washed with n-octane and ethanol, dried and subsequently stored under nitrogen atmosphere. Figure 6.5 shows a sketch of a fabricated sensor containing interdigitated electrodes and the structure of the GNP film with its GNP and cross-linker coatings and layers.

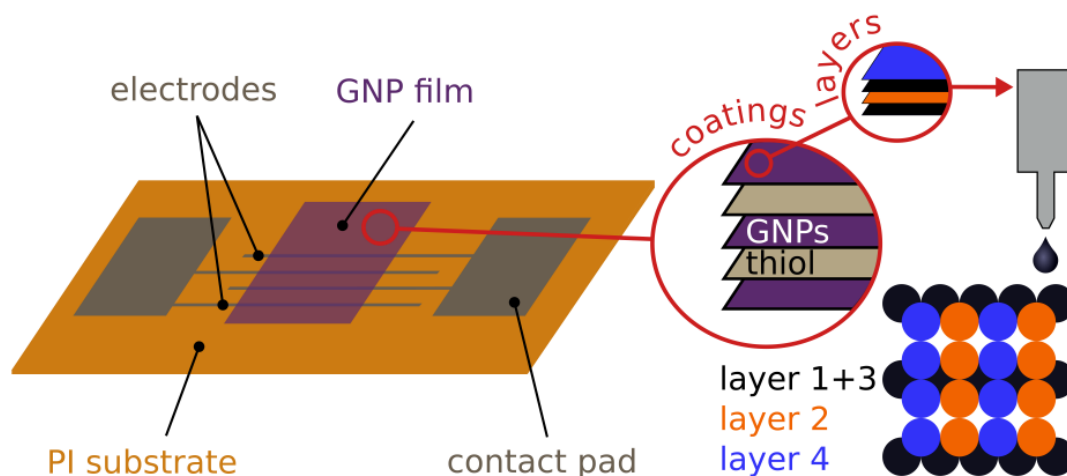


Figure 6.5: Schematics of the inkjet printing process showing the mesh-like structure of the printed layers building up a coating. First, a coating of GNPs consisting of four layers was printed. Next, a coating of dithiol cross-linking ink was deposited the same way. This process was repeated until a total of five coatings was printed. Adapted with permission from Ref. [81]. The material was modified compared to the original figure shown in the publication.

6.3 General Characterization

In this chapter general characterization methods for GNP stock solutions, GNP films and sensor comprising of cross-linked GNPs are described. It has to be noted that due to their fabrication process not all sensors could be characterized identically.

6.3.1 UV-Vis Absorbance Spectroscopy

To estimate the particle concentration of obtained GNP stock solutions, absorbance spectra were recorded using a UV/Vis spectrometer (Varian Cary 50). A typical measurement was performed using quartz glass cuvettes (optical path length: 10 mm). The GNPs were diluted with the respective solvent of the stock solution. All measured spectra were corrected for background absorbance by recording a baseline spectrum of the respective solvent. The concentration of the GNP stock solution was obtained by using the formula presented by Haiss et al.^[184]

Furthermore, fabricated GNP films on glass substrates were analyzed to estimate the homogeneity of the films. Therefore, the substrate was placed in a custom-built sample holder perpendicular to the incident beam and spectra at four different spots were acquired.

6.3.2 Transmission Electron Microscopy (TEM)

Ligand-stabilized GNPs were prepared for TEM analysis as described in chapter 6.1.1. Next, 3 times 10 μL were deposited onto a carbon film covered TEM copper grid and the excessive solution was removed after 30 s. Cross-linked GNPs were prepared for TEM analysis by floating the glass cover slip supported GNP film on a water surface for at least 16 h. After gently pressing down the cover slip, a floating GNP film was obtained and skimmed from the water surface using a carbon film covered TEM copper grid. All samples were measured with a Jeol JEM-1011 (LaB₆ cathode, acceleration voltage: 100 kV). To determine the average diameter of the particles at least 500 GNPs were evaluated using ImageJ software. Particles with a diameter below 1 nm were excluded from the statistics and the circularity was set to a range of 0.6.^[185]

6.3.3 Scanning Electron Microscopy (SEM)

SEM images were acquired from GNP films on various substrates such as silicon wafers and carbon film covered TEM copper grids. Measurements were performed using a Leo 1550 (Zeiss) at operating voltages from 5 kV to 20 kV.

6.3.4 Atomic Force Microscopy (AFM)

AFM measurements were performed using a Digital Instruments Multimode AFM scanner and a JPK Nanowizard AFM. The AFMs were operated with ACTA and NSG01 cantilevers, respectively. Measurements were conducted by operating in intermittent contact mode. Height profiles and membrane thicknesses of fabricated GNP film samples were extracted. For this purpose the films were scratched to obtain sharp edges.

6.3.5 X-Ray Diffractometry (XRD)

For XRD measurements, GNPs were spin-coated and cross-linked as described above (chapter 6.2.1) onto silicon XRD substrates. XRD diffractograms were recorded using a PANalytical X'PERT Pro diffractometer. The diffractometer was equipped with a copper anode (λ 1.54 Å) and operated at 45 kV, 40 mA. A baseline correction was performed by subtracting a diffraction pattern of a blank XRD substrate from the obtained data.

6.3.6 Small Angle X-Ray Scattering (SAXS)

Small angle X-Ray scattering (SAXS) measurements were performed on GNP films transferred onto PI. The setup is equipped with an Incoatec – X-ray source I μ S and a Quazar Montel optics. The wavelength of the incident X-ray beam was 1.54 Å and the size of the spot on the sample was 0.6 mm². Samples were placed on a motorized sample stage and were measured using a Rayonix SX165 CCD-detector. The measurement time was set to 10 min and data evaluation was done using Scatter software. Measurements were performed in cooperation with Dr. Andreas Meyer (Institute of Physical Chemistry, University of Hamburg).

6.3.7 X-Ray Photoelectron Spectroscopy (XPS)

For XPS measurements, GNPs were deposited and cross-linked via spin-coating as described above (chapter 6.2.1) onto unoxidized silicon wafer substrates. Measurements were performed using a high-resolution two-dimensional delay line detector. The incident radiation was provided by a monochromatic Al K α X-ray source (photon energy: 1486.6 eV, anode operating at 15 kV). The data was recorded in fixed transmission mode. A pass energy of 20 eV was chosen, resulting in an overall energy resolution better than 0.4 eV. A flood gun was used to compensate charging effects and binding energies were calibrated based on the graphitic carbon 1s peak at 284.8 eV.^[186] Measurements were performed in cooperation with Dr. Heshmat Noei and Dr. Michael Wagstaffe (X-Ray Physics and Nanoscience, DESY, Hamburg).

6.3.8 Charge Transport Measurements

Charge transport measurements were performed using a Keithley source measurement unit (SMU) 2601A and an Agilent 4156c parameter analyzer. Measurements were performed on various substrates and the GNP films were electrically contacted using gold-coated micro probes or spring-loaded contact pins. Current voltage (I - V) curves were recorded by applying voltages from ± 5 V and measuring the resulting current. Typically, these measurements were carried out at room temperature.

To determine charge transport activation energies of GNP films, further measurements were performed at cryogenic temperatures (100–300 K). To this end, the samples were

loaded into a custom-built test cell provided with four power resistances acting as heating elements. The test cell was then sunk into a Dewar flask filled with liquid nitrogen. Temperatures were measured via Pt100 thermistors. A custom-designed microcontroller-based unit controlled the heater power via a PID loop. Before cooling down to 100 K the test cell was heated to room temperature for 30 min to evaporate water from the sample surface and to prevent further condensation while cooling down the sample. After cooling down to 100 K a custom-written python software automatically controlled the heating of the test cell and performed I - V -measurements via a Keithley 2601A SMU, when desired temperatures were reached. For activation energy measurements solely GNP films prepared on glass cover slips were used. A more detailed description of the cryocell used for activation energy measurements is given in the appendix chapter A.1.

6.4 Chemiresistor Measurements

Materials and Apparatus. *Materials:* 1-propanol (Grüssing, 99.5 %), n-octane (Merck, 99 %), 4M2P (Merck, 98.5 %), 1-butanol (Alfa Aesar, 99 %), ethanol (VWR, 99.8 %), toluene (VWR, 99.6 %), demineralized water (18.2 M Ω cm, ELGA LabWater, PURELAB flex System), nitrogen 5.0 (Linde).

Apparatus: gas calibration system (Umwelttechnik MCZ GmbH, Kalibriersystem Model CGM 2000), SMU (Keithley Instruments, 2601A), multimeter (Keithley Instruments, 2002).

Chemiresistor measurements were carried out using fully printed GNP films with interdigitated electrode structures (see chapter 6.2.2) and is schematically shown in figure 6.6. The samples were placed in a custom-made metal cell (total volume: \sim 10 mL) capable to read out eight sensors simultaneously. A gas calibration system was used to generate a variety of analyte vapors of different concentrations (25–2000 ppm) (n-octane, toluene, 4M2P, 1-butanol, 1-propanol, ethanol, water) and nitrogen (quality 5.0) was used as carrier gas. A constant flow rate of 400 mL min⁻¹ through the test cell was set. After exposing the sensors to analyte vapor for 240 s, they were purged using carrier gas for 480 s. Each of the sensor samples was connected in series with a commercial surface mount device (SMD) resistor (tolerance: 0.1 %) acting as a shunt to read out the resistive responses upon analyte exposure. To this end, a constant bias of 5 V was applied using a Keithley 2601A sourcemeter. The shunt resistor readout was carried out using a mul-

timer (Keithley 2002). The voltage drops at the shunt resistors were used to calculate the resistive responses of the sensor samples according to following equation:

$$R_{\text{Sensor}} = \frac{V_{2601A} - V_{\text{Shunt}}}{V_{\text{Shunt}}/R_{\text{Shunt}}} \quad (6.1)$$

Here, R_{Sensor} is the resistance of the chemiresistor sample, V_{2601A} is the voltage applied using the Keithley 2601A SMU, V_{Shunt} and R_{Shunt} are voltage measured at the shunt resistor and the shunt resistor's resistance, respectively. Sampling rate for the chemiresistor readout was set to 0.5 Hz.

Figure 6.6 schematically shows the chemiresistor measurement setup and an image of the test chamber containing seven printed GNP chemiresistors used for characterization.

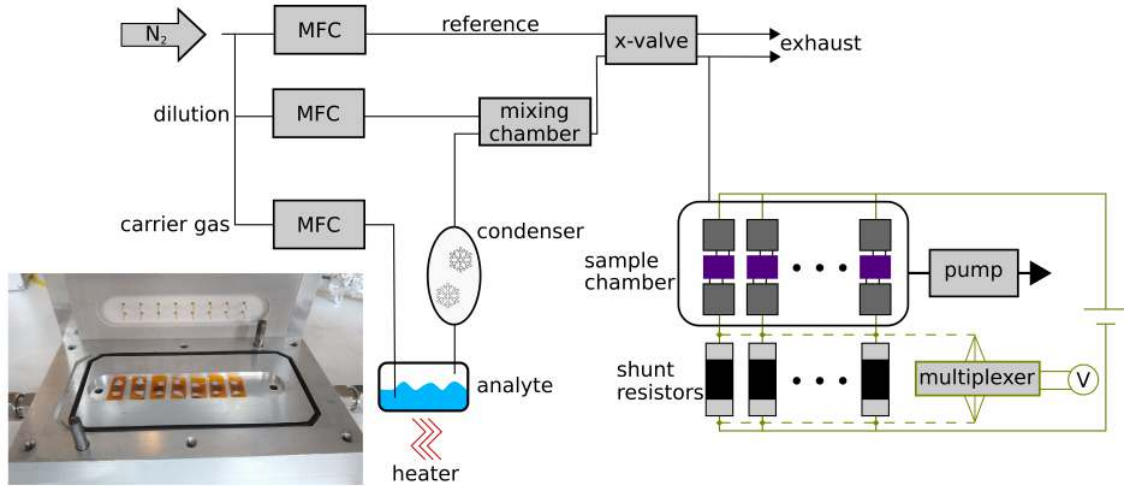


Figure 6.6: Scheme of the measurement setup for chemiresistive measurements. An image of the test chamber containing seven sensors is shown in the lower left. Reprinted with permission from Ref. [81].

6.5 Strain Measurements

Materials and Apparatus. *Materials:* Instant glue (Uhu), glass-reinforced epoxy laminate FR4 material (thickness: 1.6 mm, 0.8 mm).

Apparatus: Custom-built four point flexural bending setup, SMU (Keithley Instruments, 2601A).

Before performing strain measurements, PI-supported GNP sensors were fixed onto FR4 material. For this purpose, the FR4 stripes (160 mm × 10 mm × 1.6 mm) and discs

(diameter: 60 mm, thickness: 0.8 mm) were roughened in their center using abrasive paper and the sensor samples were glued onto it using instant glue. It has to be noted that the rectangular GNP films were fixed onto FR4 stripes and discs (cf. figure 6.7 a), b), whereas the lithographically patterned samples were solely fixed onto the circular shaped FR4 discs (cf. figure 6.7 c).

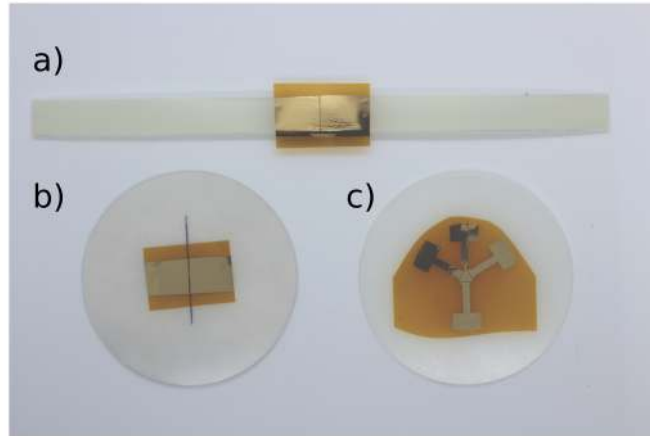


Figure 6.7: Images of samples used for strain measurements. a) Two electrode geometry with mechanically structured GNP film on FR4 stripe. b) Two electrode geometry with mechanically structured GNP film on FR4 disc. c) Lithographically patterned GNP film with four electrodes on FR4 disc.

Next, the FR4-supported sensors were inserted in a custom-built four point flexural bending setup. A detailed description of the bending setup can be found in the appendix, chapter A.2. Since the dimensions of the FR4 substrates differ from each other, the distance of the top and bottom pins of the bending setup were set differently for each type of FR4 substrate (stripe, disc). For the FR4 stripes the top and bottom pins were set to a distance of 40 mm and 80 mm, respectively. For the FR4 discs the top and bottom pins were set to a distance of 20 mm and 40 mm, respectively. The sensors were electrically contacted via crocodile clips at small freestanding straps at the edges of the gold covered PI foil. A commercial strain sensor (Omega, SGT-1/350-TY11) was used as reference and measured simultaneously to the sample to determine the applied strain. For a typical measurement the top pins were lowered for 1 mm using a stepper motor resulting in a total strain of $\sim 0.12\%$ – $\sim 0.25\%$, depending on the distances between the pins of the bending setup.

To measure the resistive responses of the sensors a constant bias of 5 V was applied using a Keithley 2601A sourcemeter for both sensors, the GNP sample and the reference.

Since the lithographically patterned sensor samples are equipped with four electrodes (cf.

figure 6.7 c), they were electrically contacted using a custom-built microcontroller-based multiplexer device based on reed relays, applying a 5 V bias in an alternating manner between each electrode and the ground electrode. During measurements conducted with samples supported by FR4 substrate discs, no additional reference sensor was measured simultaneously. Instead, this measurement was performed once before to obtain reference strain values for sensor samples on FR4 disc substrates. The electrical readout and stepper motor control were linked using a custom python routine. All measurements were performed under ambient conditions.

6.6 Nanomembrane Bulging

Materials and Apparatus. *Materials:* Demineralized water (18.2 M Ω cm, ELGA LabWater, PURELAB flex System), silicon wafers (Silicon Materials, SEMI standard prime, thickness: 300 ± 10 μm , orientation: (100); both sides polished; n-doped, resistivity: 1–10 Ωcm), ACTA AFM cantilevers (JPK Instruments, $k \sim 40$ Nm^{-1} , $f_0 \sim 300$ kHz), NSG01 AFM cantilevers (NT-MDT Spectrum Instruments, $k \sim 5.1$ Nm^{-1} , $f_0 \sim 150$ kHz), 9DT (Alfar Aesar, 97 %), 1,6-hexanedithiol (6DT) (VWR, 96 %), 1,4-butanedithiol (4DT) (Sigma Aldrich, 97 %), BDT (Sigma Aldrich, 99 %), sulfuric acid (VWR, 95 %), hydrogen peroxide (Merck, 30 %), double sided sticky tape (TESA, 05338).

Apparatus: Optical Microscope (Olympus, BH2-UMA), AFM (JPK, Nanowizard), pressure sensor (Sensortech, HDIM100DUF8P5, range: 1 – 10 kPa), pressure sensor (Sensortech, HDIB001DBF8P5, range: -100 – 100 kPa).

To fabricate GNP films for nanomembrane bulging, GNPs were deposited onto glass cover slips and cross-linked via spin-coating as described in chapter 6.2.1 using three spin-coating cycles (cf. figure 6.8 a) i, b). GNPs of different sizes (~ 4 nm, ~ 8 nm) and a variety of cross-linkers (9DT, 6DT, 4DT, BDT) were used for film fabrication. Next, the glass cover slips were cut into quarters and ~ 0.5 mm of the edges of the GNP films were removed from the substrate. Subsequently, each quarter was floated on demineralized water (~ 20 mL). The substrate-supported film remained floating for approximately 16 h and eventually the film could gently be detached from the substrate by pressing down the substrate edges with tweezers. Thereby, the GNP nanomembrane remained floating on the water surface.

Circular apertures (diameter: 80 μm) were etched into the silicon substrates using deep reactive ion etching (DRIE). The etching was conducted by N. Schulz at Technische

Universität Hamburg according to the Bosch process. Next, the wafers were cleaned in a mixture of sulfuric acid and hydrogen peroxide (3:1, v:v) for 1 h at 85 °C. After rinsing with demineralized water and drying in a nitrogen flow, the silicon substrates were used to skim the floating GNP nanomembranes from the water surface (cf. figure 6.8 a) ii, c) and thereby spanning it across the aperture (cf. figure 6.8 a) iii, d). The samples dried for several hours under ambient conditions.

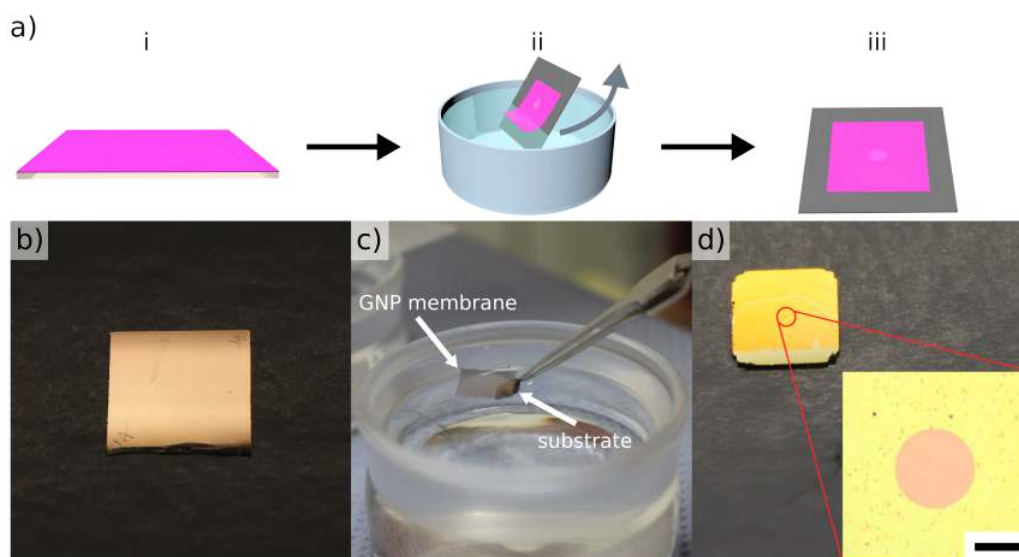


Figure 6.8: a) Schematic illustration of the skimming process. First, a GNP film on glass (i) was floated onto the surface of water. After the glass substrate sank to the bottom, the GNP film could be skimmed with a wafer containing an aperture (ii) and was subsequently dried (iii). Figure parts b) – d) show images of the process schematics from figure part a) i–iii. The inset in figure part d) depicts a micrograph of a GNP nanomembrane spanned across an 80 μm aperture. Scale bar: 50 μm .

After drying, the samples were inspected for defects at the edges of the aperture via optical microscopy. The samples were then taped onto custom-built sample holders (cf. 6.9 a) using double sided sticky tape, which were then screwed onto a testing stage. The consecutive zoom in figure 6.9 b) shows the GNP nanomembrane spanned across the 80 μm aperture. AFM scans ($100 \mu\text{m} \times 100 \mu\text{m}$) in intermittent contact mode were performed by recording ten line profiles at a scanning speed of $44.6 \mu\text{m s}^{-1}$ as it is schematically depicted in figure 6.9 c). Underpressures ranging from 100 Pa up to ~ 70 kPa were created by the backpressure of nitrogen passing two needle valves and controlled using two pressure sensors with different detection limits. For each scan, critical stress and strain data were obtained using the circular-fit method described in chapter 5.2.5 and the pressure was increased until the nanomembranes collapsed. All measurements were performed under ambient conditions.

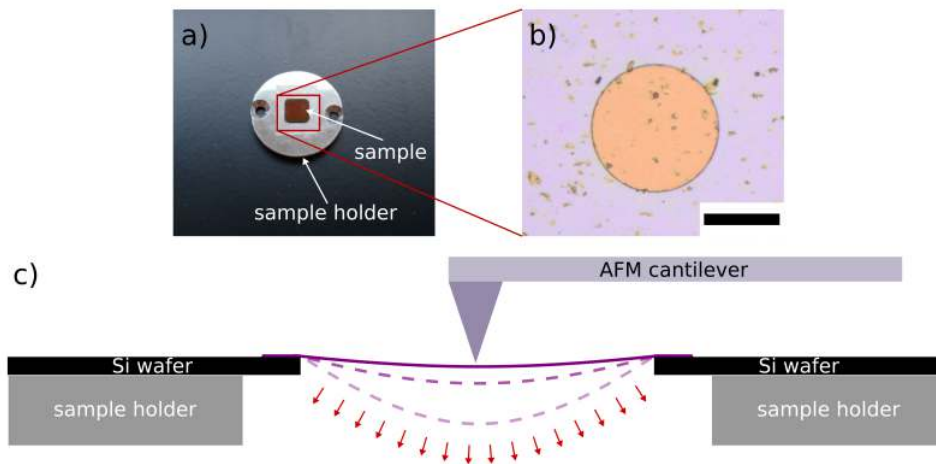


Figure 6.9: a) Wafer substrate with an 80 μm aperture taped onto a metallic sample holder with an 1 mm aperture in the center. b) Zoom-in to the center of the wafer substrate. The 80 μm aperture as well as the GNP membrane spanned across it are clearly visible as can be seen by the change in color. Scale bar: 50 μm . c) Schematic of the bulge experiment. The AFM cantilever scans the membrane in intermittent contact mode. After each scan the underpressure is increased and the membrane is further deflected (dashed lines).

6.7 Pulse Wave and Gesture Measurements

For pulse wave and gesture measurements, DS supported GNP strain sensors equipped with four electrodes were used (cf. chapter 6.2.1). Pulse wave measurements were performed by positioning a sensor probe onto the lower side of the wrist above the radial artery. The sensor was fixated onto the arm using a bracelet made of hook and loop fastener (cf. figure 6.10 a). The gesture measurements were performed by taping the sensor onto the back of the wrist using medical tape as shown in figure 6.10 b).

For electrical readout, the four electrodes of the sensor were connected to a custom-built WiFi enabled printed circuit board. The data were displayed and recorded using a custom python routine. Test persons signed an informed consent according to a form provided by TU Delft^[187] and all data were anonymized. The document is provided in the appendix A.10.

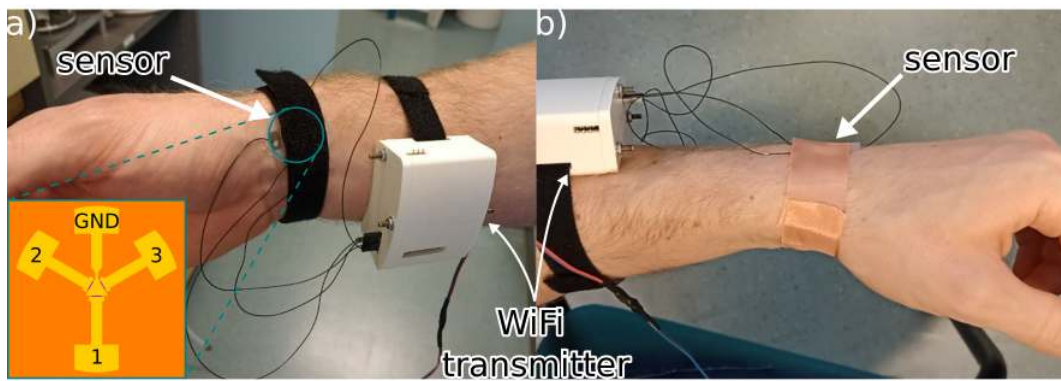


Figure 6.10: Flexible DS supported strain sensor mounted on the wrist. A custom-designed circuit board rendered electrical read out possible and transmitted the data via WiFi to a remote computer. *a)* Position for pulse wave measurements. The inset shows a schematic of the sensor geometry with its four electrodes (GND, 1, 2, 3). *b)* Position for gesture measurements.

7 Results and Discussion

7.1 Strain Sensors

The anisotropic response behavior of GNP strain gauges is controversially discussed in literature.^[39,40] This phenomenon comprises of two relevant parameters, i.e., the geometric effect and the piezoresistive effects which influence the composite. Primary (axial) strains as well as the transversal strains depending on the Poisson ratio of the underlying substrate and the GNP composite have to be considered. Furthermore, purely geometric effects have to be well separated from the influence of strain (axial as well as transversal) on the charge transport mechanism (tunneling and percolation). To this end 9DT cross-linked strain sensors with different geometries were fabricated onto PI foil and their angular dependent strain sensitivity was studied. Various bending experiments were performed at angles ranging from 0° to 180° in steps of 15° . Additional mechanical finite element simulations were performed to evaluate the axial and transversal strains acting on the GNP composite. An analytic model accounting for geometric and piezoresistive effects was fitted (cf. equation 5.15) to the experimental data and axial and transversal gauge coefficients (g_{11} and g_{12}) were extracted. In this context it should be noted, that materials having high gauge factors of some hundreds up to some thousands, geometric effects are negligible, whereas for bulk metal-based strain gauges with low gauge factors piezoresistive effects can be ignored. For GNP-based sensors, however, which have intermediate gauge factors of some tens up to one hundred, both effects should be considered separately. Finally, a triaxial sensor was fabricated by embedding lithographically structured GNP films into a highly flexible polymer to monitor physiological signals such as pulse waves and limb movement and was read out via a custom-built circuit.

Characterization of the Anisotropic Response of GNP-Based Strain Gauges.

For this study, particles with a mean diameter of ~ 7 nm were fabricated according to a synthesis route presented by Peng et al.^[61] and were dissolved in n-heptan resulting in a stock solution with a concentration of $\sim 5 \mu\text{mol L}^{-1}$. The particle concentration was determined according to a method presented by Haiss et al.^[184] UV/vis spectra, size statistics and TEM images of the two used syntheses (S1, S2) are depicted in figure 7.1. The dilution factors f for the UV/vis samples were $1/300$ and $1/600$, respectively and a

cuvette with an optical path length of 1 mm was used. The characteristic surface plasmon resonance (SPR) at ~ 517 nm can be seen.

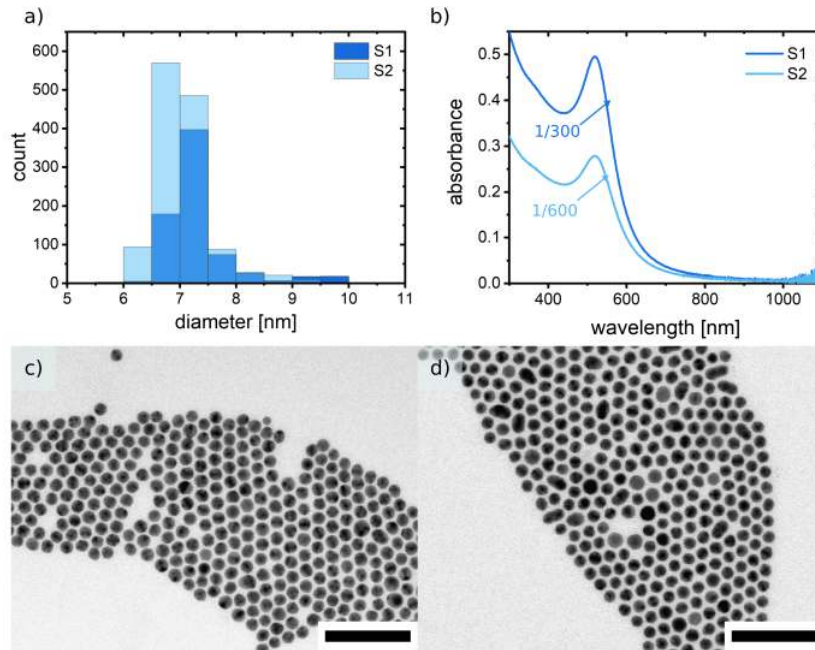


Figure 7.1: a) Size histograms of the GNP synthesis (S1, S2) used to fabricate strain sensors. b) UV/vis spectra of GNP solutions with the respective dilution factors as indicated. Figure parts c) and d) depict TEM images of ligand stabilized GNPs used in this study. Scale bars: 50 nm.

GNP films were fabricated via spin-coating and cross-linked using 9DT. Rectangular shaped films with a width B of 2.4 mm were transferred via contact printing onto flexible PI foil and electrode structures with different gap sizes L (200, 400, 800 μm) were evaporated onto the material. To characterize the anisotropic strain behavior, the sensors were glued onto circular shaped FR4 substrates. Figure 7.2 a) schematically shows the rectangular shaped GNP film on PI foil. Figure parts 7.2 b) and c) exemplarily show an optical micrograph of a sensor with a 200 μm gap and an image of such sensor glued onto the FR4 disc, respectively.

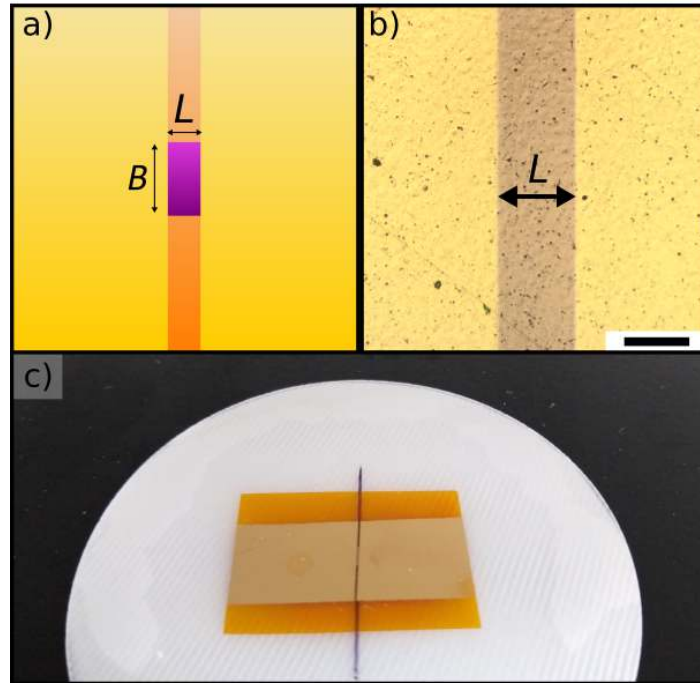


Figure 7.2: a) Schematics of rectangular shaped GNP films on PI foil with a width B and a length L . b) Optical micrograph of a sensor with an electrode of $200\ \mu\text{m}$. Scale bar: $200\ \mu\text{m}$. c) Image of a GNP sensor with an electrode gap of $200\ \mu\text{m}$, used for angle dependent strain measurements, glued onto a FR4 substrate disc. The black line was for orientation.

To test the angular responses to strain, the FR4-supported sensors were deflected in a custom-build four-point bending test setup (cf. figure 7.3 a). A detailed description of the bending setup is given in the appendix chapter A.2. The anisotropy of the responses was tested by performing bending experiments at each angle of rotation θ between 0° and 180° at steps of 15° . Here, θ defines the relative orientation of the principal strain axis (PSA) defined by the bending setup (cf. figure 7.3 a) with respect to the overall bias direction of the sample. During a measurement, the FR4 substrate disc was deflected by the upper (inner) two moving supports down by Δs (cf. figure 7.3 b). A constant bias of $5\ \text{V}$ was applied to the sample while bending and the resulting current was measured.

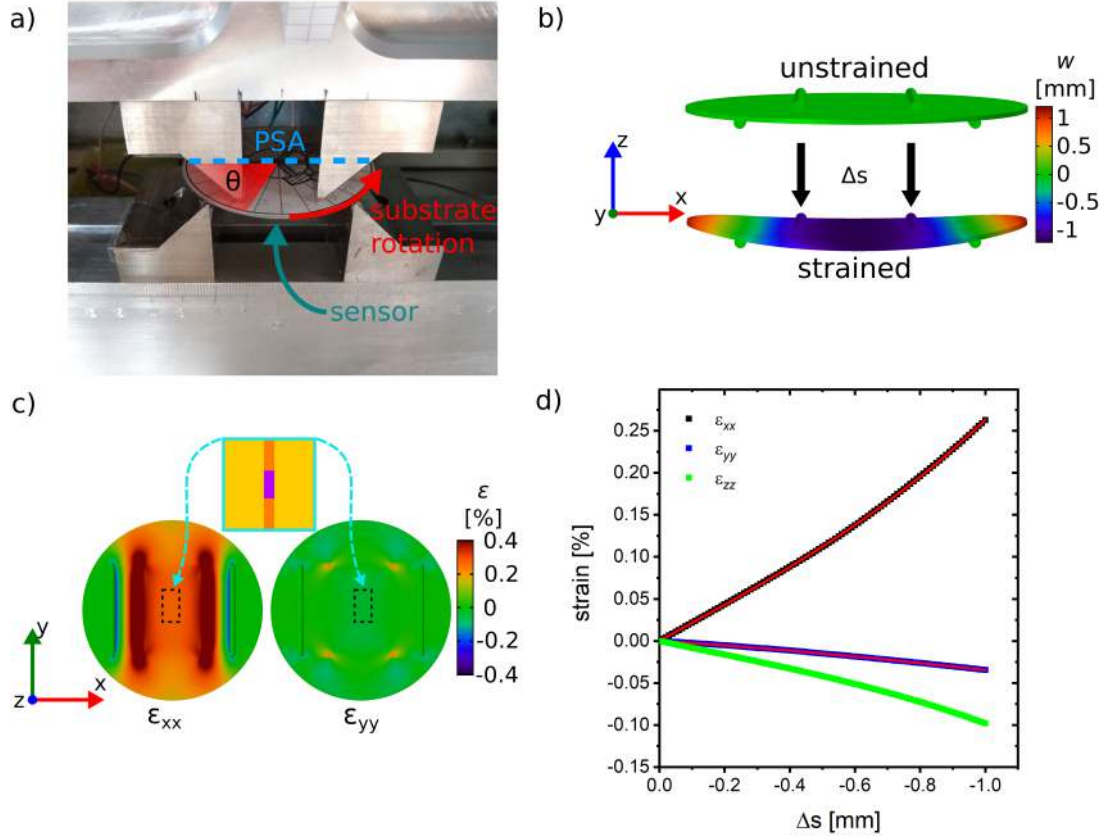


Figure 7.3: a) Image of a FR4 substrate inserted in the four-point flexural bending setup. The top two supports are lowered to deflect the sample along the PSA as indicated by the dashed blue line. The sample is consecutively rotated counterclockwise in steps of $\theta = 15^\circ$ (red arrow) and the sensor is located at the center of the lower side of the substrate as indicated by the arrow. b) Simulated deflections of the FR4 substrate's initial (top) and final (bottom) strained state after moving the top supports by $\Delta s = -1$ mm. c) Strains in x and y direction ϵ_{xx} and ϵ_{yy} , respectively, after a maximum deflection of $\Delta s = -1$ mm. A cut-off at $\epsilon = 0.4$ % was made for better visibility. It can be seen, that the location of the sensor (indicated by the arrows) is homogeneously strained. d) Plots depicting the strains ϵ_{xx} , ϵ_{yy} and ϵ_{zz} acting on the sample as a function of the deflection height Δs . The strain values shown correspond to a point at the center of the lower side of the FR4 substrate's surface.

Simulation of the Strain Acting on the GNP Composite. A FEM Comsol simulation was employed to simulate surface deflections, which are shown in figure 7.3 b). Here, a circular shaped FR4 substrate is depicted in its initial relaxed and final bending state during the experiment. The parameters of the FR4 substrate for this simulation were as follows: thickness: 0.8 mm, diameter: 60 mm, Young's modulus E : 22 GPa,^[188] Poisson ratio ν : 0.15 (Comsol library). The color bar indicates the z deflection w before and after the supports were lowered by a distance Δs of 1 mm to deflect the FR4 substrate. The resulting strains at the lower side of the FR4 substrate in x and y direction (ϵ_{xx} , ϵ_{yy}) are shown in figure 7.3 c). As can be seen from the data, the spot, where the sensor is located (indicated by the arrows and dashed outlines) is homogeneously strained.

Next, the data obtained from the simulation were used to determine the strains acting on the GNP film during deflection. These strains are a key aspect for the analysis of the anisotropy of the sensors' resistive responses. To extract a continuum of the strains ϵ_{xx} and ϵ_{yy} , mechanical simulations were performed for values of Δs ranging from 0 to -1 mm in steps of -0.01 mm. Since the flexible GNP/PI sample was directly attached to the FR4 substrate it was assumed, that strains acting in x and y direction were solely governed by the deformation of the FR4 substrate. The z dimension of the GNP film, however, can freely deform. Due to the Poisson effect it is expected that the GNP is compressed. To consider this compression, the z strain of the GNP film is computed according to equation 7.1, taking into account a Poisson ratio ν_{film} of ~ 0.33 , which is commonly used for organically stabilized GNP composites.^[148,189,190]

$$\epsilon_{zz} = -\nu_{film} \left(\frac{\epsilon_{xx} + \nu_{film}\epsilon_{yy}}{1 - \nu_{film}^2} \right) - \nu_{film} \left(\epsilon_{yy} + \nu_{film} \left(\frac{\epsilon_{xx} + \nu_{film}\epsilon_{yy}}{1 - \nu_{film}^2} \right) \right) \quad (7.1)$$

In figure 7.3 d) graphs showing the bending-induced strains along all three axes $\epsilon_{xx}(\Delta s)$, $\epsilon_{yy}(\Delta s)$ and $\epsilon_{zz}(\Delta s)$ calculated for a sensor sample placed in the center of the lower FR4 substrate's surface are depicted. While the strains along the x direction ϵ_{xx} are the most prominent with ~ 0.26 % at maximum deflection, smaller values of -0.035 % and -0.098 % for the compressive strains ϵ_{yy} and ϵ_{zz} were found, respectively. The differences in compressive strains along the y and z directions are attributed to the different Poisson ratios of the substrate (responsible for y-compression) and the GNP film (responsible for z-compression) of 0.15 and 0.3, respectively. For further model calculations the simulated strains $\epsilon_{xx}(\Delta s)$ and $\epsilon_{yy}(\Delta s)$ were fitted using a third-degree polynomial fitting as indicated by the solid red lines shown in figure 7.3 d).

Evaluation of Bending Experiments. Three representative strain response curves of a sensor sample with an electrode gap L of 200 μm and a channel width B of 2.4 mm are shown in figure 7.4 a) at angles of $\theta = 0^\circ$, 45° and 90° . The inset shows a schematic of the sensor's relative bias orientation (dashed green line) to the setup's PSA (solid green line) at the angle θ . For the measurement of each strain response curve the sample was deflected to a maximum strain of $\epsilon_{xx} = 0.26$ % along the setup's PSA and subsequently relaxed to its initial state ($\epsilon_{xx} = 0$ %). Strain values were obtained from Comsol simulations based on the displacement Δs , as described above. For further analysis the model fitting was performed in the linear regime up to 0.12 %. Up to this point, both responses of a commercial sensor (SGT-1/350-TY11, Omega) and the simulation show linear behavior when plotted against the displacement Δs (cf. appendix figure A.3 a).

As expected, the sensor is most sensitive ($\Delta R/R_0 = \sim 3\%$ at $\Delta s = -0.55$ mm) at an angle θ of 0° when the overall bias direction is aligned with the PSA of the setup. At $\theta = 45^\circ$, the relative change in resistance decreases to $\sim 2\%$ as the sensor's bias direction is rotated out of the PSA. Even at $\theta = 90^\circ$ a non-zero relative change in resistance of $\sim 1\%$ is measured for 0.12% applied strain. One could now define the anisotropy as the ratio of the relative changes in resistance at sensor orientations of $\theta = 0^\circ$ and $\theta = 90^\circ$ with respect to the PSA. According to that a value of ~ 3 is found (cf. figure 7.4 a), which is in good agreement to a value of ~ 3.2 indicated by the data presented by Jiang et al.^[39]

Figure 7.4 b) shows the relative changes in resistance $\Delta R/R_0$ at a strain of $\epsilon_{xx} = 0.12\%$ for angles θ measured between 0° and 180° for a sample with an electrode gap L of $200\ \mu\text{m}$. This plot as well shows that the angular dependent sensor response decreased until an angle of 90° and increased again until the sensor was aligned in parallel to the setup's PSA at $\theta = 180^\circ$. Similar results were found for sensor samples with electrode gaps L of $400\ \mu\text{m}$ and $800\ \mu\text{m}$, respectively, proving that within this geometric size scale the variation of the electrode gap length has no significant influence on the sensors' strain sensitivity. Corresponding plots of sensors with $400\ \mu\text{m}$ and $800\ \mu\text{m}$ electrode gaps are shown in the appendix in figure A.3 b) and c).

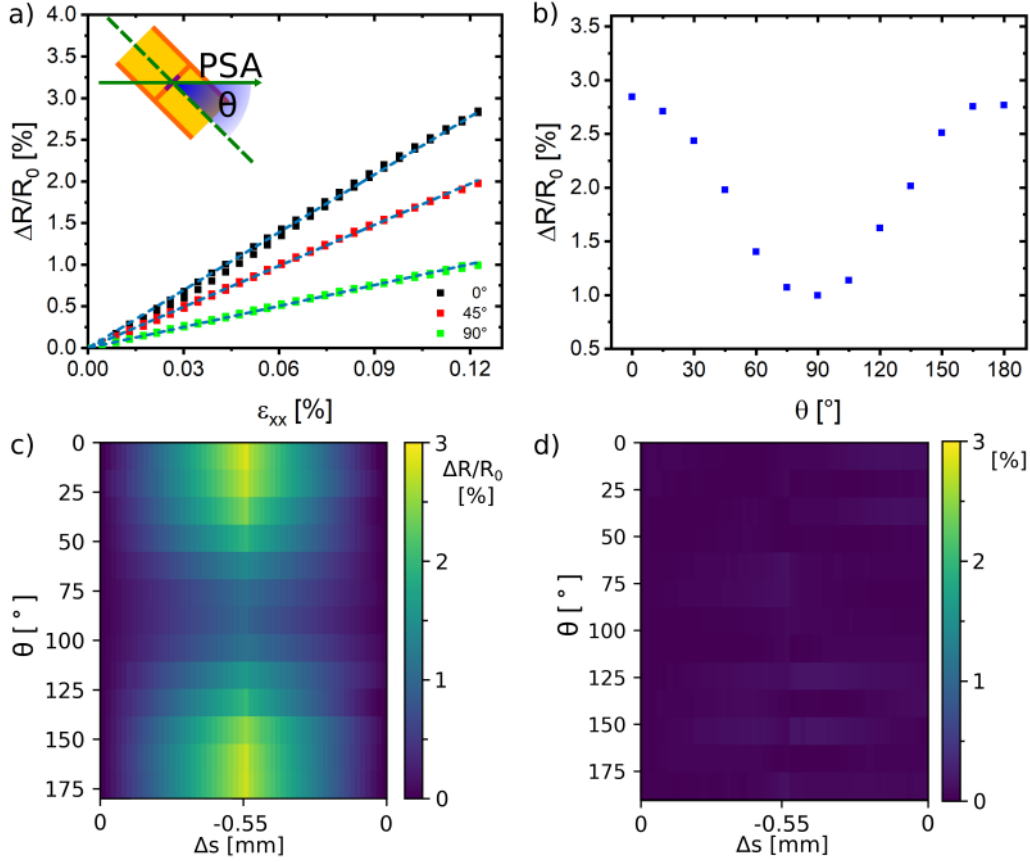


Figure 7.4: a) Measurements performed with a sensor sample at angles $\theta = 0^\circ$, 45° and 90° with a $200 \mu\text{m}$ electrode gap. The dashed lines depict linear fits as an guide to the eye. The inset shows a sketch of the sensor with its primary axis (dashed lines) rotated out of the setup's PSA (solid lines) at the angle θ . b) Relative changes in resistance plotted against the rotational angle θ at a strain of $\epsilon_{xx} = 0.12\%$. c) 2D plot depicting the measured data of a rectangular shaped sensor sample. Measurements were performed at angles θ from $0^\circ - 180^\circ$ in steps of 15° at a bending range (Δs) corresponding to the linear regime shown in figure part a). d) Absolute error between the analytical fitting function and the measured data shown in figure part c). The overall residual error is below 0.13% .

For the determination of the anisotropic strain response of the sensor, strains acting parallel and perpendicular to the overall current direction, ϵ'_{xx} and ϵ'_{yy} , respectively, were calculated. These strains depend on both the angular orientation of the sensor to the PSA (cf. figure 7.4 a) inset) and the strain imposed by the bending setup. According to a coordinate transformation shown in equations 7.2 and 7.3 ϵ'_{xx} and ϵ'_{yy} could be calculated from the global strains applied by the bending setup.

$$\epsilon'_{xx} = \frac{\epsilon_{xx} + \epsilon_{yy}}{2} + \frac{\epsilon_{xx} - \epsilon_{yy}}{2} \cos(2\theta) + \epsilon_{xy} \sin(2\theta) \quad (7.2)$$

$$\epsilon'_{yy} = \frac{\epsilon_{xx} + \epsilon_{yy}}{2} + \frac{\epsilon_{xx} - \epsilon_{yy}}{2} \cos\left(2\left(\theta + \frac{\pi}{2}\right)\right) + \epsilon_{xy} \sin\left(2\left(\theta + \frac{\pi}{2}\right)\right) \quad (7.3)$$

As described above, ϵ_{xx} and ϵ_{yy} are the strains in the global coordinate system of the bending setup obtained from the Comsol simulations and ϵ'_{xx} and ϵ'_{yy} are the strains acting parallel and perpendicular to the overall current direction of the sensor sample. The angle θ describes the rotation of the sensor out of the bending setup's PSA. For this experiment the shear strain ϵ_{xy} is small, which was further confirmed by Comsol simulations and is three orders of magnitude lower than the strains ϵ'_{xx} and ϵ'_{yy} (cf. appendix figure A.4). Hence, the sine terms in the coordinate transformations are assumed to be zero. Note, that no coordinate transformation is necessary for the strain along the GNP film's z-direction, hence, $\epsilon'_{zz} = \epsilon_{zz}$.

The 2D plot shown in figure 7.4 c) depicts all strain response measurements from $\theta = 0^\circ$ to $\theta = 180^\circ$ in 15° steps performed with a sensor sample having an electrode gap L of $200 \mu\text{m}$. A model based on ϵ_{xx} and ϵ_{yy} obtained from the Comsol simulations, ϵ_{zz} (cf. equation 7.1), the coordinate transformations according to equations 7.2 and 7.3 and the gauge coefficients g_{11} and g_{12} (cf. equation 5.15) was used to fit the measured data. With this model, the GNP sensor's sensitivity towards axial and transversal strain with respect to the overall current direction could be described and eventually the piezoresistive gauge coefficients g_{11} and g_{12} could be extracted. Figure 7.4 d) shows the residual error of the fit and indicates that the applied model well fits the obtained data from the experiments. The overall residual error between the experiments and the fit is $\sim 0.13 \pm 0.11 \%$.

Table 7.1 provides the axial and transversal gauge coefficients g_{11} and g_{12} for sensors with different electrode gaps L ranging from $200 \mu\text{m}$ to $800 \mu\text{m}$. The gauge factors were obtained from fitting the data up to strains of $\epsilon_{xx} = 0.12 \%$.

Table 7.1: Axial and transversal gauge coefficients (g_{11} and g_{12}) for rectangular shaped GNP strain sensors with different electrode gaps.

electrode gap [μm]	g_{11}	g_{12}
200	33.4	22.3
400	32.5	20.9
800	31.2	19.4

According to these results, the sensors exhibit an anisotropic strain response behavior, however, having a non vanishing sensitivity when being strained perpendicular to the overall current direction. These results are attributed to the fact, that the GNPs form disordered films during the spin-coating fabrication process. When a bias is applied, pre-

ferred percolation pathways for the charge carriers are formed. In this context, Müller et al. thoroughly described the effect of percolation paths in three dimensions for the conductivity of GNP composites.^[107] Concerning the charge transport, such percolation pathways can be split into parallel and perpendicular (detours) components with respect to the overall current direction, which is also discussed by Jiang et al. in their study on GNP films.^[39]

However, inconsistent results were found by Zhao et al. They observed relative changes in resistance one order of magnitude higher when the device was strained perpendicular to the overall current direction compared to relative changes in resistance when the device was strained parallel to the overall current direction.^[40] Contradictory to that, Jiang et al. found relative changes in resistance which are three times higher when the device is strained parallel to the overall current direction, which goes hand in hand with the assumption that charge carriers primarily move along the bias direction leading to higher sensitivities in a parallel orientation. Furthermore, the findings of Zhao et al. are indeed astonishing, because GNPs used by them were smaller (2–5 nm) compared to GNPs used in the study of Jiang et al. (7–12 nm). In both studies, GNPs were stabilized with a similar type of linker, namely mercaptic acids. According to the commonly accepted semi-empiric model correlating the relative change in resistance to the applied strain (cf. equation 5.13) one would expect that sensors made from larger particles exhibit higher sensitivities to strain, which was confirmed in various studies.^[36,62,191] In summary, the sensitivity to parallel and perpendicular strain differs in both studies. Also the sensitivity of sensors made from the smaller GNPs presented in the study of Zhao et al. is greatly increased compared to the results presented by Jiang et al., where larger particles were used. This does not follow the commonly accepted microscopic model for GNP strain sensors (cf. equation 5.13).

The gauge factors found by Zhao et al. are ~ 225 for strains applied perpendicular to the overall current direction, which is rather uncommon for GNP-based strain sensors.^[62,63] Such high gauge factors are commonly attributed to crack formation during the deflection of the nanoparticle strain sensor, which indeed is an established method to tune the sensitivity of nanoparticle strain gauges.^[192] Moreover, electrodes used to contact the GNP transducers need to be designed in a way to ensure that the material does not fail during the bending experiment. In the study of Zhao et al., however, interdigitated copper electrodes were employed having ~ 300 nm thick and $6 \mu\text{m}$ wide electrode fingers.^[40] In this context it can not be excluded that the fragile design of the electrode patterns lead to a physical malfunction due to crack formation, especially when the devices were deflected perpendicular to the overall current direction, namely along the length of the electrode fingers. Here, breaking of the electrodes finger could then explain such high gauge factors.

Employment of Triaxial Strain Sensor. Based on the comprehensive characterization of the strain anisotropy of GNP-based strain gauges, a triaxial sensor is presented made from a lithographically patterned GNP film transferred onto PI foil. The sensor comprised of three transducing elements aligned in an angle of 120° and four gold electrodes (GND, 1, 2, 3; cf. figure 7.5 a). The resistive read-out was performed with a custom-built multiplexer device based on reed relays to alter the bias at the terminals between 0 and 5 V and measuring the resulting current. Figure part 7.5 b) shows a stitched optical micrograph of the sensor's electrode structure with arrows indicating the current flow, as well as the PSA and the angle θ . This sensor enables distinct measurements of angles between 0 and 180° exhibiting a unique triplet of resistive responses from the transducers R_1 , R_2 and R_3 .

In figure 7.5 c), these responses are depicted as a function of the angle θ and the relative changes in resistance are shown for strains $\epsilon_{xx} = 0.26\%$. As expected, the signal period restarts after 180° and a phase shift of the sensor responses of 60° can be observed (cf. figure 7.5 c), d) for the transducers aligned in an orientation of 120° . It should be noted, that since the goal of these measurements was to show the angular dependent sensor response, the resistive responses at maximum strains of ϵ_{xx} of 0.26% are shown.

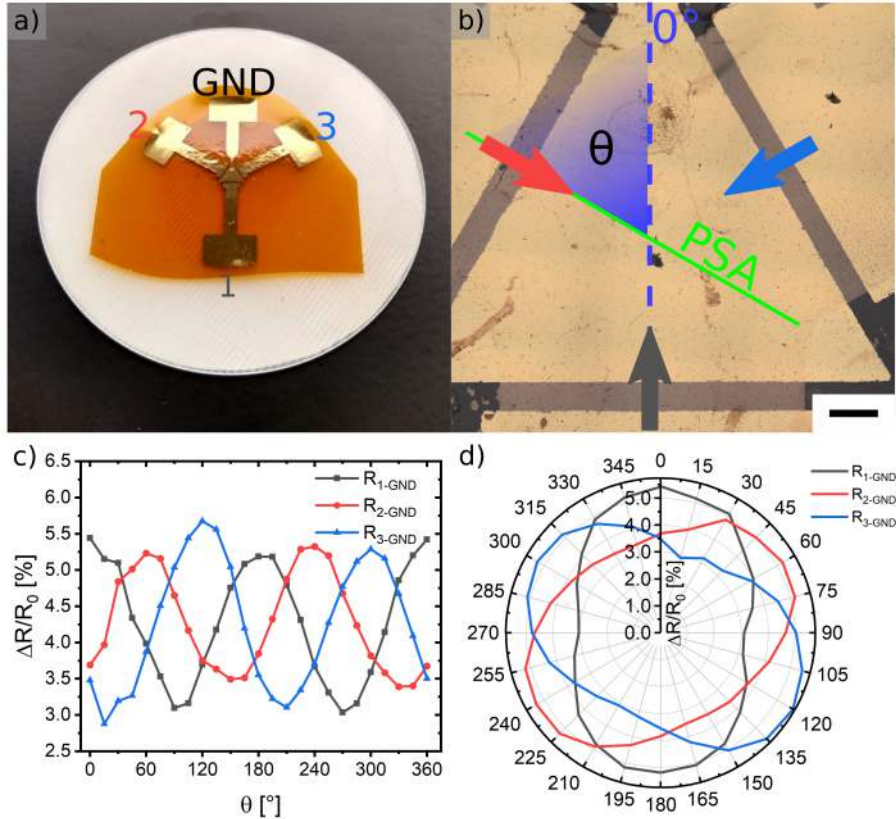


Figure 7.5: a) Image of a triaxial strain gauge on Pi foil glued onto a circular FR4 substrate. The resistance between the electrodes 1, 2, 3 was measured against the ground electrode (GND) at each step of deflection. b) Stitched optical micrograph of the electrode structure and the three transducing elements. The arrows indicate the current flow to the central ground electrode, the dashed blue line marks the PSA at 0°, the solid green line marks the PSA at 60°. c) Relative changes in resistance at a maximum strain of $\epsilon_{xx} = 0.26$ % plotted against the angle θ ranging from 0° to 360° in steps of 15°. d) Polar plot of the data shown in figure part c).

Highly Flexible Strain Sensors for Health Care Applications. In this study the importance of low-cost and facile fabrication health care monitoring sensors, e.g. for pulse wave measurements and limb motion, is emphasized by further presenting a triaxial strain sensor on a highly flexible Dragon Skin 30 (DS) polymer (cf. figure 7.6 a). For the fabrication of such sensor, first, a lithographically structured GNP film was transferred onto a thin layer of DS containing evaporated gold electrodes (thickness: 0.5 mm) via transfer printing. Second, thin copper wires were glued onto such electrode pads using silver conductive paste. Finally, liquid DS was poured onto the sensor and dried for 16 h embedding the electrodes and the GNP transducers in a 1.5 mm thick polymer layer making it highly robust against mechanical stresses and other external influences, e.g. by sweat. Since the elastic modulus of the Dragon Skin 30 polymer is in the range of $\sim 0.25 - 0.6$ MPa,^[193,194] it is in the range of the elastic modulus of human skin (< 0.3 MPa).^[195]

This feature renders DS well-suited as a substrate for skin-mounted devices, because the matching elastic moduli minimize shear forces and motion artifacts caused by the detachment of the sensor when the polymer is fixated on the skin. Moreover, the high flexibility of the DS polymer allows the detection of even faint deformations of the skin. The sensor geometry also allows time-efficient mounting of the sensor onto the artery for pulse wave measurements. Here, no exact alignment is necessary, since the sensor contains three differently oriented transducers to ensure that at least one sensor part can clearly resolve the human pulse wave.

To measure human pulse waves, the DS sensor was fixated onto the wrist, above the radial artery and connected to a custom-built readout device, digitalizing the recorded data and transmitting it via Wi-Fi to a remote computer (cf. figure 7.6 b). Pulse wave measurements were performed continuously before (at rest) physical exercise and after physical exercise (20 squats, large peaks in top panel of figure part 7.6 c). The lower panels in figure part 7.6 c) depict zoom-in graphs of the transients before and after the execution of 20 squats. The pulse frequency before and after the exercise were determined to be 60 bpm and 96 bpm, respectively. The pulse wave could further be highly resolved exhibiting details such as the percussion wave (PW), tidal wave (TW) and dicrotic wave (DW). The sensor responses of sensor S1–S3 prove, that the redundancy of three sensors always ensure a precise measurement of the pulse wave. Whereas sensor S1 only gives a weak response, sensor S2 and S3 clearly measured pulse wave signals.

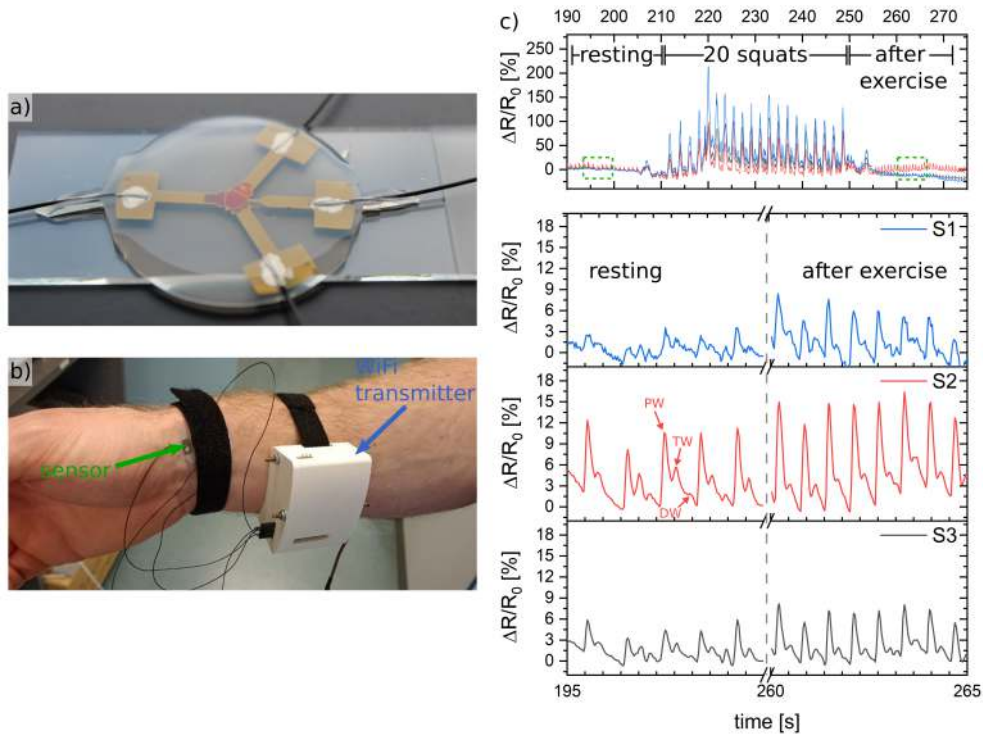


Figure 7.6: a) Image showing the triaxial sensor. A lithographically patterned GNP film is transferred and embedded into DS polymer. The polymer further protects the electrodes and the electrode/wire interfaces from being separated, providing a highly robust sensor. b) Image of the DS supported sensor fixated onto the wrist above the radial artery. The sensor is connected to a custom-built electrical read-out system and a Wi-Fi transmitter. c) Top panel: overall time trace of a pulse wave measurement recorded before, during and after physical exercise (20 squats). The green shaped areas mark regions which are depicted in the lower panels. Lower panels: Zoom-in of the pulse wave sequences recorded by sensor S1-S3 before and after physical exercise. The increase in pulse frequency as well as distinct features of the pulse wave such as the percussion wave (PW), the tidal wave (TW) and the dicrotic wave (DW) can clearly be seen.

Next, the sensor was employed to detect different limb motions and hand gestures. To this end, the sensor was mounted on top of the wrist (cf. figure 7.7 a, grey frame) using medical tape. Responses of all three sensor parts were recorded. Limb motions were recorded by moving the wrist to the four positions (colored frames, i-iv) shown in figure 7.7 a). Compared to the wrist's initial stance (cf. figure 7.7 a) i) resistive responses of three additional positions were measured (figure 7.7 a) ii-iv). After each position i-iv, the wrist was kept stable for several seconds before moving to a new position.

The sensor responses, as well as the different positions of the wrist were used as input parameters for a linear discriminant analysis (LDA). First, several movements were performed to train the LDA model following a set of test measurements. The LDA was performed using the LinearDiscriminantAnalysis algorithm provided by the sklearn (version 0.24.2) python (version 3.9.0) library. Figure 7.7 a) clearly shows, that all four

positions of the wrist could be well discriminated from each other. Here, light colored cross markers depict the training data and darker triangular-shaped markers depict the results obtained from the test measurements.

The sensor further allows to discriminate finger movements, as it is shown in figure 7.7 b). After repeatedly performing finger counts (cf. figure 7.7 b) i-iv) and returning to the initial position of the wrist (figure 7.7 a), grey frame) a second LDA model was trained and fitted to a set of test data. Except the finger count "two" (cf. figure 7.7 b) ii), which was hardly distinguishable from the initial position, all other finger counts could be well discriminated.

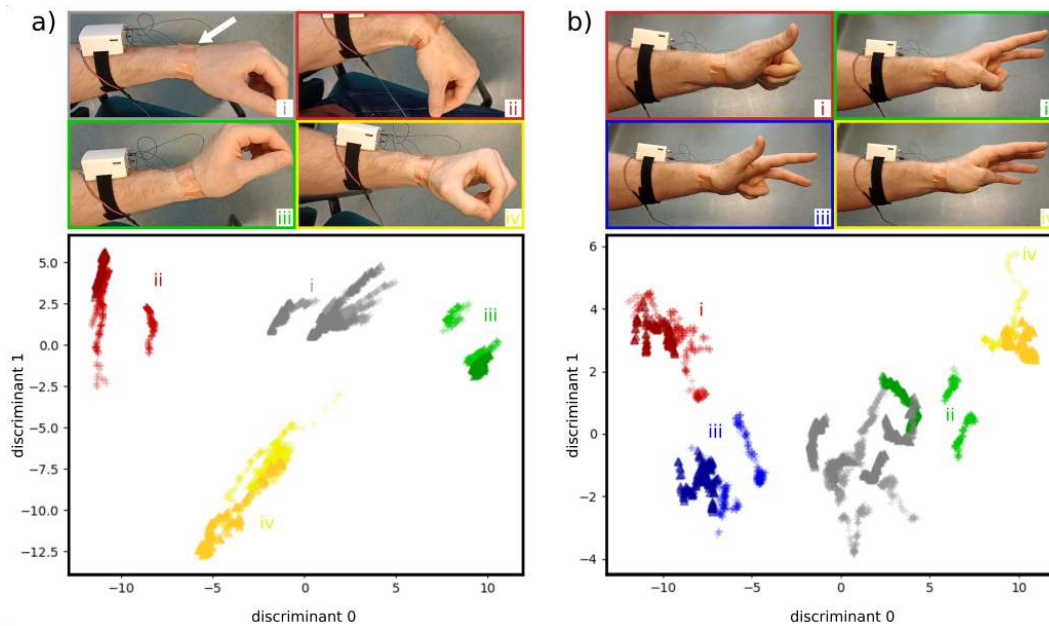


Figure 7.7: Measurements performed with a sensor mounted on top of the wrist (white arrow in image i in figure part a). a) Images i-iv depict hand positions (colored frames). Here, the initial hand position is shown in the grey frame. The plot shows an LDA analysis of the recorded sensor data. b) Images i-iv in colored frames depict different hand counts, while recording the responses of the triaxional sensor. The plot shows the LDA analysis of the different finger counts. In both LDA plots, light colored crosses denote the data used for fitting the LDA, while darker triangles depict the test data.

Summary. In this study, an in-depth analysis of anisotropic strain response behavior of GNP-based strain gauges is presented. Rectangular shaped two-electrode sensors with different aspect ratios were fabricated and responses to strains at different directions with respect to the overall current direction were measured. FEM modeling in combination with an improved mathematical model was employed to separate piezoresistive and geometric sensor responses. According to the model, parallel (g_{11}) and perpendicular (g_{12}) piezoresistive gauge coefficients, describing the anisotropic sensor response were extracted.

Values of 32.4 ± 1.1 and 20.9 ± 1.5 were found for g_{11} and g_{12} , respectively. Furthermore two possible health care applications of a lithographically patterned DS supported triaxial sensor were presented. Pulse wave analysis measurements exhibited high-resolution pulse waves with distinct features (PW, TW, DW). Measurements were performed before and after physical exercise resulting in pulse wave frequencies of 60 bpm and 96 bpm, respectively. The sensor was also employed to detect and discriminate wrist movements and finger counts using an LDA to cluster the respective sensor responses for each position of the wrist and hand count sign. The sensor was read out with low cost commercially available equipment.

7.2 Chemiresistors

GNP-based gas sensors are well suited for the detection of volatile organic compounds (VOCs), e.g. released by the human body. The sensors are highly sensitive because of their high permeability, as well as their perturbation-sensitive charge transport based on thermally activated charge carrier tunneling.^[129] Moreover, these composites exhibit short response and recovery times and offer the possibility to be operated at room temperature at low power consumption.^[196] As described in chapter 5.2.4, the chemical selectivity of such sensors can be tuned by functionalizing the GNPs with different ligands or cross-linkers. However, the efficient fabrication and patterning of GNP-based chemiresistors remains a challenging task. Among a variety of fabrication methods (cf. chapter 5.2.1) inkjet-printing offers a resource-efficient approach, which allows fast on demand changes of geometric features of the device.

In this study, a new fabrication protocol for fully printed GNP-based chemiresistors with tunable selectivities is presented. The fabricated chemiresistors were characterized regarding their electrical properties and were further arranged in a sensor array to study their response patterns to different analytes by dosing them with vapors of solvents ranging from nonpolar (hydrophobic) to polar (hydrophilic) nature.

For this work, particles with a mean diameter of ~ 7 nm, synthesized according to a procedure by Peng et al., were used.^[61] The particles were dissolved in n-octane resulting in a GNP ink with a concentration of $\sim 4.5 \mu\text{mol L}^{-1}$. The particle concentration was determined according to a method presented by Haiss et al.^[184] Figure 7.8 provides a size histogram of the used particles, as well as a UV/vis absorbance spectrum showing the characteristic surface plasmon peak at 517 nm. The dilution factor for the preparation of

the UV/vis sample was 1/300 and a cuvette with an optical path length of 10 mm was used. Further, TEM images depict oleylamine stabilized GNPs at different magnifications.

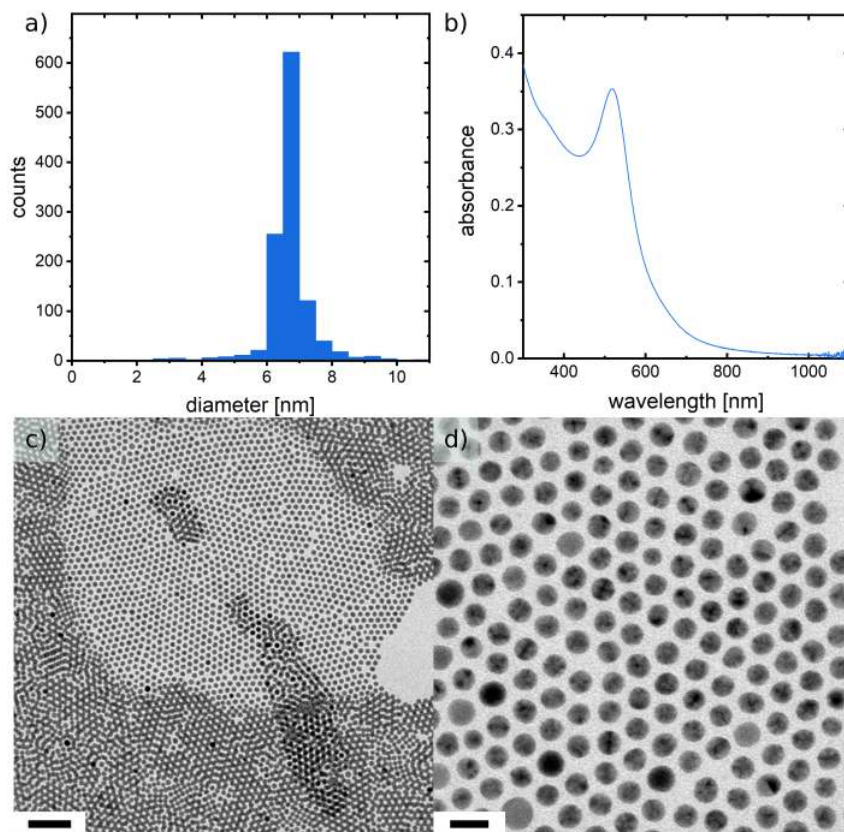


Figure 7.8: a) Size histogram of the GNPs used for ink fabrication. Particle diameters of 6.7 ± 0.7 nm were determined via TEM analysis. b) UV/vis absorbance spectrum of GNP ink. Figure parts c) and d) depict TEM images of ligand stabilized GNPs at different magnifications. Scale bars: c) 50 nm, d) 10 nm. Adapted with permission from Ref. [81]. The material was modified compared to the original figure shown in the publication.

To obtain fully printed GNP chemiresistors, two printing processes were combined. First, dispenser printing was used to print interdigitated electrode structures onto PI foil using silver conductive paste. Second, the GNP film transducer was deposited onto such electrode structure via layer-by-layer (LbL) inkjet-printing, which is thoroughly described in chapter 6.2.2. Fairly homogeneous films were obtained by rotating the deposition direction by 90° after each printed layer and altering the printing speed between $18.5 - 25 \text{ mm s}^{-1}$. After four layers of GNPs were deposited, the same printing procedure was repeated using a cross-linker ink (or monothiol/dithiol blends) consisting of 9DT in n-octane. The concentration was adjusted, to yield a 1000-fold excess of cross-linker molecules with respect to the GNPs. To promote solvent evaporation and increase cross-linking reactions, inkjet-printing was performed at a constant temperature of 37°C . The dithiol cross-linkers

can easily replace the original amine ligands of the GNPs due to the formation of strong Au-S bonds^[100] and robust cross-linked GNP networks are formed.^[30] Fully printed sensors were obtained (cf. figure 7.9 a) exhibiting a mesh-like pattern, as can be seen in figure 7.9 b), resulting from the printing process.

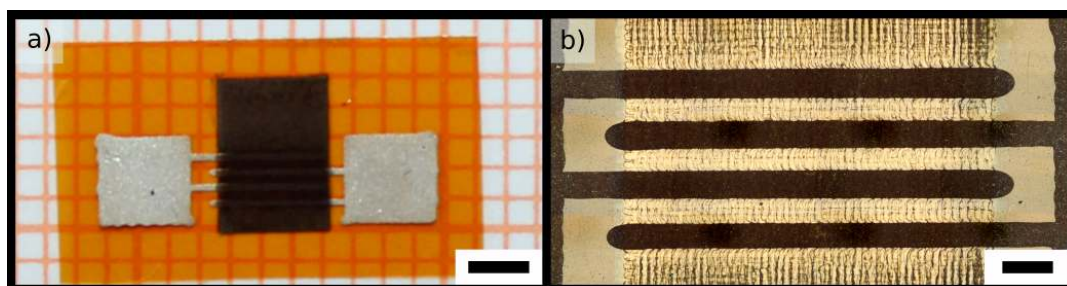


Figure 7.9: a) Optical photograph of fully printed GNP chemiresistor on PI foil (orange). The dispenser printed interdigitated silver paste electrodes and the inkjet-printed GNP film (dark rectangle) can clearly be discriminated. b) Optical micrograph showing the overlap region of the electrode fingers. The mesh-like structure of the printed GNP film is clearly visible. Scale bars: a) 2 mm, b) 500 μm . Adapted with permission from Ref. [81]. The material was modified compared to the original figure shown in the publication.

To allow a facile read-out of the chemiresistive devices, it was preferable to fabricate samples with baseline resistances in the low megohm range. For this purpose, multiple layers of GNPs and linker ink were printed to achieve a certain thickness of the nanomaterial. The sample shown in figure 7.9 was fabricated by printing 3×4 layers of GNPs and 2×4 layers of 9DT, resulting in a baseline resistance of 0.7 MOhm. In figure 7.10 a), the resistances of four sensor devices made from 9DT cross-linked GNPs depending on the amount of coatings (note: 1 coating = 4 layers) are shown. The figure shows, that with increasing number of coatings the baseline resistance decreases, resulting in similar baseline resistances below 1 MOhm after three coatings of GNPs for all shown devices. According to these findings all sensors used in this study were fabricated by printing three coatings of GNPs. To exchange the amines of the top GNP coating with the mono-/dithiols and to enhance the cross-linking of the GNPs throughout the whole film, all samples were immersed in the respective thiol ink before testing their gas sensing properties. It has to be noted, that data points shown in figure 7.10 a) represent resistances measured before the samples were immersed, whereas the inset shows IV-curves measured after sensors passed through the last immersion step. Since the slope of the curves corresponds to a resistance of ~ 0.7 MOhm it can be concluded, that the last immersion step has no significant influence on the final baseline resistance.

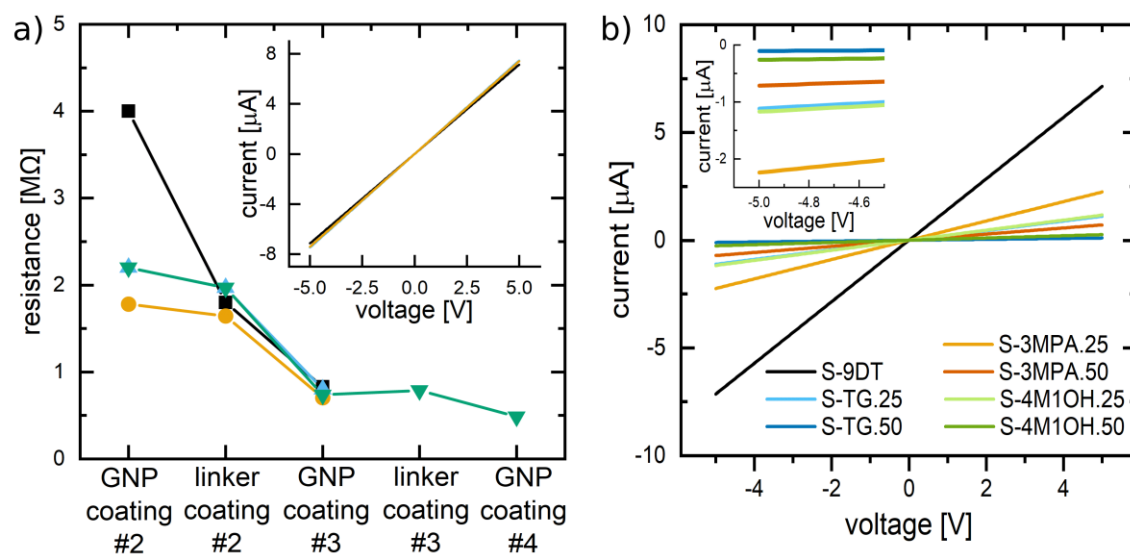


Figure 7.10: a) Baseline resistances of four samples of 9DT cross-linked GNPs as indicated by four different symbols (black, blue, green, orange). Each coating (GNP/linker) consisted of four inkjet-printed layers. Resistance measurements were conducted directly after printing at a temperature of 37 °C. The IV-curves shown in the inset were recorded after finally immersing the printed films in the cross-linker ink. Note, that after printing one coating of GNPs the baseline resistance was too high to be measured. b) IV-curves of chemiresistors used in this work. The 9DT cross-linker ink contained different monothiols (L) in various concentrations as indicated in table 7.2. All IV-curves shown were measured after immersing the samples in the respective 9DT or 9DT+L ink. Adapted with permission from Ref. [81]

For a more detailed view on the morphology of the printed GNP films, SEM images are provided in figure 7.11. Here, one can see that on the micrometer scale a fairly homogeneous film is obtained. However, higher magnifications show a granular structure, most likely due to clustering of the GNPs. Similar results were reported by our group's former work for 9DT cross-linked GNPs deposited onto polyethylene (PE) via LbL self-assembly.^[63]

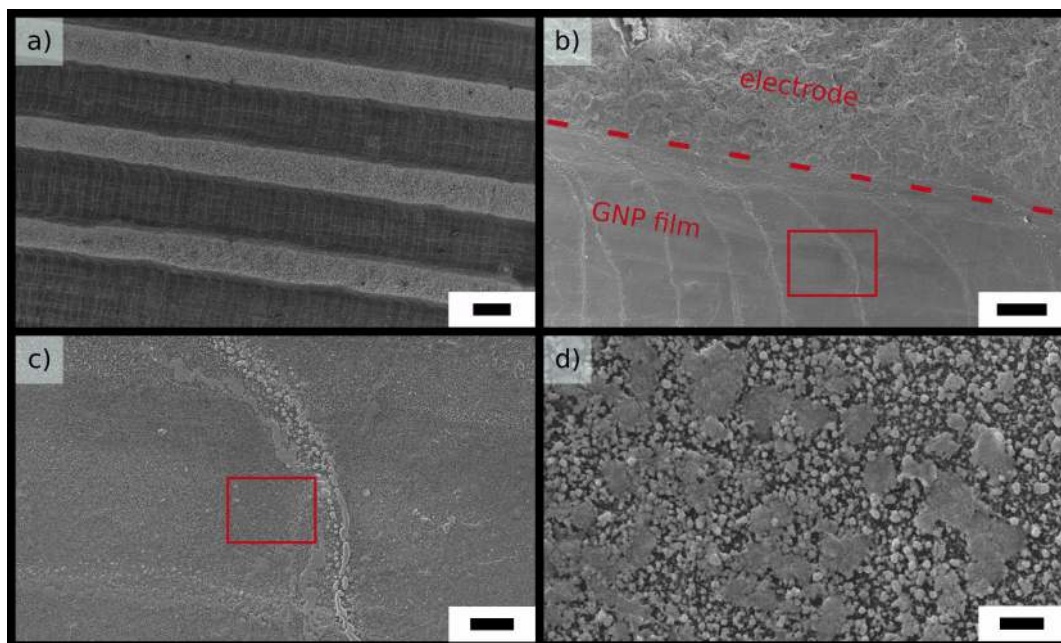


Figure 7.11: SEM images of a GNP film printed onto interdigitated electrodes and cross-linked with 9DT. The film was prepared similar to the sample shown in figure 7.9. *a)* Micrograph depicting the GNP film and the electrode fingers at low magnification. *b)* Higher magnification image of the border line between film and electrode. *c)* Zoom of the area marked in figure part *b)*. *d)* High magnification image of the area indicated by the red box in figure part *c)*. Scale bars: *a)* 200 μm , *b)* 20 μm , *c)* 4 μm , *d)* 400 nm. Adapted with permission from Ref. [81]. The material was modified compared to the original figure shown in the publication.

To initially test the sensing responses of the pure 9DT cross-linked GNP sensor, a sample was dosed with toluene vapors at concentrations of 25 – 2000 ppm. The concentrations were generated using a programmable gas calibration system with nitrogen as carrier gas. Such responses to exposure periods of 240 s are depicted in figure 7.12 a). It can be seen, that the sensor exhibits very short response and recovery times, resulting in almost ideal rectangular response profiles. At a test cell volume of ~ 10 mL and a flow rate of 400 mL min^{-1} , the time required to fully exchange the zero gas (nitrogen) with the analyte vapor is ~ 8 s. As the t_{90} times of the transients are in the same time scale, one can conclude that the actual t_{90} times of the sensors were ≤ 8 s. A response isotherm is depicted in figure 7.12 b) by plotting the response amplitudes vs. vapor concentrations.

Here, mean values of three measurements with different devices are shown and small error bars indicate good reproducibility of the sensor probes. A first-order Langmuir isotherm could be fitted well to the data according to equation 7.4:

$$\frac{\Delta R}{R_0} = \left(\frac{\Delta R}{R_0} \right)^{\text{sat}} \frac{K_b[A]}{1 + K_b[A]} \quad (7.4)$$

with $\left(\frac{\Delta R}{R_0} \right)^{\text{sat}}$ being the relative change of resistance at saturation of the sensor, $[A]$ being the concentration of the analyte vapor and K_b being the Langmuir binding constant. The extracted parameters for $\left(\frac{\Delta R}{R_0} \right)^{\text{sat}}$ and K_b are 6 % and $\sim 10^4$ L mol⁻¹, respectively. The binding constant is similar to results reported in our groups' earlier work for 9DT-based chemiresistors fabricated via LbL self assembly on PE substrates.^[63] It is noteworthy though, that this value is three times higher than that reported for similar GNP films deposited on glass substrates.^[197] The maximum sensitivity corresponds to 2×10^{-5} ppm⁻¹, which is given by the initial slope of the response isotherm and is similar to values reported earlier.^[63]

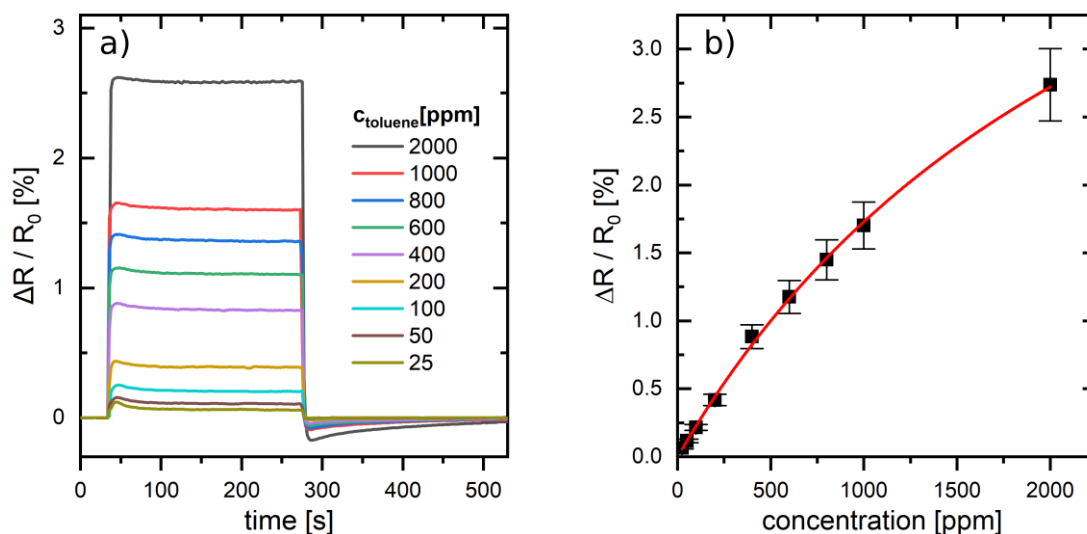


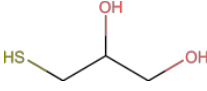
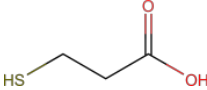
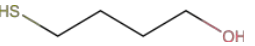
Figure 7.12: a) Baseline-corrected response transients of a chemiresistor made of GNPs cross-linked with 9DT on PI foil. Toluene vapor was used as test gas. b) Response isotherm of a 9DT cross-linked chemiresistor exposed to toluene vapor. The values were obtained by plotting the transient amplitudes vs. analyte concentration. The red line indicates a first-order Langmuir sorption model fitted to the data (cf. equation 7.4). Data points represent mean values of three measurements with different devices and deviations are shown as error bars. Reprinted with permission from Ref[81].

To validate the mechanical robustness of the printed sensor devices, a 9DT cross-linked sensor device was repeatedly flexed at radii of curvature down to 5 mm. The baseline resistance as well as the response patterns to toluene remained nearly unchanged, indi-

cating no significant changes in the sensor’s morphology. Further, optical micrographs proved that neither the GNP transducer nor the electrodes degraded or delaminated from the PI foil. Details are provided in the appendix chapter A.5.

After the printing protocol was established for chemiresistor fabrication, their chemical sensitivity was tuned. To this end, monothiols (ligands, L) with polar functional groups were added to the 9DT cross-linking ink at different molar ratios. An overview of all blends containing the respective monothiol (L), its concentration and the abbreviation used for the fabricated sensors is given in table 7.2.

Table 7.2: List of thiols (abbreviations), structural formulas of 9DT and monothiols L as well as relative molar concentrations of the ligand L in 9DT+L blends used in this study. Furthermore, the abbreviations of sensors used in this study are given.

thiols (abbreviations)	structural formula	rel. conc. of L [%]	sensor
1,9-nonanedithiol (9DT)		0	S-9DT
1-thioglycerol (TG)		25	S-TG.25
		50	S-TG.50
3-mercaptopropionic acid (3MPA)		25	S-3MPA.25
		50	S-3MPA.50
4-mercapto-1-butanol (4M1OH)		25	S-4M1OH.25
		50	S-4M1OH.50

The printing protocol for such sensors was the same as for the 9DT cross-linked sensor, except that the 9DT+L mixtures were used for fabrication. The used monothiols (L) bind to the GNP surface via their thiol head-group and add hydroxyl or carboxyl groups to the unpolar 9DT matrix surrounding the GNPs. Their introduction should consequently increase the sensors’ sensitivities to polar analyte vapors.

IV-curves of all used sensors can be seen in figure 7.10 b) demonstrating that all samples exhibit ohmic conductivity. However, sensors made with mixtures of 9DT and monothiols show higher resistances compared to the sensor made with pure 9DT. These findings are in agreement with a study presented by Cui et al. stating that replacing cross-linkers to some extent with alkylthiols leads to a less interconnected GNP network, hence, to a material with reduced conductivity.^[111] These findings are further supported by the fact, that sensors containing the highest amount of monothiol (50 vol%) exhibited the highest resistances as can be seen in the inset of figure 7.10 b). However, it should be noted that different trends were observed, exhibiting an increase in conductivity by replacing a

dithiol cross-linker with a monothiol such as, e.g., TG.^[136]

Seven sensors with different ink formulations (cf. table 7.2) were combined to form an array and read out via a custom-made multiplexer setup (details in the appendix chapter A.6). Their chemical sensitivity was characterized using volatile analytes with hydrophilic (ethanol, water), amphiphilic (1-butanol, 1-propanol) and hydrophobic (n-octane, toluene, 4M2P) character. Baseline-corrected response transients for these analytes at concentrations of 2000 ppm are depicted in figure 7.13 a). As the pure 9DT sensor, sensors fabricated with the mixed ink formulations also showed remarkably fast and fully reversible responses. The sensitivities of all sensors to the different analytes presented in figure 7.13 b) were determined from the initial slopes of the response isotherms. Graphs of all response isotherms are depicted in the appendix figure A.6. Although the response isotherms show non-linear characteristics, the response transients presented in figure 7.13 a) basically show similar trends compared to the sensitivities shown in figure 7.13 b).

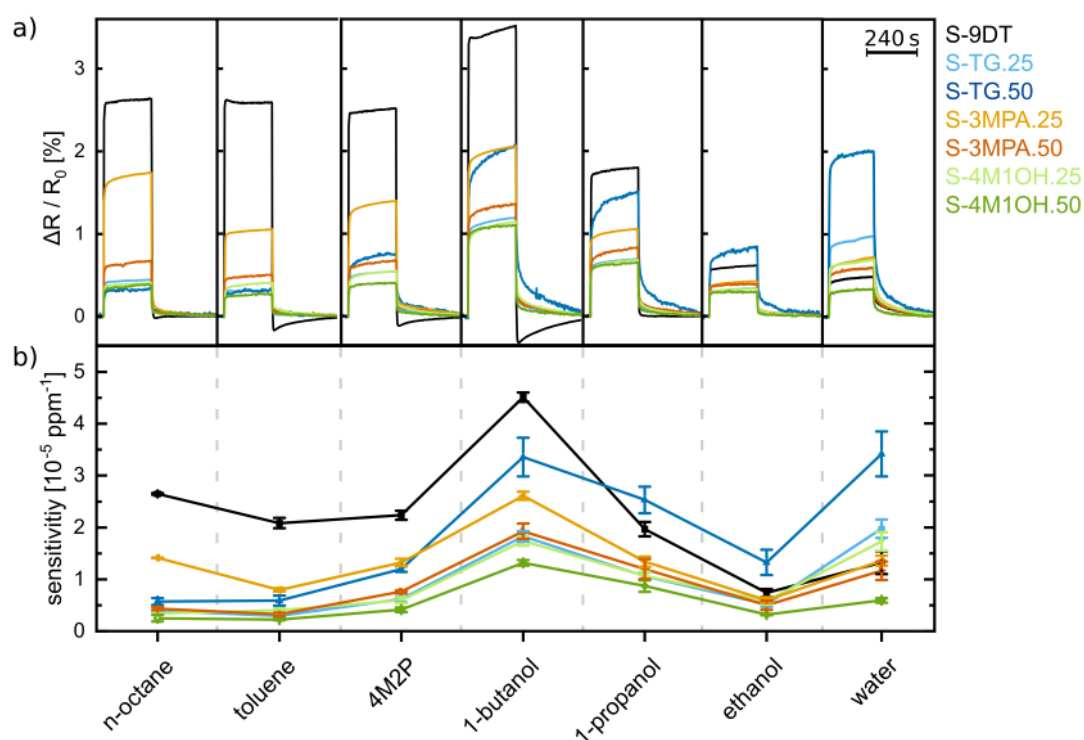


Figure 7.13: a) Baseline-corrected response transients of GNP-based chemiresistors fabricated with different 9DT+L blends. The sensors were dosed with vapors of hydrophobic (n-octane, toluene, 4M2P), amphiphilic (1-butanol, 1-propanol) and hydrophilic (ethanol, water) analytes at concentrations of 2000 ppm. Scale bar: timescale for all traces shown. b) Sensitivities of the sensors to different analytes. The sensitivities were determined from the initial slopes of the response isotherms shown in the appendix figure A.6. The error bars represent the deviations of the slopes to the fitted data. Reprinted with permission from Ref. [81].

As described in chapter 5.2.4, the sensitivity of a GNP-based chemiresistor to different analyte gases depends on various effects. Swelling of the film on the one hand causes an increase in resistance, since the interparticle distance is increased.^[74] On the other hand, sorption of analytes with high permittivity can decrease the charging energy of the GNPs, thus, leading to a decrease of the transducer's resistance.^[128] However, commonly a GNP-based chemiresistor's response upon analyte exposure is an increase in resistance, indicating that for these types of films swelling is the predominant effect of the sensing mechanism. Moreover, the sensitivity of such a chemiresistor to different analytes critically depends on the partition coefficient of the respective analyte. It is generally accepted, that partition coefficients are high for analytes matching the solubility properties of the ligand/linker matrix of the GNP transducer. Here for example, if GNPs are embedded in a non-polar hydrophobic matrix the partition coefficients of non-polar hydrophobic analytes are significantly higher compared to polar hydrophilic analytes.^[129]

The vapor pressure of the respective analyte also plays an important role. Considering an analyte with a low vapor pressure, it tends to have a higher partition coefficient, most probably resulting in an increased sensitivity response of the chemiresistor. Also the molecular dimension of the analyte may affect the efficiency of the swelling, since larger molecules could more effectively cause swelling of the GNP film.^[74]

Based on the above mentioned aspects, a quantitative analysis of the sensitivity to different analytes is highly complex and beyond the scope of this work. However, a qualitative analysis for the most pronounced trends will be given in the following. First, as can be seen from figure 7.13 a), all sensors responded to the applied vapors with an increase in resistance. This behavior suggests, that sorption-induced swelling was the dominating effect for each chemiresistor/analyte pair, which is in agreement with previous studies.^[74,129]

Furthermore, the sensors showed relatively high sensitivity towards 1-butanol, which has an amphiphilic character and intermediate polarity. This result seems remarkable especially for sensor S-9DT (pure 9DT matrix) containing a pure hydrophobic alkylene backbone. However, it is known from Schlicke et al. that 9DT cross-linked GNP films contain various unbound thiol groups.^[30] These free thiol groups can interact with protic (1-butanol, 1-propanol, ethanol) and aprotic (4M2P) polar compounds and form hydrogen bonds. Moreover, it can not be excluded, that the fabricated GNP film still contained some residual amphiphilic 12A, which was the initial stabilizer of the GNPs in solution. Since all sensors contained 9DT as cross-linker (and possibly residual 12A), it is reasonable why all sensors exhibited a relatively high sensitivity towards 1-butanol. An additional aspect to explain the high sensitivities towards 1-butanol is its low vapor pressure, which may allow for a better sorption to the GNP films as shown in our groups previous study.^[84]

The comparison of sensors printed with pure 9DT and 9DT+L blends shows that the sensor containing the 9DT+L matrix exhibited lower sensitivities towards hydrophobic analytes, such as 4M2P, toluene, and n-octane. This trend can, for example, be seen clearly for the sensors S-3MPA.25 and S-3MPA.50 printed using the 9DT/3MPA ink. Here, the increased amount of 3MPA for sensor S-3MPA.50 led to a further decreased sensitivity towards hydrophobic analytes compared to sensor S-3MPA.25. Accordingly, it was concluded that increasing the amount of monothiol increased the hydrophilic character of the GNP films. For example sensor S-TG.50 (9DT/TG, 1:1) shows greater responses to 1-propanol and ethanol than sensor S-9DT.

The data shown in figure 7.13 b) also demonstrate, that the sensitivities of all sensors to alcohols decrease in the order 1-butanol > 1-propanol > ethanol. This trend is generally attributed to the differences in vapor pressure (1-butanol: 8.85 hPa; 1-propanol: 28.2 hPa; ethanol: 78.7 hPa)^[198,199] leading to a decreased solubility in the ligand/linker matrix with increasing vapor pressure.

Moreover, the decreasing molecular volume, as well as the increasing permittivities (1-butanol: 17.8; 1-propanol: 20.1; ethanol: 25.3)^[198,199] may contribute to the observed results. By further inspecting the results, one finds that the sensitivities towards 1-butanol, 1-propanol, and ethanol of the sensors printed using the 9DT+L increased in this order compared to the sensitivity of the sensor containing pure 9DT. This behavior in general confirms the expected increased sensitivity to hydrophilic analytes of sensors with increased monothiol amount. Even more pronounced are the results for water as analyte. Here, both sensors fabricated with 9DT/TG S-TG.25 and S-TG.50 show significantly increased sensitivities to water. Hence, blending the 9DT ink with TG containing two hydroxyl groups (cf. table 7.2), thus forming more H-bonds, tuned the chemical selectivity most effectively towards polar hydrophilic analytes.

Radar plots of the sensor responses to toluene, 1-propanol and water for concentrations of 2000 ppm and 100 ppm are shown in figure 7.14. The radar plots clearly show that the selectivity of the sensors was successfully tuned by blending additional monothiols with polar functional groups into the 9DT ink. Moreover, although the above discussed response isotherms are non-linear, the radar plots at different concentrations (2000 and 100 ppm) are very similar in shape allowing for the discrimination of analytes at different concentrations. In this context it should be noted, that if the selectivity of the sensor remained unaffected by the blending of the different monothiols and only the sensitivity changed, the radar plots would form distorted heptagons which would have different sizes but the same shape for different analytes. Figure 7.14 a) and b), however, show distinct shapes for three different analytes.

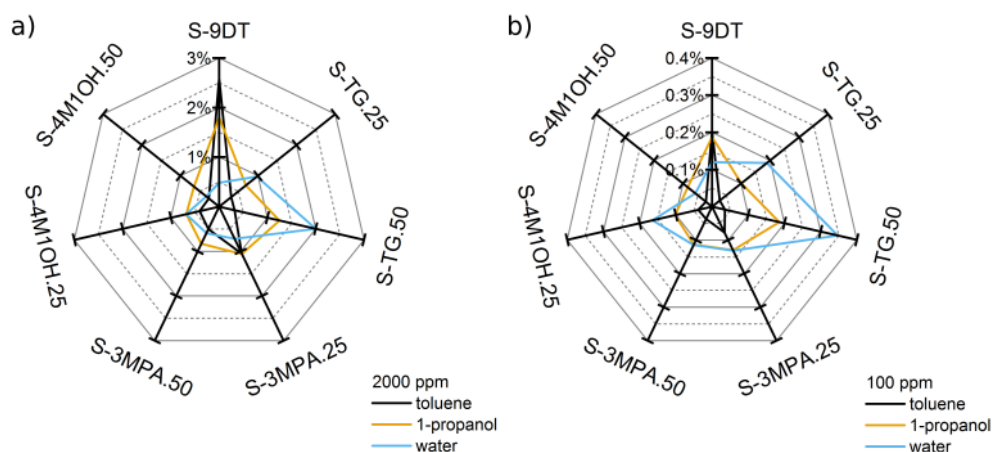


Figure 7.14: Radar plots of sensor response amplitudes. Selected analytes are depicted ranging from hydrophobic to hydrophilic character. The sensors were exposed to analyte vapors at concentrations of a) 2000 ppm and b) 100 ppm. The corresponding response transients for figure part b) are shown in the appendix figure A.7. Reprinted with permission from Ref. [81].

Summary. In this study the fabrication of fully printed flexible chemiresistors based on cross-linked GNPs was presented. First, interdigitated electrodes were printed onto flexible PI foil via dispenser printing. Second, transducers of cross-linked GNPs were deposited onto the electrode structures via inkjet-printing. Here, the cross-linking ink consisted of either 9DT or mixtures of 9DT and functionalized monothiols to tune the selectivity of the chemiresistors. This fabrication method is well-suited for on-demand fabrication of flexible chemiresistor arrays for specific purposes. Further, it should be possible to tune the selectivity of such sensors to be highly suitable for personalized health care monitoring, eg., breath analysis or for diagnostic applications in electronic skin devices. Future work may include the introduction of a greater variety of differently functionalized ligands to further adjust the organic structure of the matrix and alter the selectivity. Additionally, differently shaped GNPs could be included to further alter the nanoscale structure and change the overall electric properties of the transducer material.

7.3 Mechanical Resilience

In view of the potential future applications of GNP-based materials as flexible, wearable sensors, a thorough assessment of their mechanical resilience and durability is of great interest, since the performance of the strain gauges and chemiresistors critically relies on the mechanical properties of the cross-linked GNP films.

These properties were tested by fabricating so called nanomembranes (freestanding GNP

films) via LbL spin-coating followed by floating and transferring them onto holey substrates. The nanomembranes were subsequently bulged as described in chapter 6.6. Different parameters such as critical stresses and strains (stress/strain at which the nanomembranes collapse) as well as elastic moduli of the nanomaterial were extracted from experiments conducted with nanomembranes comprising differently cross-linked GNPs. Furthermore, the nanomembranes' toughnesses were calculated to obtain the energy stored in them until the applied underpressure resulted in a rupture of the membrane. The graph in figure part 7.17 a) depicts stress/strain curves closest to the critical parameters shown in figure part 7.17 b). Stress/strain curves of all characterized nanomembranes are shown in the appendix in figure A.8 and A.9.

The experiments were conducted with particles of ~ 4 nm and ~ 7 nm in diameter fabricated according to Leff et al. and Peng et al., respectively.^[59,61] Figure 7.15 provides size histograms, as well as UV/vis spectra and representative TEM images of the particles used for these experiments. Particles from both systems were interconnected with a variety of dithiols (1,4-butanedithiol (4DT), 1,6-hexanedithiol (6DT), 1,9-nonanedithiol (9DT), 1,4-benzenedithiol (BDT)) to investigate the cross-linker's influence on the mechanical parameters mentioned above. Structural formulas of the linkers are provided in figure 7.15 f). Since the position of the GNPs' surface plasmon resonance (SPR) (cf. figure 7.15 b) provides valuable information about the films' interparticle distance and microstructure, additional UV/Vis spectra of the cross-linked films are provided in figure part 7.15 e). These results show that the average distance of the GNPs can be controlled by varying the dithiol cross-linker. Note, the UV/vis spectra were obtained from glass substrate supported GNP films before they were transferred onto the holey substrates used for bulge experiments and all spectra were normalized for a better comparison of the shift of the plasmon peaks.

7. Results and Discussion

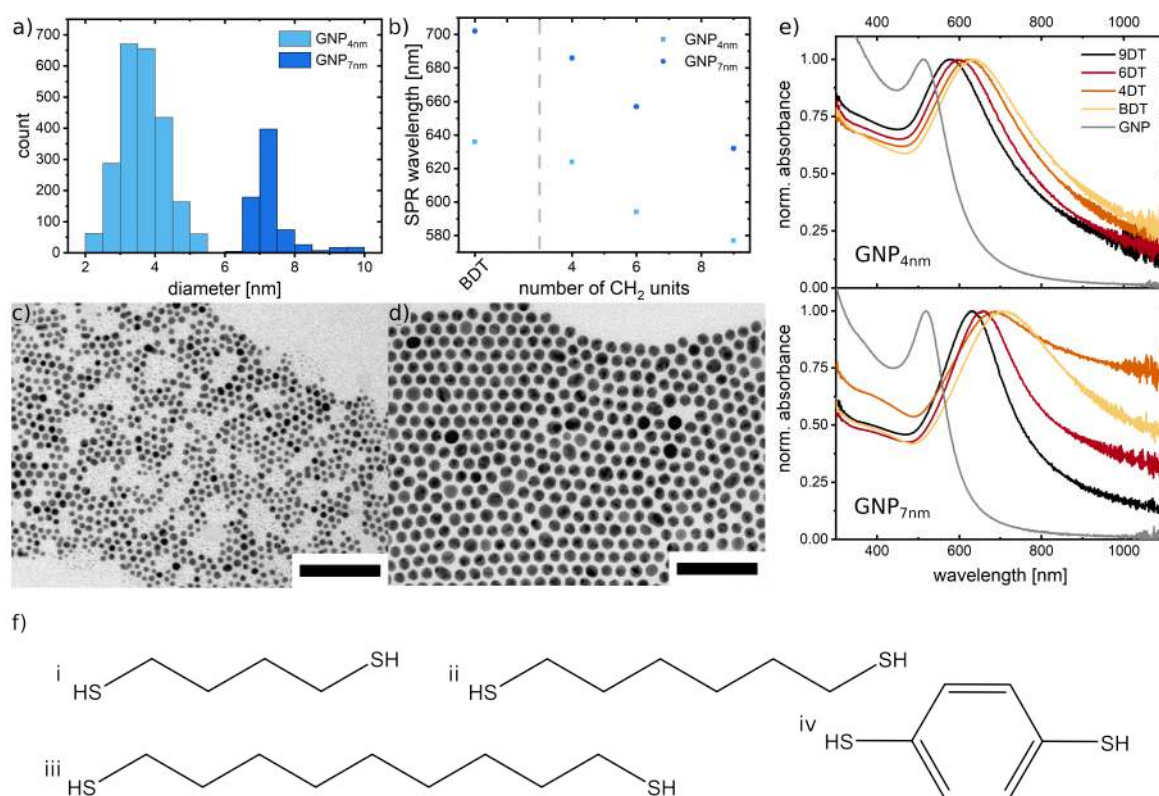


Figure 7.15: *a)* Size histograms of the particles used for nanomembrane fabrication. *b)* SPR peaks of the GNP films as a function of the number of CH₂ units of the respective cross-linkers. The BDT cross-linker was separately added to the plot. *c)* Representative TEM image of the ligand stabilized GNP_{4 nm} particles. *d)* Representative TEM image of the ligand stabilized GNP_{7 nm} particles. *e)* Normalized UV/vis spectra of all cross-linked films used for bulge experiments compared to the respective stock solution (grey line). The red-shift with decreasing linker length due to enhanced coupling of the plasmons is clearly visible. *f)* Structural formulas of all dithiol linkers used. i: 4DT, ii: 6DT, iii: 9DT, iv: BDT. Scale bars: *c)*, *d)* 50 nm.

To conduct bulge experiments, the GNP films were transferred onto holey silicon substrates with an aperture diameter of ~ 80 nm to provide freely suspended nanomembranes. They were bulged in a setup presented in one of our groups earlier works^[31] and by stepwise increasing underpressures ranging from 100 Pa up to ~ 70 kPa until the membranes collapsed. At each bulging state an atomic force microscope (AFM) scan was performed to obtain height profiles of the nanomembrane. All measurements were performed within ~ 60 min. The nanomembranes were bulged with pressure rates of up to ~ 60 and ~ 10 Pa s⁻¹ for the GNP_{4nm} and GNP_{7nm}, respectively. According to the model presented in chapter 5.2.5 the biaxial stress acting laterally in the membrane was calculated using the applied underpressure, the thickness of the membrane and the radius of curvature. The latter was obtained by fitting spheres to the height profiles of the nanomembrane at each applied underpressure. The respective biaxial strains were calculated using the nanomem-

branes' arc lengths at zero and at different applied underpressures. Thicknesses of the nanomembranes were determined via AFM and were in the range $\sim 20\text{--}35$ nm. Exemplary topographic scans of each particle system are depicted in figure 7.16. It should be noted, that these topographic scans were performed at the edges of the holey silicone substrates to obtain the exact topography of the nanomembranes used for bulging.

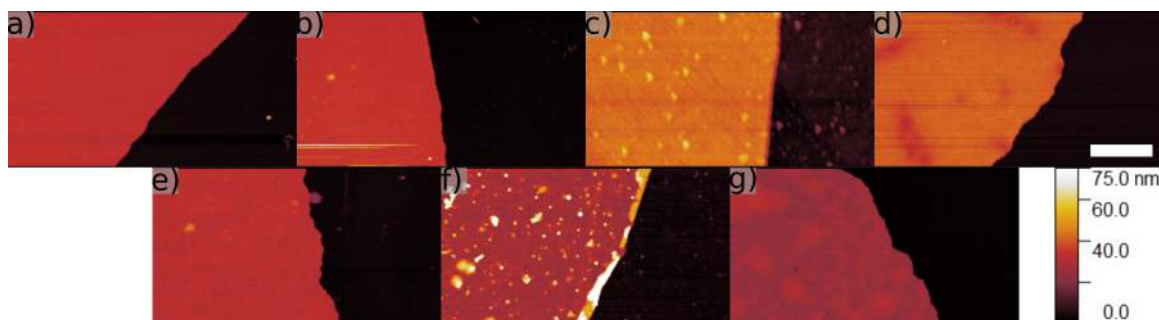


Figure 7.16: Representative topographic AFM scans of nanomembranes used for bulge experiments. a) GNP_{4nm}-4DT, b) GNP_{4nm}-6DT, c) GNP_{4nm}-9DT, d) GNP_{4nm}-BDT, e) GNP_{7nm}-6DT, f) GNP_{7nm}-9DT, g) GNP_{7nm}-BDT. Scale bar: 2 μm .

For each experiment the last measured height profile before the nanomembrane ruptured was taken to calculate the critical stress and strain. Biaxial moduli were obtained by fitting the linear regime of the stress vs. strain curve. From the biaxial moduli Young's moduli were extracted using Poisson ratios for the GNP nanomembranes of 0.33, as they are commonly found in literature.^[148,189,190]

Mean values were calculated from at least three different samples. Toughnesses were obtained by integrating polynomial fits of the stress/strain curves ranging from strains at 600 Pa up to the critical strains. It has to be noted, that no bulge experiments were performed with GNP_{7nm}/4DT, since the membrane immediately ruptured after mounting the sample on the substrate holder. Table 7.3 shows the Young's modulus, the core diameter of particles used for nanomembrane fabrication as well as the nanomembranes' critical parameters and toughness and employed cross-linkers. For GNP_{4nm} and GNP_{7nm} Young's moduli between 2.4–5.7 GPa and 2.3–9.3 GPa were obtained, respectively, depending on the cross-linker used. These results are in good agreement with values found in literature. Schlicke et al. obtained Young's moduli of ~ 3.6 GPa for 9DT cross-linked GNPs with a core diameter of ~ 7 nm^[72] and Young's moduli of $\sim 3.6\text{--}10$ GPa for GNPs with a core diameter of ~ 4 nm depending on the cross-linking agent.^[30] Wang et al. determined a Young's modulus of 2 GPa for 12T stabilized particles with a mean core diameter of ~ 5 nm.^[146] These studies confirm that the elastic moduli of GNP nanomembranes are in the low GPa regime. As can be seen from table 7.3 the Young's modulus is increasing with

decreasing linker length, which is in good agreement with literature.^[30] Since the Young's modulus is a measure for a material's stiffness it is expected, that with decreasing linker length the nanomembrane becomes stiffer. Both types of nanomembranes (GNP_{4nm} and GNP_{7nm}) exhibit the lowest critical strain, when BDT is used as cross-linker, since this molecule offers least flexibility (cf. figure 7.15 f). As can be seen in the table below, the Young's moduli of nanomembranes made from GNP_{4nm} cross-linked with BDT, 4DT and 6DT are similar which is probably related to a similar size of the cross-linking agents. By comparing the Young's moduli of composites made from both the GNP_{4nm} and GNP_{7nm}, composites made from smaller particles tend to have higher Young's moduli for the same alkane organic cross-linker. This is probably due to the increased interconnection of smaller particles compared to larger ones. Hence, higher forces are needed to yield a similar strain of a nanomembrane comprising smaller particles compared to a nanomembrane made from larger ones. For BDT nanomembranes made from both particle systems exhibit the highest Young's modulus compared to nanomembranes made with ADT linkers because of the rigid molecule structure.

Table 7.3: Young's moduli, critical strains and stresses and toughnesses for both particle systems interconnected with different cross-linkers.

GNP size [nm]	cross-linker	Young's modulus [GPa]	critical strain [%]	critical stress [MPa]	toughness [MJ m ⁻³]
4	4DT	4.9 ± 0.7	1.8 ± 0.1	109 ± 11	1.1 ± 0.1
	6DT	4.4 ± 0.2	2.4 ± 0.5	112 ± 15	1.7 ± 0.6
	9DT	2.8 ± 0.3	2.4 ± 0.4	82 ± 10	1.1 ± 0.3
	BDT	4.9 ± 0.3	1.0 ± 0.25	65 ± 10	0.3 ± 0.1
7	6DT	3.9 ± 0.3	1.1 ± 0.2	53 ± 6.4	0.3 ± 0.1
	9DT	2.5 ± 0.4	1.3 ± 0.5	40 ± 14	0.3 ± 0.2
	BDT	7.9 ± 1.0	0.33 ± 0.07	38 ± 5.9	0.07 ± 0.02

The overall comparison between the toughnesses of nanomembranes made from GNP_{4nm} and GNP_{7nm} particles shows that generally more energy can be stored in nanomembranes made from smaller particles.

Figure 7.17 b) depicts critical stresses and strains for nanomembranes made of both particle systems. The overall tendency clearly shows that GNP_{4nm}-based nanomembranes could be strained to a higher extend until rupture (~2.5 % strain for GNP_{4nm}/9DT) than nanomembranes made from GNP_{7nm} with the same cross-linker (~1.3 % strain for GNP_{7nm}/9DT). The critical stresses for these two particle systems (GNP_{4nm}/9DT and GNP_{7nm}/9DT) were in the range of ~110 MPa and ~40 MPa, respectively. Since the applied strain is primarily transferred to the organic molecules in the interparticle positions, fewer interparticle positions have to compensate the same strain for nanomembranes made

from larger GNPs. This effect leads to smaller critical stresses and strains for nanomembranes made from larger particles, hence to smaller toughnesses as elucidated in figure 7.17.

Additionally, as can be seen from figure 7.16 the nanomembranes made from $\text{GNP}_{7\text{nm}}$ are less homogeneous than the ones made from $\text{GNP}_{4\text{nm}}$ particles. These local inhomogeneities of GNPs might also lead to punctually higher stresses during the bulge experiments, which causes the nanomembranes of larger GNPs to collapse earlier.

Figure 7.17 further indicates the general decrease of the critical strain for each particle system when the length of the alkane cross-linker is reduced. This behavior is expected, since smaller alkane linkers can be strained less, which leads to a faster collapse of the nanomembrane. Jaeger and coworkers found comparable critical parameters for GNP (core size ~ 5 nm) monolayers stabilized with 12T in the range of 0.9 % strain and ~ 11 MPa.^[146] Tsukruk and coworkers found critical parameters for GNP (core size ~ 13 nm) nanomembranes sandwiched between polyelectrolyte multilayers of 0.8–2 % strain and stresses of ~ 75 MPa at similar Young's moduli of 5–10 GPa.^[143] Both works are depicted in figure 7.17 b) as reference.

This figure part also emphasizes the rigidity of the nanomembranes made from BDT-cross-linked particles, exhibiting the lowest critical parameters with stresses of ~ 40 MPa and ~ 0.3 % and ~ 65 MPa at strains of ~ 0.3 % and ~ 1 % for nanomembranes comprising $\text{GNP}_{7\text{nm}}$ and $\text{GNP}_{4\text{nm}}$, respectively. The relatively large deviations especially for 9DT cross-linked nanomembranes can possibly be attributed to fluctuations during membrane transfer via skimming and defects.

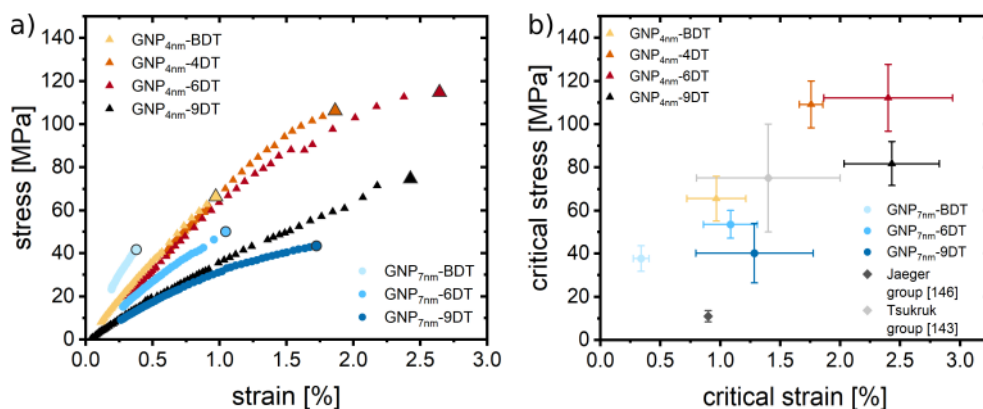


Figure 7.17: a) Stress/strain curves of samples closest to the mean values of the critical parameters depicted in figure part b). The highlighted values of each measurement curve were recorded just before membrane collapse. b) Critical stresses and strains for particle systems comprising $\text{GNP}_{4\text{nm}}$ and $\text{GNP}_{7\text{nm}}$ with different cross-linkers.

Summary. Mechanical properties of GNP nanomembranes were determined via bulge experiments. Different particle systems were employed comprising GNPs with different core diameters and a variety of alkane cross-linkers and 1,4-benzenedithiol (BDT). Critical mechanical parameters such as stresses and strains of the nanomembranes measured before rupture showed that the smaller GNP_{4nm}-based nanomembranes can be strained to a higher extend compared to their GNP_{7nm} counterparts. For both particle systems these critical parameters decrease when the length of the alkane cross-linker is decreased as well. GNPs cross-linked with BDT exhibit the lowest critical stresses and strains due to the rigid nature of the linker molecule.

7.4 Durability

Since the long-term stability is highly important for the applications of cross-linked GNP networks, as it was addressed in one of our groups former studies,^[62] in this section the accelerated aging behavior of such composites will be discussed.

To this end, the particles were artificially aged in a climate chamber (WKL 34/40, Weiss Umwelttechnik GmbH) at mild (65 °C, 65 %rH) and harsh (85 °C, 85 %rH) temperature and humidity conditions which are in the following referred to as 65/65 and 85/85 tests. Climate chamber parameters were validated once at 85/85 conditions using an external humidity and temperature sensor (BME680, Bosch) and are depicted in the appendix, figure A.10 a). Especially the 85/85 test conditions are commonly chosen to perform stress tests for electronic components in industry.^[200] The period for this type of test is commonly 1000 hours (~42 days). However, in this study 9DT cross-linked GNPs with different core diameters (~4 nm and ~8 nm) were aged for a total period of 28 days (~670 hours) and a variety of imaging and measurement techniques were applied to track the aging process of these systems. It should be noted, that for the LbL spin-coating preparation of the GNP films in this project the same concentration (7.4 mM) for the 9DT cross-linker was used. This might lead to a decreased linker to particle ratio for the smaller (~4 nm) particles compared to the GNPs with a core diameter of ~7 nm. By applying the Q₁₀ rule (cf. chapter 5.2.6) to roughly approximate the 28 days of degradation for the 65/65 and 85/85 tests, virtual tests periods of ~1 year and ~5 years were determined, respectively. For all films, initial (day 0) non-electrical measurements were performed directly after the GNP film was removed from the over-night immersion in the 9DT/methanol bath (cf. chapter 6.2.1). The initial electrical measurement was performed directly after electrode structures were deposited onto the film. However, due to the PVD deposition process of

the electrodes, the initial electrical measurement was performed ~ 16 h after the films were removed from the 9DT/methanol bath.

Figure 7.18 provides basic information, such as size histograms, UV/vis absorbance spectra and representative TEM images, about the two particle systems used, which have a mean core diameter of ~ 3 – 4 nm and ~ 7 nm, respectively, and are in the following referred to as GNP_S (comprised of two synthesis, $\text{GNP}_{3\text{nm}}$ and $\text{GNP}_{4\text{nm}}$) and GNP_L (comprised of $\text{GNP}_{7\text{nm}}$). The GNP films had thicknesses ranging from 20 to 45 nm.

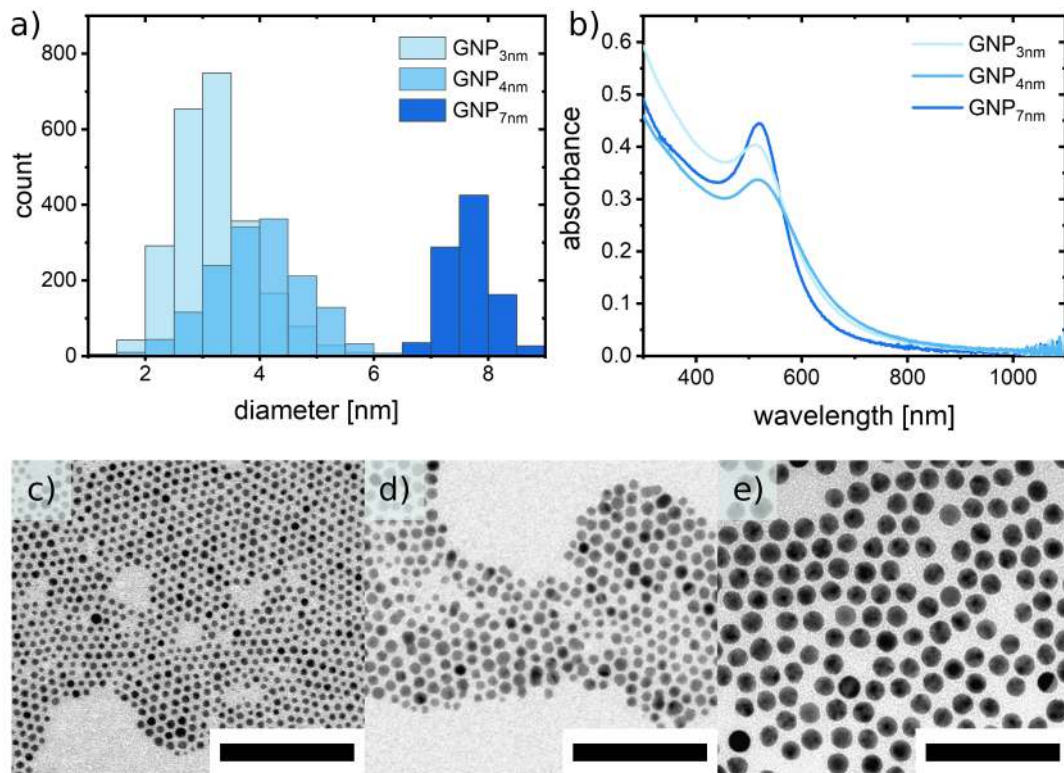


Figure 7.18: a) Size histograms of both particle systems used. b) UV/vis absorbance spectra of both synthesis used for GNP film preparation. The dilution factor f was $1/300$ for all synthesis and the optical path length was 10 mm. c) , d) , e) Representative TEM images of $\text{GNP}_{3\text{nm}}$, $\text{GNP}_{4\text{nm}}$ and $\text{GNP}_{7\text{nm}}$, respectively. Scale bars: 50 nm.

Since nearly all applications involve applying a bias to the composites, first IV-curves were recorded after each day of the first week of aging and after 14 and 28 days, respectively. To this end, a bias sweep from -5 – 5 V was applied and the resulting current was measured. Figure 7.19 depicts specific conductivities σ of artificially aged GNP films on glass compared to a sample which was stored in a nitrogen atmosphere at room temperature and another sample stored under ambient conditions. The specific conductivities were calculated according to equation 7.5.

$$\sigma = \frac{Gd}{bt} \tag{7.5}$$

Here, G is the sample's conductance, d is the distance between the electrodes, b is the width of the electrodes and t is the thickness of the GNP film.

The comparison of both 9DT cross-linked particle systems shows, that the larger GNP_L particles exhibit higher overall specific conductivities, as expected (cf. equation 5.7). All initially (day 0) measured specific conductivities are in good agreement with values presented in literature.^[62,83,100] The graphs further show, that the increase in conductivity during the artificial aging is most pronounced for the 85/85 tests, especially in the last 14 days for both particles systems. Here the conductivity of the GNP_S and GNP_L system increased by a factor of 1.4 and 2, respectively, compared to the initial measurement. The sample stored under ambient conditions also showed an increase for the GNP_L system similar to what was observed for the sample stored under 65/65 conditions, whereas the GNP_S ambient sample remained nearly constant. The samples stored under nitrogen did not show any changes in conductivity over the measurement period of 28 days. Similar trends were found by Joseph et al. for GNPs cross-linked with alkane dithiols^[161] and by Panjwani et al. for gold-black.^[201]

Furthermore, the GNP_L system showed a somewhat exponential increase in conductivity when stored under 65/65 or 85/85 conditions. The GNP_S sample, however, exhibited a strong increase in conductivity after the first day and between day 14 and day 28. Between day 1 and day 7 this sample only showed little change. The GNP_S sample stored under ambient conditions did not show any significant change in conductivity during the whole aging period. The stability of the GNP_S system's ambient sample and the less pronounced increase in conductivity during the 85/85 test period indicate that the smaller particles are cross-linked more effectively than the larger particles from the GNP_L system. These measurements also show, that the kinetics of the aging behavior for both particle systems is different.

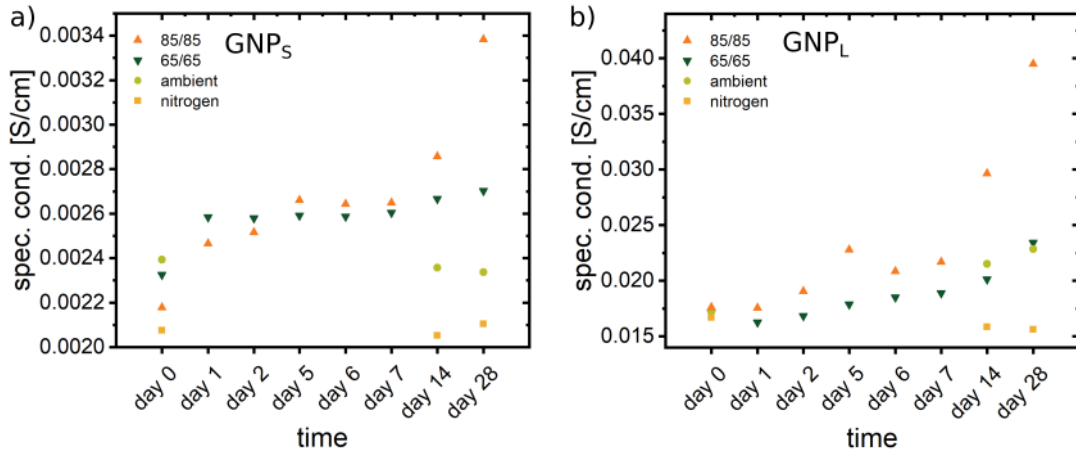


Figure 7.19: Specific conductivities of artificially aged GNPs cross-linked with 9DT compared to a sample stored under ambient conditions and in a nitrogen atmosphere. a) GNP_S. b) GNP_L.

Additionally, the GNPs' sensitivity to strain under the influence of artificial aging was investigated. For this purpose, GNP films on PI foil were glued onto stripes of FR4 material and deflected up to strains of $\sim 0.12\%$ using a custom-built flexural bending setup. Figure 7.20 shows the general increase of the sensitivity to strain for both particle systems during artificial aging. Here, the same trends as for the conductivity measurements were observed, namely, the larger effect of humidity and temperature to the larger particles (GNP_L). The sensitivity of the GNP_L system increased by a factor of up to 3, whereas for the GNP_S system the sensitivity only increased by a factor of 2, which as well indicates, that the films fabricated using the smaller particles are more stable under the artificial aging conditions. It is also astonishing that the GNP_L sample nearly reached its maximum sensitivity after two days of aging under 65/65 conditions, while the increase in sensitivity was more gradually for the GNP_L sample stored under 85/85 conditions. Moreover, no additional increase of the sensitivities was observed when the particles were aged under 85/85 conditions compared to the 65/65 test showing that the aging process of such nanoparticle systems is highly complex. As the IV-measurements showed, no significant changes of the conductivity were observed for the samples stored in a nitrogen atmosphere, hence no strain response measurements were performed with samples solely stored under nitrogen conditions.

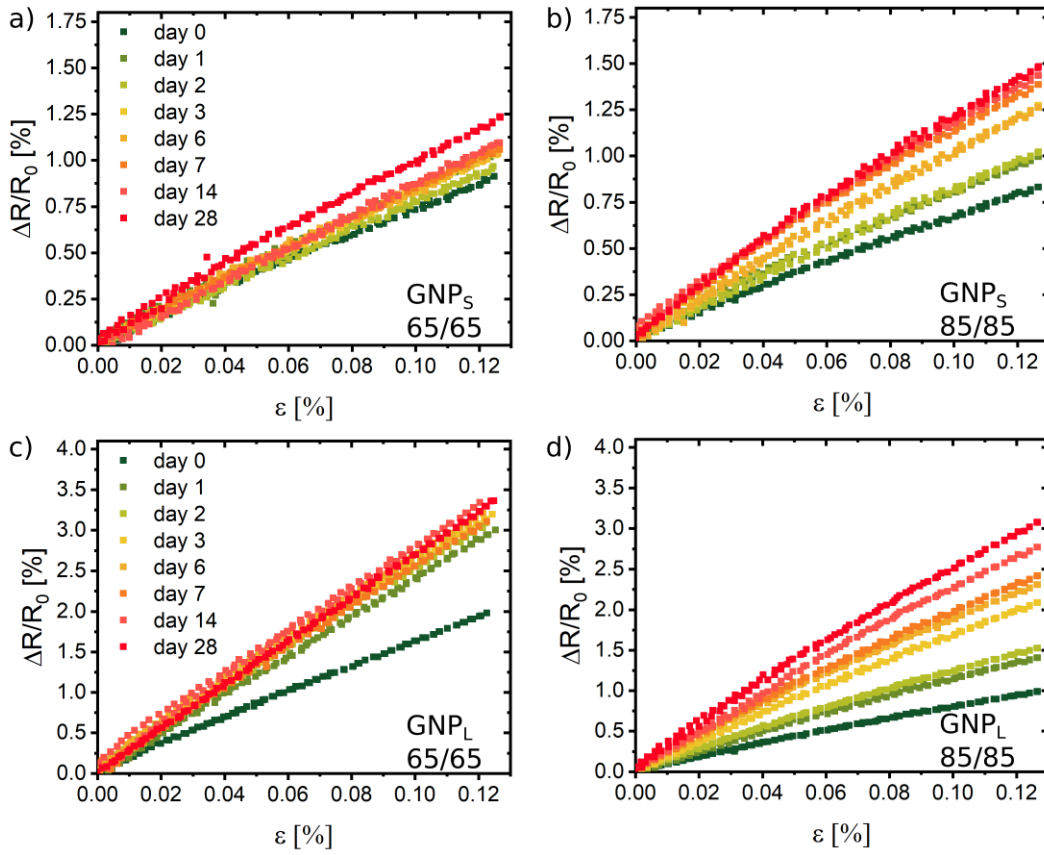


Figure 7.20: Resistive strain response curves for artificially aged GNP_S and GNP_L systems. a) GNP_S stored under 65/65 conditions. b) GNP_S stored under 85/85 conditions. c) GNP_L stored under 65/65 conditions. d) GNP_L stored under 85/85 conditions.

Since changes of the electrical properties of the GNP films are expected to be related to changes in the composites morphology, TEM images of both particles systems were recorded at day 0 and day 28. For this purpose, thin films were skimmed onto TEM copper grids provided with a carbon film and for each measurement a new sample was taken. The images are depicted in figure 7.21 and show nearly no change in the GNP film's morphology of the GNP_S -based system after aging for 28 days under 65/65 conditions. Under 85/85 conditions this particle system exhibited a slight increase in the domain size after aging for 28 days. This heat-induced coarsening of GNP networks is also described in literature. Yu et al. described structure transitions of GNP crystals under the influence of temperature.^[202] Gubicza et al. also found agglomeration of cetyltrimethylammonium bromide (CTAB) stabilized GNPs in water after a period of one year. Here, both Ostwald ripening and particle agglomeration were observed, which was related to the removal of surface stabilizing ligands.^[203] It should be noted that for GNP_S -based systems different stock solutions were used for the 65/65 and 85/85 tests, resulting in slightly different particle sizes for the day 0 TEM images (cf. figure 7.18 a).

For the GNP_L -based system the influence of the artificial aging was more pronounced. Here, figure 7.21 clearly shows, that the GNPs formed even larger agglomerates after the 85/85 test compared to the 65/65 test. The changes of the GNPs shown in the TEM images are in agreement with the results obtained from the 65/65 and 85/85 electrical measurements shown in figure 7.19, where the GNP_L -based particle system showed generally larger changes compared to the GNP_S -based particle system. Furthermore, differences between both test periods (65/65 and 85/85) are clearly visible for the GNP_L -based particle system. The strong correlation between the reduction in resistance and the increase of feature sizes was also reported for thermally evaporated porous gold films by Panjwani et al.^[201] It has to be noted, that all samples for the TEM imaging were first transferred to the copper grids before aging, since it was uncertain that after an advanced test period still a transfer from initial glass substrate to TEM copper grids could be ensured. Different substrates, however, might also affect the aging behavior of the GNP films.

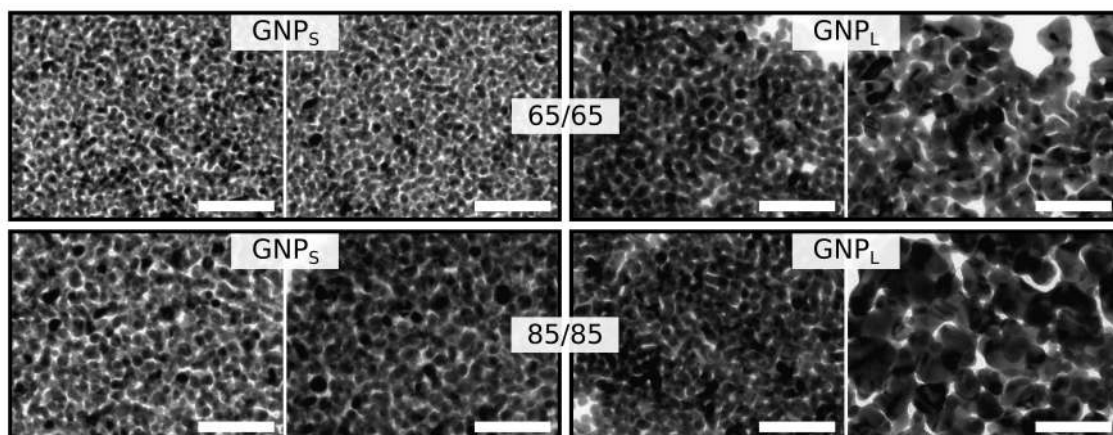


Figure 7.21: TEM images of GNP_S - and GNP_L -based particle systems. Images shown in the top row refer to the 65/65 test. Images shown in the bottom row refer to the 85/85 test. Between paired images, the left and right one refer to the particle system at day 0 and day 28, respectively. Note that different stock solutions were used for the GNP_S -based systems for the 65/65 and 85/85 tests, resulting in slightly different particle sizes at day 0. Scale bars: 50 nm. All GNP films were transferred onto TEM copper grids before aging.

Because the electrical and morphological changes in both particle systems are assumed to be correlated to the cross-linkers attached to the GNPs, XPS measurements were conducted with three different samples at day 0, day 2 and day 7 for both particle systems under 65/65 conditions. The samples were prepared via spin-coating and the GNPs were deposited onto unoxidized silicon wafers.

All samples were analyzed regarding the sulfur (S 2p) energy range and were fitted using two doublets of Gaussian functions, representing the S $2p_{1/2}$ and S $2p_{3/2}$ orbitals of thiol groups and gold-bound sulfur. In agreement with studies performed previously on cross-

linked GNPs, the peak at ~ 162 eV corresponds to gold-bound sulfur and the peak at ~ 164 eV corresponds to free thiol groups (S-H).^[30,62] Figure 7.22 a) and b) depict the XPS spectra of the S 2p energy range for the GNP_S and GNP_L system, respectively. The fit functions are shown as dashed and solid grey lines, respectively. For both particle systems no oxidized sulfur species, which are expected at higher binding energies (165–170 eV), were found in measurements of day 0 and day 2. For both particle systems a slight increase in the regime for oxidized sulfur is observable for the measurement at day 7 indicating the onset of degradation of the cross-linker. This phenomenon was also observed by Joseph et al.^[161] for GNPs aged under ambient/light conditions for several months and Schlicke et al. after irradiating cross-linked GNPs for two hours with DUV light, indicating as well accelerated aging effects.^[196] Figure parts c) and d) depict the relative sulfur concentrations (normalized to the corresponding Au 4f peak). The values are displayed as a fraction of the total thiol concentration of the GNP_S system at day 0.

This comparison shows, that the system comprised of the smaller particles contains significantly more free thiol groups as well as gold-bound sulfur. This is probably related to the increased surface to bulk ratio of the smaller particles. For both particle systems, the amount of gold-bound sulfur remains nearly constant after seven days of aging, whereas the amount of free thiol groups is reduced over time. The ratio of free thiol and gold-bound sulfur is approximately identical for both particle systems over the observed period of seven days. For the GNP_S-based system, however, the amount of free thiol is reduced by ~ 20 %, whereas for the GNP_L-based system the amount of free thiol is reduced by ~ 30 % after the aging of seven days. Note, that no total sulfur-to-gold ratio could be extracted in this scope, because the RSO_x peak was too small to be fitted. Since the gold-bound sulfur stays nearly constant over the aging period, these measurements might indicate that only free thiol undergoes oxidation or evaporates from the organic matrix. But it is also possible that sulfur is catalytically oxidized on the GNP's surface and then replaced by free thiols, which would also explain the reduction of the S-H amount. However, the evaporation process of free thiols was also found by Joseph et al. for GNPs aged under ambient conditions.^[161]

The removal of free thiol might increase the electrical conductivity due to volume loss of the organic matrix. The loss in volume could further promote the agglomeration of particles as it was observed during TEM analysis (cf. figure 7.21). The results shown here support the overall assumption that the smaller particles are better stabilized when following the used spin-coating fabrication procedure, probably due to the increased amount of thiol in the organic matrix. Here, a readjustment of the linker concentration for the larger particles could increase the stability of such composite material as well.

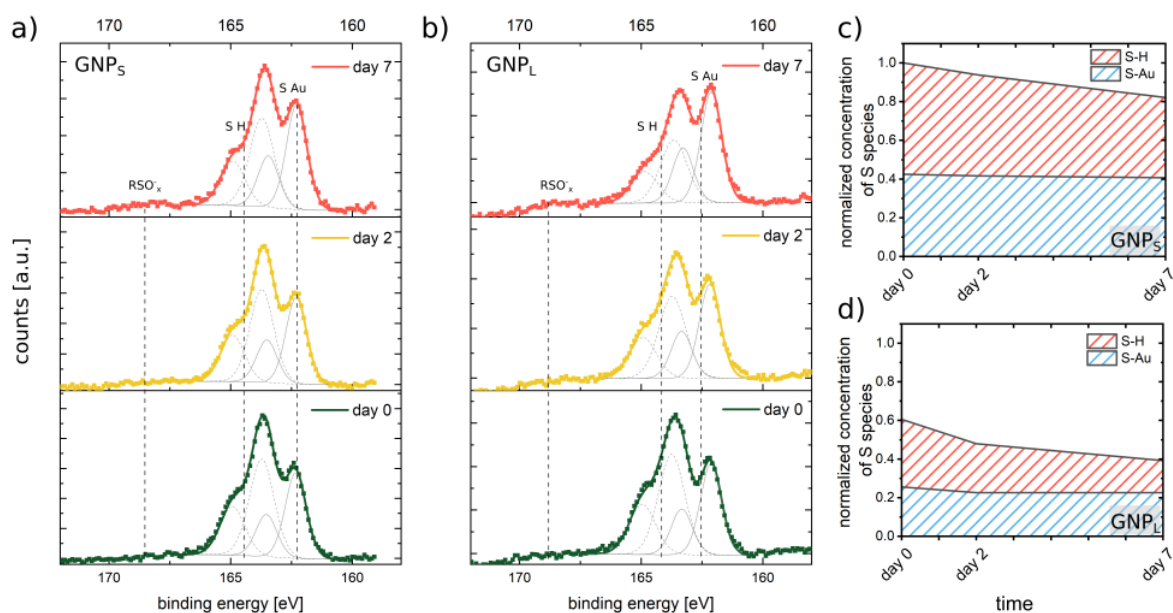


Figure 7.22: a) , b) XPS spectra of the GNP_S and GNP_L system cross-linked with 9DT at day 0, day 2 and day 7 during a 65/65 test, respectively. The plots show the S 2p energy range and the data was fitted using two doublets of Gaussian functions. The dashed gray lines correspond to the S H species, the solid gray lines correspond to the S Au species. c) , d) Relative S 2p concentrations as percentage of the maximum total S concentration measured (day 0 of sample GNP_S) for GNP_S and GNP_L, respectively.

Since the changes in electrical properties and TEM micrographs indicate strong changes in the films' structure, which are partly supported by the XPS measurements, charge transport measurements at temperatures from 100–300 K were conducted to obtain activation energies of the thermally activated tunneling of both particle systems.

To exclude any effects to the samples during the measurement due to the strong temperature deviations, three samples were used in total, one for day 0–7 and one for day 14 and day 28, respectively. One measurement lasted approximately eight hours. After the measurement was finished the sample was put again into the climate chamber.

The activation energy was obtained from the slope of an Arrhenius type plot according to equation 5.1. These measurements, however, show that the changes described above have only little effect on the activation energy when the particles are aged, as can be seen in figure 7.23. As expected, the smaller GNPs exhibit higher activation energies compared to the larger particle system (cf. equation 5.7). Note, the difference in activation energy of ~ 500 J/mol for the GNP_S system is due to the two different synthesis used which have a slightly different mean particle diameter (cf. figure 7.18). Here, the higher activation energies of ~ 4500 J/mol and ~ 4000 J/mol belong to the particle batches with mean diameters of ~ 3 nm and ~ 4 nm, respectively. All measurements show a slight decrease of the activation energy between day 0 and day 1 and a slight increase after the aging period

of 28 days. This increase might be due to the increase in particle size due to Ostwald ripening and the concomitant increase in interparticle distance. The latter effect may become dominant for longer aging periods, which then causes an increase in activation energy and cancels out the reduction due to the increase of the particle size (cf. equation 5.7).

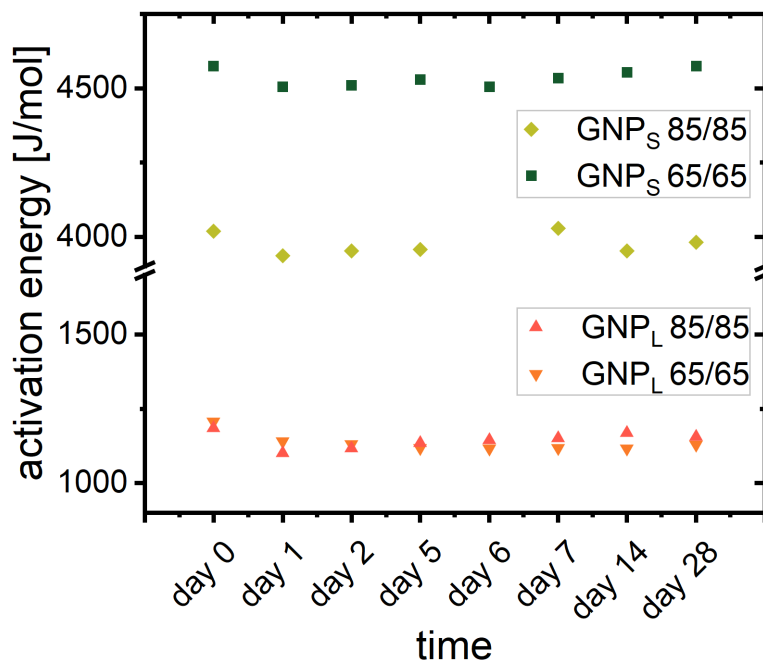


Figure 7.23: Activation energies of the thermally activated tunneling-based charge transport for both particle systems, GNP_S and GNP_L. The different activation energies of ~4500 J/mol and ~4000 J/mol belong to the two different particles batches (~3 nm and ~4 nm) used for the GNP_S particle system. The results show no significant changes during an aging period of 28 days for both testing conditions. Note that no measurement was performed for GNP_S at 85/85 for day six due to a measurement device failure.

The changes in activation energy, however, indicate only little changes in the film's morphology or at least the effects of different phenomena which cancel each other out, showing, that the fabricated GNP films have a high durability towards heat and moisture. This trend is supported by UV/vis, XRD and SAXS measurements providing analysis for areas in the millimeter regime. These experiments all show that the 65/65 and 85/85 tests have only little effect on the GNP films.

Figure 7.24 depicts normalized UV/vis spectra for both particle systems after 65/65 and 85/85 tests. A total of four samples was used, one for each particle system and artificial aging condition. The spectra show that the aging has nearly no effect on the particle agglomeration for the GNP_S-based system, which should result in a red-shift of the localized SPR band. For the GNP_L-based system a slight red-shift is observed for both

test conditions (figure 7.24 b), d), 65/65 and 85/85, which is a little more pronounced for the latter. This result is further supported by the observations obtained from the TEM measurements.

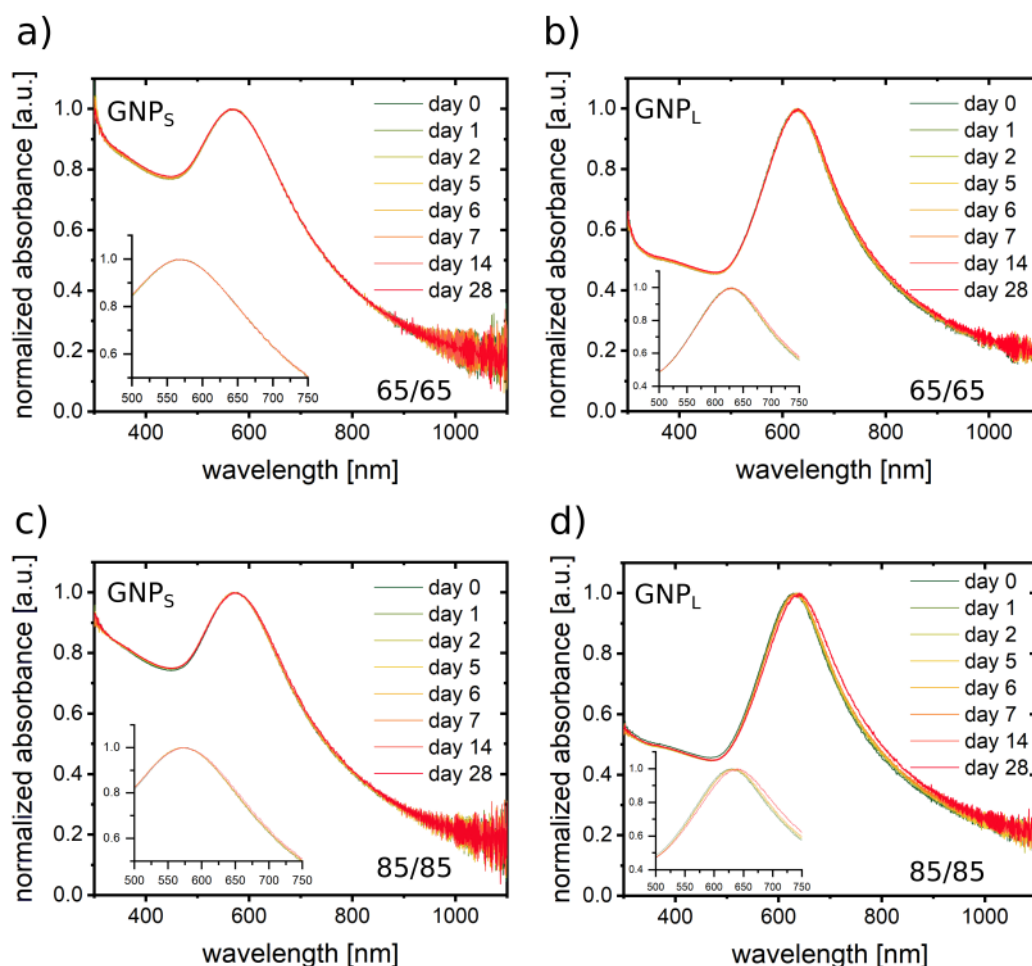


Figure 7.24: UV/vis absorbance spectra of GNP_S- and GNP_L-based systems. a) GNP_S 65/65. b) GNP_L 65/65. c) GNP_S 85/85. d) GNP_L 85/85. The insets show magnifications of the peak area.

Finally, XRD and SAXS measurements were performed to analyze possible changes in the crystallinity of both GNP systems during the aging process as well as the change of mean particle diameter and interparticle distance. For each of these methods a new sample was measured, so that effects of the x-ray sources to the particles during the measurement were excluded. It has to be noted, that due to the limitations of SAXS measurements only the GNP_L-based system could be analyzed. Since it was observed that the changes in the GNP films appear to be more pronounced at 85/85 conditions, both experiments were solely performed under these environmental conditions. Figure 7.25 a) shows XRD survey diffractograms from 30–120 ° as well as additional baseline-corrected diffractograms of the region between 55 and 90 °, where the gold (220) reflection is located. The results are in

good agreement with previously published data.^[30] The gold (220) reflections were fitted with a Lorentz fit. The obtained full widths at half-maximum, as well as the peak center $2\theta_0$ and the Scherrer equation (cf. equation 7.6) were used to estimate the domain sizes of the GNP films, which are in the range of 2.6–3.2 nm for both particle systems and do not follow any trend. These results suggest a negligible change of the particle domains during the aging process.

$$L = \frac{K\lambda}{w \cos \theta_0} \quad (7.6)$$

Here, L is the domain size, λ the wavelength of the x-ray source and K a shape factor, which was assumed to be 1.

Figure 7.25 b) shows SAXS measurements of the GNP_L-based system. The results as well show, that no significant changes happened to the composites macroscopic domain size and morphology during the aging process, since no broadening or shifting of the two maxima were observed.

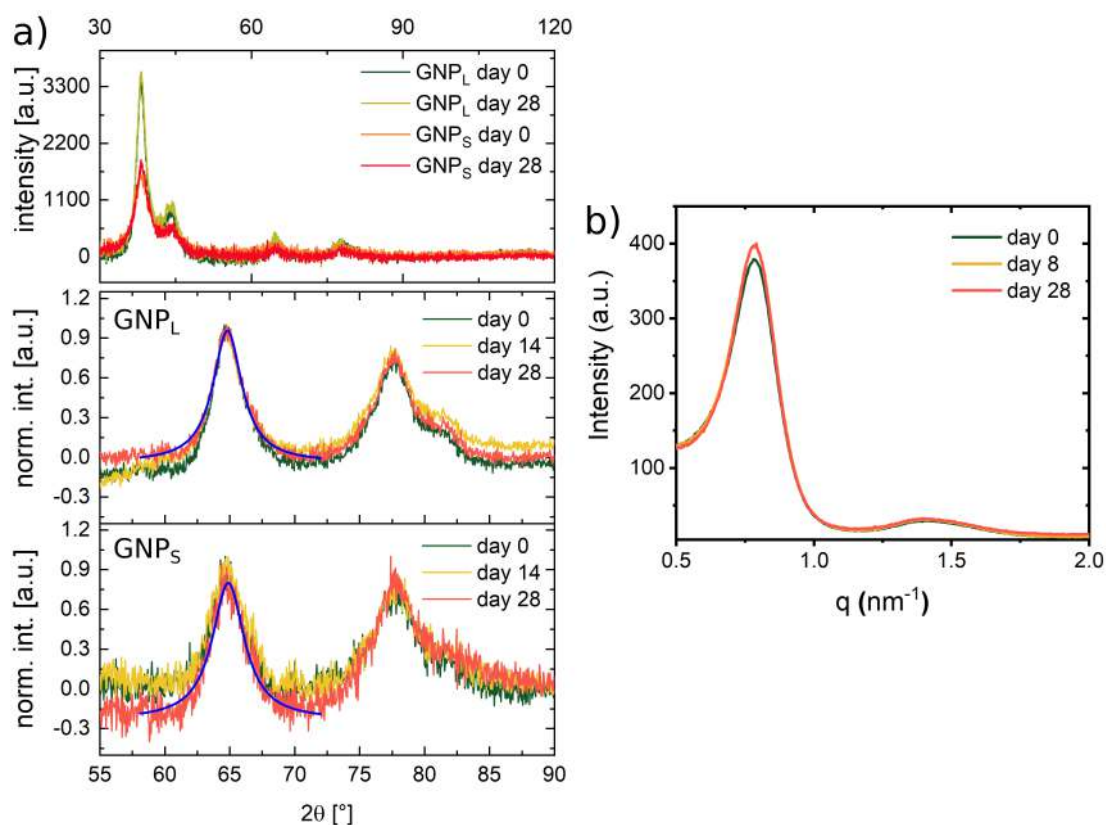


Figure 7.25: a) XRD survey diffractograms for both particle systems, as well as additional diffractograms in the range of the gold (220) reflection for day 0, day 14 and day 28 at 85/85 conditions. For the sake of clarity only one Lorentz fit (solid blue line) for day 28 is shown. b) SAXS pattern of the GNP_L -based system at three different days of artificial aging at 85/85 conditions. The measurements show that on the millimeter scale no significant peak shifts occurred, which indicate no noticeable change in the mean particle diameter or the particle distance.

It should be noted that in the scope of this work, aging experiments with samples aged in an additional climate chamber (Memmert, HCP50) at 85/85 conditions were conducted. To this end, I - V -measurements were performed with two samples from the GNP_L system aged in the HCP50 chamber and were compared to two freshly prepared samples aged in the WKL34/40 climate chamber. The results are depicted in the appendix figure A.10 a).

Though it could be shown that the samples aged in the WKL34/40 climate chamber exhibited only little changes in conductivities after seven days of aging (cf. figure 7.19 b), the results were inconsistent with the ones obtained for the samples aged in the HCP50 climate chamber (cf. figure A.10 a). Here, conductivities of up to two orders of magnitude higher were found compared to the samples aged in the WKL34/40 climate chamber. The temperature and humidity of both climate chambers were verified with an external sensor (cf. figure A.10 b), c), but no significant inconsistencies were observed. The origin of the different aging behaviors of the GNPs remained unclear and could not be clarified. These

results, however, show that the aging process of GNP composites is highly complex and needs further investigation.

Summary. The artificial aging of the GNP composites with two different mean particle diameters cross-linked with 9DT was analyzed with a variety of methods, focusing on electrical structural properties of the material. These results show, that the particle system comprised of the large particles (GNP_L) is generally more affected by the aging in terms of increased conductivity and particle agglomeration, whereas the small particles (GNP_S) remain highly stable under both artificial aging conditions (65/65 and 85/85) over the period of 28 days. However, millimeter scale analysis methods (UV/vis, XRD, SAXS) reveal, that on this scale both composites remain sufficiently stable to be used as sensors. Furthermore, electrical measurements showed that the aging process can be greatly inhibited by storing the composites under ambient temperature in a nitrogen atmosphere. It should be noted that the strong morphological changes shown by the TEM images might arise from the storage on the TEM copper grids during the whole aging period, whereas all other measurements were performed on GNPs supported by glass substrates or PI-foil. Finally, it was shown, that different climate chambers (WKL34/40 and HCP50) lead to different results of the aging experiments.

8 Bibliography

- [1] J. Turkevich, P. C. Stevenson, J. Hillier, *Discuss. Faraday Soc.* **1951**, *11*, 55–75.
- [2] S. D. Perrault, W. C. Chan, *J. Am. Chem. Soc.* **2009**, *131*, 17042–17043.
- [3] N. G. Bastús, J. Comenge, V. Puentes, *Langmuir* **2011**, *27*, 11098–11105.
- [4] N. R. Jana, L. Gearheart, C. J. Murphy, *Langmuir* **2001**, *17*, 6782–6786.
- [5] N. Harris, M. J. Ford, P. Mulvaney, M. B. Cortie, *Gold. Bull.* **2008**, *41*, 5–14.
- [6] J. Rodríguez-Fernández, J. Pérez-Juste, F. J. García De Abajo, L. M. Liz-Marzán, *Langmuir* **2006**, *22*, 7007–7010.
- [7] J. Pérez-Juste, L. M. Liz-Marzán, S. Carnie, D. Y. Chan, P. Mulvaney, *Adv. Funct. Mater.* **2004**, *14*, 571–579.
- [8] A. F. Leontowich, C. F. Calver, M. Dasog, R. W. Scott, *Langmuir* **2010**, *26*, 1285–1290.
- [9] Y. Li, O. Zaluzhna, C. D. Zangmeister, T. C. Allison, Y. J. Tong, *J. Am. Chem. Soc.* **2012**, *134*, 1990–1992.
- [10] T. J. Cho, R. A. Zangmeister, R. I. MacCuspie, A. K. Patri, V. A. Hackley, *Chem. Mater.* **2011**, *23*, 2665–2676.
- [11] M. Haruta, M. Daté, *Appl. Catal. A-Gen.* **2001**, *222*, 427–437.
- [12] R. Bardhan, S. Lal, A. Joshi, N. J. Halas, *Acc. Chem. Res.* **2011**, *44*, 936–946.
- [13] P. T. Mathew, F. Fang, *Engineering* **2018**, *4*, 760–771.
- [14] H. C. Chen, Y. C. Liu, *J. Ind. Eng. Chem.* **2018**, *60*, 9–18.
- [15] X. Hu, Y. Zhang, T. Ding, J. Liu, H. Zhao, *Front. Bioeng. Biotechnol.* **2020**, *8*, 1–17.
- [16] D. A. Giljohann, D. S. Seferos, W. L. Daniel, M. D. Massich, P. C. Patel, C. A. Mirkin, *Angew. Chem. Int. Ed.* **2010**, *49*, 3280–3294.
- [17] H. B. Yao, L. B. Mao, Y. X. Yan, H. P. Cong, X. Lei, S. H. Yu, *ACS Nano* **2012**, *6*, 8250–8260.
- [18] S. Burzhuev, A. Dâna, B. Ortaç, *Sens. Actuator A Phys.* **2013**, *203*, 131–136.

8. Bibliography

- [19] I. Oja Acik, L. Dolgov, M. Krunk, A. Mere, V. Mikli, S. Pikker, A. Loot, I. Sildos, *Thin Solid Films* **2014**, *553*, 144–147.
- [20] R. Elghanian, J. J. Storhoff, R. C. Mucic, R. L. Letsinger, C. A. Mirkin, *Science* **1997**, *277*, 1078–1081.
- [21] X. Huang, I. H. El-Sayed, W. Qian, M. A. El-Sayed, *J. Am. Chem. Soc.* **2006**, *128*, 2115–2120.
- [22] P. K. Jain, K. S. Lee, I. H. El-Sayed, M. A. El-Sayed, *J. Phys. Chem. B* **2006**, *110*, 7238–7248.
- [23] M. Brust, D. Bethell, C. J. Kiely, D. J. Schiffrin, *Langmuir* **1998**, *14*, 5425–5429.
- [24] X. B. Li, H. Y. Wang, X. D. Yang, Z. H. Zhu, Y. J. Tang, *J. Chem. Phys.* **2007**, *126*.
- [25] X. Zhao, X. Ding, Z. Deng, Z. Zheng, Y. Peng, X. Long, *Macromol. Rapid Commun.* **2005**, *26*, 1784–1787.
- [26] H. W. Cheng, S. Yan, G. Shang, S. Wang, C. J. Zhong, *Biosens. Bioelectron.* **2021**, *186*, 113268.
- [27] M. Segev-Bar, H. Haick, *ACS Nano* **2013**, *7*, 8366–8378.
- [28] W. Hu, L. Wan, Y. Jian, C. Ren, K. Jin, X. Su, X. Bai, H. Haick, M. Yao, W. Wu, *Adv. Mater. Technol.* **2019**, *4*, 1–38.
- [29] M. K. Nakhleh, Y. Y. Broza, H. Haick, *Nanomedicine* **2014**, *9*, 1991–2002.
- [30] H. Schlicke, S. Kunze, M. Finsel, E. W. Leib, C. J. Schröter, M. Blankenburg, H. Noei, T. Vossmeier, *J. Phys. Chem. C* **2019**, *123*, 19165–19174.
- [31] H. Schlicke, E. W. Leib, A. Petrov, J. H. Schröder, T. Vossmeier, *J. Phys. Chem. C* **2014**, *118*, 4386–4395.
- [32] K.-C. Yeh, Y. Chiang, S.-W. Chang, *Multiscale Sci. Eng.* **2020**, *2*, 242–251.
- [33] K. C. Yeh, Y. Y. Tsai, S. W. Chang, *J. Phys. Chem. C* **2022**, *126*, 6456–6464.
- [34] L. Tong, J. Guo, *Platin. Met. Rev.* **1994**, *38*, 98–108.
- [35] H. Moreira, J. Grisolia, N. M. Sangeetha, N. Decorde, C. Farcau, B. Viallet, K. Chen, G. Viau, L. Ressier, *Nanotechnology* **2013**, *24*, 095701.
- [36] N. M. Sangeetha, N. Decorde, B. Viallet, G. Viau, L. Ressier, *J. Phys. Chem. C* **2013**, *117*, 1935–1940.
- [37] S. H. Ha, S. H. Ha, M. B. Jeon, J. H. Cho, J. M. Kim, *Nanoscale* **2018**, *10*, 5105–5113.

- [38] K. K. Kim, S. Hong, H. M. Cho, J. Lee, Y. D. Suh, J. Ham, S. H. Ko, *Nano Lett.* **2015**, *15*, 5240–5247.
- [39] C.-W. Jiang, I.-C. Ni, S.-D. Tzeng, K. Watson, *Sci. Rep.* **2015**, *5*, 11939.
- [40] W. Zhao, J. Luo, S. Shan, J. P. Lombardi, Y. Xu, K. Cartwright, S. Lu, M. Poliks, C.-J. Zhong, *Small* **2015**, *11*, 4509–4516.
- [41] H. Li, J. Wu, X. Huang, Z. Yin, J. Liu, H. Zhang, *ACS Nano* **2014**, *8*, 6563–6570.
- [42] M. K. Choi, I. Park, D. C. Kim, E. Joh, O. K. Park, J. Kim, M. Kim, C. Choi, J. Yang, K. W. Cho, J.-H. Hwang, J.-M. Nam, T. Hyeon, J. H. Kim, D.-H. Kim, *Adv. Funct. Mater.* **2015**, *25*, 7109–7118.
- [43] E. Tekin, P. J. Smith, U. S. Schubert, *Soft Matter* **2008**, *4*, 703–713.
- [44] E. Chow, J. Herrmann, C. S. Barton, B. Raguse, L. Wiczorek, *Anal. Chim. Acta* **2009**, *632*, 135–142.
- [45] C. H. Su, H. L. Chiu, Y. C. Chen, M. Yesilmen, F. Schulz, B. Ketelsen, T. Vossmeier, Y. C. Liao, *Langmuir* **2019**, *35*, 3256–3264.
- [46] T. Kant, K. Shrivastava, K. Tapadia, R. Devi, V. Ganesan, M. K. Deb, *New J. Chem.* **2021**, *45*, 8297–8305.
- [47] C. S. Boland, U. Khan, G. Ryan, S. Barwich, R. Charifou, A. Harvey, C. Backes, Z. Li, M. S. Ferreira, M. E. Möbius, R. J. Young, J. N. Coleman, *Science* **2016**, *354*, 1257–1260.
- [48] C. Barberio, T. Chaudhry, D. Power, B. Lawless, D. Espino, S. Tan, J. Wilton, *J. Musculoskelet. Surg.* **2019**, *3*, 134.
- [49] I. Freestone, N. Meeks, M. Sax, C. Higgitt, *Gold Bull.* **2007**, *40*, 270–277.
- [50] F. E. Wagner, S. Haslbeck, L. Stievano, S. Calogero, Q. A. Pankhurst, K. P. Martinek, *Nature* **2000**, *407*, 691–692.
- [51] W. A. Weyl, *Coloured glasses*, Society of Glass Technology, Sheffield, UK, **1951**.
- [52] British Museum, (*accessed February 08, 2022*), https://www.britishmuseum.org/collection/object/H_1958-1202-1, **2022**.
- [53] P. Zhao, N. Li, D. Astruc, *Coord. Chem. Rev.* **2013**, *257*, 638–665.
- [54] R. Sardar, A. M. Funston, P. Mulvaney, R. W. Murray, *Langmuir* **2009**, *25*, 13840–13851.
- [55] G. Schmid, R. Pfeil, R. Boese, F. Bändermann, S. Meyer, G. H. M. Calis, J. W. A. van der Velden, *Chem. Ber.* **1981**, *114*, 3634–3642.

8. Bibliography

- [56] M. Brust, M. Walker, D. Bethell, D. Schiffrin, R. Whyman, *Chem. Comm.* **1994**, 7, 801–802.
- [57] D. V. Leff, L. Brandt, J. R. Heath, *Langmuir* **1996**, 12, 4723–4730.
- [58] F. Chen, X. Li, J. Hihath, Z. Huang, N. Tao, *J. Am. Chem. Soc.* **2006**, 128, 15874–15881.
- [59] D. V. Leff, P. C. Ohara, J. R. Heath, W. M. Gelbart, *J. Phys. Chem.* **1995**, 99, 7036–7041.
- [60] C. B. Murray, R. Kagan., M. Bawendi, *Annu. Rev. Mater. Sci.* **2000**, 30, 545–610.
- [61] S. Peng, Y. Lee, C. Wang, H. Yin, S. Dai, S. Sun, *Nano Res.* **2008**, 1, 229–234.
- [62] B. Ketelsen, M. Yesilmen, H. Schlicke, H. Noei, C.-H. Su, Y.-C. Liao, T. Vossmeier, *ACS Appl. Mater. Interfaces* **2018**, 10, 37374–37385.
- [63] N. Olichwer, E. W. Leib, A. H. Halfar, A. Petrov, T. Vossmeier, *ACS Appl. Mater. Interfaces* **2012**, 4, 6151–6161.
- [64] H. Schlicke, M. Rebber, S. Kunze, T. Vossmeier, *Nanoscale* **2016**, 8, 183–186.
- [65] M. A. Squillaci, X. Zhong, L. Peyruchat, C. Genet, T. W. Ebbesen, P. Samorì, *Nanoscale* **2019**, 11, 19315–19318.
- [66] L. Qin, G. Zeng, C. Lai, D. Huang, P. Xu, C. Zhang, M. Cheng, X. Liu, S. Liu, B. Li, H. Yi, *Coord. Chem. Rev.* **2018**, 359, 1–31.
- [67] J. Yi, Y. Xianyu, *Adv. Funct. Mater.* **2022**, 32, 2113012.
- [68] F. Schulz, T. Vossmeier, N. G. Bastús, H. Weller, *Langmuir* **2013**, 29, 9897–9908.
- [69] B. Begines, A. Alcudia, R. Aguilera-Velazquez, G. Martinez, Y. He, R. Wildman, M. J. Sayagues, A. Jimenez-Ruiz, R. Prado-Gotor, *Sci. Rep.* **2019**, 9, 1–12.
- [70] I. Kosif, K. Kratz, S. S. You, M. K. Bera, K. Kim, B. Leahy, T. Emrick, K. Y. C. Lee, B. Lin, *ACS Nano* **2017**, 11, 1292–1300.
- [71] H. Hartmann, J. N. Beyer, J. Hansen, S. C. Bittinger, M. Yesilmen, H. Schlicke, T. Vossmeier, *ACS Appl. Mater. Interfaces* **2021**, 13, 40932–40941.
- [72] H. Schlicke, S. Kunze, M. Rebber, N. Schulz, S. Riekeberg, H. K. Trieu, T. Vossmeier, *Adv. Funct. Mater.* **2020**, 30, 2003381.
- [73] H. Wohltjen, A. W. Snow, *Anal. Chem.* **1998**, 70, 2856–2859.
- [74] W. H. Steinecker, M. P. Rowe, E. T. Zellers, *Anal. Chem.* **2007**, 79, 4977–4986.
- [75] S. Claramunt, O. Monereo, M. Boix, R. Leghrib, J. D. Prades, A. Cornet, P. Merino, C. Merino, A. Cirera, *Sens. Actuators B Chem.* **2013**, 187, 401–406.

- [76] R. H. Terrill, T. A. Postlethwaite, C. H. Chen, C. D. Poon, A. Terzis, A. Chen, J. E. Hutchison, M. R. Clark, G. Wignall, J. D. Londono, M. Falvo, C. S. Johnson, E. T. Samulski, R. W. Murray, G. Wignall, J. D. Londono, R. H. Terrill, T. A. Postlethwaite, C. H. Chen, C. D. Poon, A. Terzis, A. Chen, J. E. Hutchison, M. R. Clark, G. Wignall, J. D. Londono, R. Superfine, M. Falvo, C. S. Johnson, E. T. Samulski, R. W. Murray, *J. Am. Chem. Soc.* **1995**, *117*, 12537–12548.
- [77] T. Gao, C. Zhang, Y. Wang, J. A. Diaz, J. Zhao, B. G. Willis, *IEEE Sens. J.* **2020**, *20*, 14016–14023.
- [78] G. Schmid, *J. Chem. Soc. - Dalt. Trans.* **1998**, 1077–1082.
- [79] Y. Zhao, S. Gschossmann, M. Schagerl, P. Gruener, C. Kralovec, *Smart Mater. Struct.* **2018**, *27*, 105009.
- [80] M. Rieu, M. Camara, G. Tournier, J. P. Viricelle, C. Pijolat, N. F. de Rooij, D. Briand, *Sens. Actuators B Chem.* **2016**, *236*, 1091–1097.
- [81] B. Ketelsen, P. P. Tjarks, H. Schlicke, Y. C. Liao, T. Vossmeier, *Chemosensors* **2020**, *8*, 1–14.
- [82] J. Cho, K. Char, J. D. Hong, K. B. Lee, *Adv. Mater.* **2001**, *13*, 1076–1078.
- [83] Y. Joseph, I. Besnard, M. Rosenberger, B. Guse, H.-G. Nothofer, J. M. Wessels, U. Wild, A. Knop-Gericke, D. Su, R. Schlägl, A. Yasuda, T. Vossmeier, *J. Phys. Chem. B* **2003**, *107*, 7406–7413.
- [84] H. Schlicke, S. C. Bittinger, T. Vossmeier, *ACS Appl. Electron. Mater.* **2020**, *2*, 3741–3748.
- [85] C. Han, S. J. Percival, B. Zhang, *Langmuir* **2016**, *32*, 8783–8792.
- [86] D. S. Lee, M. J. Ki, H. J. Lee, J. K. Park, S. Y. Hong, B. W. Kim, J. H. Heo, S. H. Im, *ACS Appl. Mater. Interfaces* **2022**, *14*, 7926–7935.
- [87] H. C. Wang, Y. Hong, Z. Chen, C. Lao, Y. Lu, Z. Yang, Y. Zhu, X. Liu, *Nanoscale Res. Lett.* **2020**, *15*, 1–7.
- [88] W. A. D. M. Jayathilaka, K. Qi, Y. Qin, A. Chinnappan, W. Serrano-García, C. Baskar, H. Wang, J. He, S. Cui, S. W. Thomas, S. Ramakrishna, *Adv. Mater.* **2019**, *31*, 1–21.
- [89] T. Xu, J. Jin, C. Gregory, J. J. Hickman, T. Boland, *Biomaterials* **2005**, *26*, 93–99.
- [90] B. Derby, *J. Eur. Ceram. Soc.* **2011**, *31*, 2543–2550.
- [91] S. H. Ko, J. Chung, N. Hotz, K. H. Nam, C. P. Grigoropoulos, *J. Micromech. Microeng.* **2010**, *20*, 125010.

8. Bibliography

- [92] S. E. Evans, T. Harrington, M. C. Rodriguez Rivero, E. Rognin, T. Tuladhar, R. Daly, *Int. J. Pharm.* **2021**, *599*, 120443.
- [93] L. Gih-Keong, M. Shrestha, *Micromachines* **2017**, *8*, 194.
- [94] M. M. Mohebi, J. R. Evans, *J. Comb. Chem.* **2002**, *4*, 267–274.
- [95] C. H. Wu, W. S. Hwang, *Microelectron. Reliab.* **2015**, *55*, 630–636.
- [96] Y. F. Liu, M. H. Tsai, Y. F. Pai, W. S. Hwang, *Appl. Phys. A* **2013**, *111*, 509–516.
- [97] H. Y. Jun, S. J. Kim, C. H. Choi, *Nanomaterials* **2021**, *11*, 3441.
- [98] M. M. De Villiers, D. P. Otto, S. J. Strydom, Y. M. Lvov, *Adv. Drug Deliv. Rev.* **2011**, *63*, 701–715.
- [99] F. Schulz, I. Lokteva, W. J. Parak, F. Lehmkuhler, *Part. Part. Syst. Charact.* **2021**, *38*, 2100087.
- [100] H. Schlicke, J. H. Schroeder, M. Trebbin, A. Petrov, M. Ijeh, H. Weller, T. Vossmeier, *Nanotechnology* **2011**, 305303(9pp).
- [101] S. T. Han, Y. Zhou, Z. X. Xu, L. B. Huang, X. B. Yang, V. A. Roy, *Adv. Mater.* **2012**, *24*, 3556–3561.
- [102] M. Brust, D. J. Schiffrin, D. Bethell, C. J. Kiely, *Adv. Mater.* **1995**, *7*, 795–797.
- [103] J. M. Wessels, H.-G. Nothofer, W. E. Ford, F. von Wrochem, F. Scholz, T. Vossmeier, A. Schroedter, H. Weller, A. Yasuda, *J. Am. Chem. Soc.* **2004**, *126*, 3349–3356.
- [104] L. Yi, W. Jiao, C. Zhu, K. Wu, C. Zhang, L. Qian, S. Wang, Y. Jiang, S. Yuan, *Nano Res.* **2016**, *9*, 1346–1357.
- [105] H. Schlicke, D. Battista, S. Kunze, C. J. Schröter, M. Eich, T. Vossmeier, *ACS Appl. Mater. Interfaces* **2015**, *7*, 15123–15128.
- [106] W. S. Lee, S.-W. Lee, H. Joh, M. Seong, H. Kim, M. S. Kang, K.-H. Cho, Y.-M. Sung, S. J. Oh, *Small* **2017**, *13*, 1702534.
- [107] H. Müller, G. Wei, B. Raguse, J. Myers, *Phys. Rev. B Condens. Matter* **2003**, *68*, 1–6.
- [108] C. A. Neugebauer, M. B. Webb, *J. Appl. Phys.* **1962**, *33*, 74–82.
- [109] A. Salomon, D. Cahen, S. Lindsay, J. Tomfohr, V. B. Engelkes, C. D. Frisbie, *Adv. Mater.* **2003**, *15*, 1881–1890.
- [110] W. P. Wuelfing, S. J. Green, J. J. Pietron, D. E. Cliffl, R. W. Murray, *J. Am. Chem. Soc.* **2000**, *122*, 11465–11472.

-
- [111] X. D. Cui, A. Primak, X. Zarate, J. Tomfohr, O. F. Sankey, A. L. Moore, T. A. Moore, D. Gust, L. A. Nagahara, S. M. Lindsay, *J. Phys. Chem. B* **2002**, *106*, 8609–8614.
- [112] B. Abeles, P. Sheng, M. D. Coutts, Y. Arie, *Adv. Phys.* **1975**, *24*, 407–461.
- [113] A. Zabet-Khosousi, A.-A. Dhirani, *Chem. Rev.* **2008**, *108*, 4072–4124.
- [114] K. I. Bolotin, F. Kuemmeth, A. N. Pasupathy, D. C. Ralph, *Appl. Phys. Lett.* **2004**, *84*, 3154–3156.
- [115] R. A. Marcus, N. Sutin, *Biochim. Biophys. Acta* **1985**, *811*, 265–322.
- [116] R. A. Marcus, *Angew. Chem. Int. Ed. Engl.* **1993**, *32*, 1111–1121.
- [117] W. P. Wuelfing, R. W. Murray, *J. Phys. Chem. B* **2002**, *106*, 3139–3145.
- [118] T. Vossmeier, C. Stolte, M. Ijeh, A. Kornowski, H. Weller, *Adv. Funct. Mater.* **2008**, *18*, 1611–1616.
- [119] J. Herrmann, K. H. Müller, T. Reda, G. R. Baxter, B. Raguse, G. J. De Groot, R. Chai, M. Roberts, L. Wiczorek, *Appl. Phys. Lett.* **2007**, *91*, 1–4.
- [120] S. Keil, *Dehnungsmessstreifen*, Springer Vieweg, **2017**.
- [121] C. Farcau, H. Moreira, B. Viallet, J. Grisolia, D. Ciuculescu-Pradines, C. Amiens, L. Ressler, *J. Phys. Chem. C* **2011**, *115*, 14494–14499.
- [122] C. B. Huang, Y. Yao, V. Montes-García, M. A. Stoeckel, M. Von Holst, A. Ciesielski, P. Samorì, *Small* **2021**, *17*, 1–6.
- [123] H. Chen, Y. Jing, J. H. Lee, D. Liu, J. Kim, S. Chen, K. Huang, X. Shen, Q. Zheng, J. Yang, S. Jeon, J. K. Kim, *Mater. Horiz.* **2020**, *7*, 2378–2389.
- [124] A. Wymysłowski, M. Santo-Zarnik, K. Friedel, D. Belavič, *Proc. 5th Int. Conf. Therm. Mech. Simul. Exp. Microelectron. Microsystems EuroSimE 2004* **2004**, 359–366.
- [125] N. White, A. Cranny, *Microelectron. Int.* **1987**, *4*, 32–35.
- [126] F. Zhang, P. C. Ma, J. Wang, Q. Zhang, W. Feng, Y. Zhu, Q. Zheng, *Mater. Horizons* **2021**, *8*, 2615–2653.
- [127] T. W. Richards, J. W. Shipley, C. B. T W Richards, *J. Am. Chem. Soc.* **1919**, *41*, 2002–2012.
- [128] Y. Joseph, A. Peie, X. Chen, J. Michl, T. Vossmeier, A. Yasuda, A. Peić, X. Chen, J. Michl, T. Vossmeier, A. Yasuda, A. Peie, X. Chen, J. Michl, T. Vossmeier, A. Yasuda, *J. Phys. Chem. C* **2007**, *111*, 12855–12859.

8. Bibliography

- [129] N. Olichwer, A. Meyer, M. Yesilmen, T. Vossmeier, *J. Mater. Chem. C* **2016**, *4*, 8214–8225.
- [130] L. Wang, J. Luo, J. Yin, H. Zhang, J. Wu, X. Shi, E. Crew, Z. Xu, Q. Rendeng, S. Lu, M. Poliks, B. Sammakia, C.-J. J. Zhong, *J. Mater. Chem.* **2010**, *20*, 907–915.
- [131] M. Tonezzer, L. T. Dang, H. Q. Tran, S. Iannotta, *Sens. Actuators B Chem.* **2018**, *255*, 2785–2793.
- [132] U. Tisch, H. H. Haick, *Rev. Chem. Eng.* **2011**, *26*, 171–179.
- [133] Y. Liao, R. Zhang, J. Qian, *RSC Adv.* **2019**, *9*, 29154–29172.
- [134] K. Persaud, G. Dodd, *Nature* **1982**, *299*, 352–355.
- [135] S. Lekha, M. Suchetha, *IEEE Rev. Biomed. Eng.* **2021**, *14*, 127–138.
- [136] J. S. Cooper, B. Raguse, E. Chow, L. Hubble, K.-H. Müller, L. Wieczorek, *Anal. Chem.* **2010**, *82*, 3788–3795.
- [137] P. Gupta, H. Gholami Derami, D. Mehta, H. Yilmaz, S. Chakrabartty, B. Raman, S. Singamaneni, *ACS Appl. Mater. Interfaces* **2022**, *14*, 3207–3217.
- [138] K. E. Mueggenburg, X. M. Lin, R. H. Goldsmith, H. M. Jaeger, *Nat. Mater.* **2007**, *6*, 656–660.
- [139] P. A. Chiarelli, M. S. Johal, J. L. Casson, J. B. Roberts, J. M. Robinson, H. L. Wang, *Adv. Mater.* **2001**, *13*, 1167–1171.
- [140] A. A. Mamedov, N. A. Kotov, *Langmuir* **2000**, *16*, 5530–5533.
- [141] A. A. Mamedov, N. A. Kotov, M. Prato, D. M. Guldi, J. P. Wicksted, A. Hirsch, *Nat. Mater.* **2002**, *1*, 190–194.
- [142] C. Jiang, S. Markutsya, Y. Pikus, V. V. Tsukruk, *Nat. Mater.* **2004**, *3*, 721–728.
- [143] S. Markutsya, C. Jiang, Y. Pikus, V. V. Tsukruk, *Adv. Funct. Mater.* **2005**, *15*, 771–780.
- [144] B. Kowalczyk, M. M. Apodaca, H. Nakanishi, S. K. Smoukov, B. A. Grzybowski, *Small* **2009**, *5*, 1970–1973.
- [145] D. Mordehai, M. Kazakevich, D. J. Srolovitz, E. Rabkin, *Acta Mater.* **2011**, *59*, 2309–2321.
- [146] Y. Wang, P. Kanjanaboos, S. P. McBride, E. Barry, X. M. Lin, H. M. Jaeger, *Faraday Discuss.* **2015**, *181*, 325–338.
- [147] E. Tam, P. Podsiadlo, E. Shevchenko, D. F. Ogletree, M. P. Delplancke-Ogletree, P. D. Ashby, *Nano Lett.* **2010**, *10*, 2363–2367.

-
- [148] P. Podsiadlo, G. Krylova, B. Lee, K. Critchley, D. J. Gosztola, D. V. Talapin, P. D. Ashby, E. V. Shevchenko, *J. Am. Chem. Soc.* **2010**, *132*, 8953–8960.
- [149] U. Landman, W. D. Luedtke, *Faraday Discuss.* **2004**, *125*, 1–22.
- [150] M. Gauvin, Y. Wan, I. Arfaoui, M. P. Pileni, *J. Phys. Chem. C* **2014**, *118*, 5005–5012.
- [151] C. Yan, I. Arfaoui, N. Goubet, M. P. Pileni, *Adv. Funct. Mater.* **2013**, *23*, 2315–2321.
- [152] T. R. Hendricks, W. Wang, I. Lee, *Soft Matter* **2010**, *6*, 3701–3706.
- [153] C. Jiang, H. Ko, V. V. Tsukruk, *Adv. Mater.* **2005**, *17*, 2127–2131.
- [154] X. Zhang, C. Neumann, P. Angelova, A. Beyer, A. Götzhäuser, *Langmuir* **2014**, *30*, 8221–8227.
- [155] A. Hensel, C. J. Schröter, H. Schlicke, N. Schulz, S. Riekeberg, H. K. Trieu, A. Stierle, H. Noei, H. Weller, T. Vossmeier, *Nanomaterials* **2019**, *9*, 1230.
- [156] J. J. Vlassak, W. D. Nix, *J. Mater. Res.* **1992**, *7*, 3242–3249.
- [157] Schlicke, H., Cross-Linked Gold Nanoparticle Membranes: Novel Materials for Electromechanical Sensors and Actuators. Dissertation, Universität Hamburg, **2017**.
- [158] M. Dasog, R. W. Scott, *Langmuir* **2007**, *23*, 3381–3387.
- [159] W. Hou, M. Dasog, R. W. Scott, *Langmuir* **2009**, *25*, 12954–12961.
- [160] J. Lacava, A. Weber, T. Kraus, *Part. Part. Syst. Charact.* **2015**, *32*, 458–466.
- [161] Y. Joseph, B. Guse, G. Nelles, *Chem. Mater.* **2009**, *21*, 1670–1676.
- [162] National Research Council, *Accelerated Aging of Materials and Structures: The Effects of Long-Term Elevated-Temperature Exposure*. Washington, DC: The National Academies Press., **1996**.
- [163] A. Bagi, D. M. Pampanin, O. G. Brakstad, R. Kommedal, *Mar. Environ. Res.* **2013**, *89*, 83–90.
- [164] X. Liao, Z. Zhang, Q. Liang, Q. Liao, Y. Zhang, *ACS Appl. Mater. Interfaces* **2017**, *9*, 4151–4158.
- [165] Y. Wang, S. Gong, S. J. Wang, X. Yang, Y. Ling, L. W. Yap, D. Dong, G. P. Simon, W. Cheng, *ACS Nano* **2018**, *12*, 9742–9749.
- [166] J. Ma, Y. Li, X. Zhou, X. Yang, F. A. Alharthi, A. A. Alghamdi, X. Cheng, Y. Deng, *Small* **2020**, *16*, 1–10.

8. Bibliography

- [167] S. K. Kim, C. Jeon, G. H. Lee, J. Koo, S. H. Cho, S. Han, M. H. Shin, J. Y. Sim, S. K. Hahn, *ACS Appl. Mater. Interfaces* **2019**, *11*, 37347–37356.
- [168] S. Wang, W. Lu, O. Tovmachenko, U. S. Rai, H. Yu, P. C. Ray, *Chem. Phys. Lett.* **2008**, *463*, 145–149.
- [169] T. Q. Trung, L. T. Duy, S. Ramasundaram, N. E. Lee, *Nano Res.* **2017**, *10*, 2021–2033.
- [170] P. G. Su, W. L. Shiu, M. S. Tsai, *Sens. Actuators B Chem.* **2015**, *216*, 467–475.
- [171] R. Zhang, B. Peng, Y. Yuan, *Compos. Sci. Technol.* **2018**, *168*, 118–125.
- [172] M. A. Squillaci, M. A. Stoeckel, P. Samorì, *Nanoscale* **2019**, *11*, 19319–19326.
- [173] R. Vishinkin, H. Haick, *Small* **2015**, *11*, 6142–6164.
- [174] Z. Li, J. Chen, L. Chen, M. Guo, Y. Wu, Y. Wei, J. Wang, X. Wang, *ACS Appl. Mater. Interfaces* **2020**, *12*, 55056–55063.
- [175] G. Roglic, *Int. J. Noncommun. Dis.* **2016**, *1*, 3–8.
- [176] X. Xuan, H. S. Yoon, J. Y. Park, *Biosens. Bioelectron.* **2018**, *109*, 75–82.
- [177] M. Middeke, *MMW - Fortschritte der Medizin* **2012**, *154*, 61–64.
- [178] I. You, B. Kim, J. Park, K. Koh, S. Shin, S. Jung, U. Jeong, *Adv. Mater.* **2016**, *28*, 6359–6364.
- [179] S. Gong, D. T. Lai, B. Su, K. J. Si, Z. Ma, L. W. Yap, P. Guo, W. Cheng, *Adv. Electron. Mater.* **2015**, *1*, 1–7.
- [180] S. Gong, D. T. Lai, Y. Wang, L. W. Yap, K. J. Si, Q. Shi, N. N. Jason, T. Sridhar, H. Uddin, W. Cheng, *ACS Appl. Mater. Interfaces* **2015**, *7*, 19700–19708.
- [181] S. Duan, Z. Wang, L. Zhang, J. Liu, C. Li, *Adv. Mater. Technol.* **2018**, *3*, 1–8.
- [182] T. An, D. V. Anaya, S. Gong, L. W. Yap, F. Lin, R. Wang, M. R. Yuce, W. Cheng, *Nano Energy* **2020**, *77*, 105295.
- [183] G. H. Lim, N. E. Lee, B. Lim, *J. Mater. Chem. C* **2016**, *4*, 5642–5647.
- [184] W. Haiss, N. T. K. Thanh, J. Aveyard, D. G. Fernig, *Anal. Chem.* **2007**, *79*, 4215–4221.
- [185] C. A. Schneider, W. S. Rasband, K. W. Eliceiri, *Nat. Methods* **2012**, *9*, 671–675.
- [186] A. Stierle, T. F. Keller, H. Noei, V. Vonk, R. Roehlsberger, *J. Large-Scale Res. Facil.* **2016**, *A76*, 1–9.

- [187] TU Delft, *Informed Consent Templates and Guide* (accessed February 08, 2022), <https://www.tudelft.nl/over-tu-delft/strategie/integriteitsbeleid/human-research-ethics/informed-consent-templates-and-guide>, **2022**.
- [188] Advanced Synthetic Engineering Components (ASEC), (accessed March 24, 2022), <https://asekunststoffen.nl/wp-content/uploads/2016/05/Datasheet-AS-EP-GC-202.pdf>, **2022**.
- [189] J. He, P. Kanjanaboos, N. L. Frazer, A. Weis, X. M. Lin, H. M. Jaeger, *Small* **2010**, *6*, 1449–1456.
- [190] P. Kanjanaboos, A. Joshi-Imre, X. M. Lin, H. M. Jaeger, *Nano Lett.* **2011**, *11*, 2567–2571.
- [191] H. Nesser, J. Grisolia, T. Alnasser, B. Viallet, L. Ressler, *Nanoscale* **2018**, *10*, 10479–10487.
- [192] E. Aslanidis, E. Skotadis, D. Tsoukalas, *Nanoscale* **2021**, *13*, 3263–3274.
- [193] M. J. Catenacci, C. Reyes, M. A. Cruz, B. J. Wiley, *ACS Nano* **2018**, *12*, 3689–3698.
- [194] J. Kwon, J. Ock, N. Kim, *Materials* **2020**, *13*, 5042.
- [195] C. S. Boland, *ACS Nano* **2019**, *13*, 13627–13636.
- [196] H. Schlicke, S. C. Bittinger, H. Noei, T. Vossmeier, *ACS Appl. Nano Mater.* **2021**, *4*, 10399–10408.
- [197] Y. Joseph, B. Guse, A. Yasuda, T. Vossmeier, *Sens. Actuators B Chem.* **2004**, *98*, 188–195.
- [198] H. R. Kemme, S. I. Kreps, *J. Chem. Eng. Data* **1969**, *14*, 98–102.
- [199] D. Ambrose, C. H. Sprake, *J. Chem. Thermodyn.* **1970**, *2*, 631–645.
- [200] Jedec Standard No. 22-A101 Test Method A101, (accessed April 12, 2022), <https://docplayer.net/36338779-Jedec-solid-state-technology-association.html>, **2022**.
- [201] D. Panjwani, A. Dutta, J. Nath, H. Heinrich, R. E. Peale, *J. Appl. Phys.* **2015**, *118*, 154307.
- [202] Y. Yu, B. W. Goodfellow, M. R. Rasch, C. Bosoy, D. M. Smilgies, B. A. Korgel, *Langmuir* **2015**, *31*, 6924–6932.
- [203] J. Gubicza, J. L. Lábár, L. M. Quynh, N. H. Nam, N. H. Luong, *Mater. Chem. Phys.* **2013**, *138*, 449–453.

A Appendix

A.1 Cryocell Setup

The cryocell setup comprises of a test cell (figure A.1 a) which is inserted into a dewar containing liquid nitrogen. The GNP films on glass were inserted into the measurement cell by gently lifting the printed circuit board containing spring loaded pins to contact the electrodes of the sample. The measurement cell was inserted into a copper block containing the heat elements and was fixated using screws. The measurement cell was grounded and inserted into a metal cylinder, so that it has no direct contact to the liquid nitrogen. A custom written Python routine was used to automatically run through pre-defined target temperatures and perform IV-measurements if the total error and standard deviation of the respective target temperature were below 0.35 for five minutes.

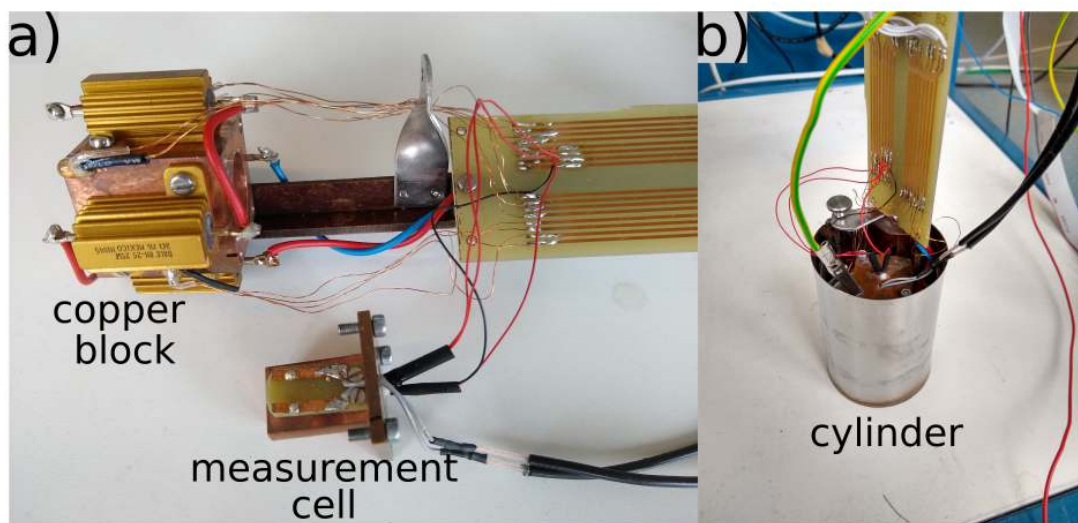


Figure A.1: Cryocell setup for activation energy measurements for temperature activated charge transport. *a)* Measurement cell for sample insertion and copper block. *b)* Test cell and copper block inserted in the metal cylinder to be inserted into the dewar.

A.2 Four Point Flexural Bending Setup

The bending test setup consisted of a threaded rod (pitch: 1 mm) connected to a stepper motor (Nema 23). The rod was mounted to a custom-built metal plate with two adjustable pins, which could be moved towards two additional pins mounted on a ground plate. The stepper motor was controlled by a commercial drivers board (TB6560), which was connected to a micro controller (MEGA 2560 R3, Elegoo). The stepper motor was powered with a bias of 24 V. A custom Python script was used to execute desired testing parameters. In order to achieve a smooth movement of the stepper motor, the step size was set to 1/16 of a full step, resulting in single steps of $\sim 0.1^\circ$. The electrical measurements for the sensor samples and the commercial sensor were performed using two Keithley 2601 A SMUs. Figure A.2 shows an overview image as well as an image of the inside of the test chamber. Here, the four pins as well as the moving metal plate are marked with red and blue squares, respectively.

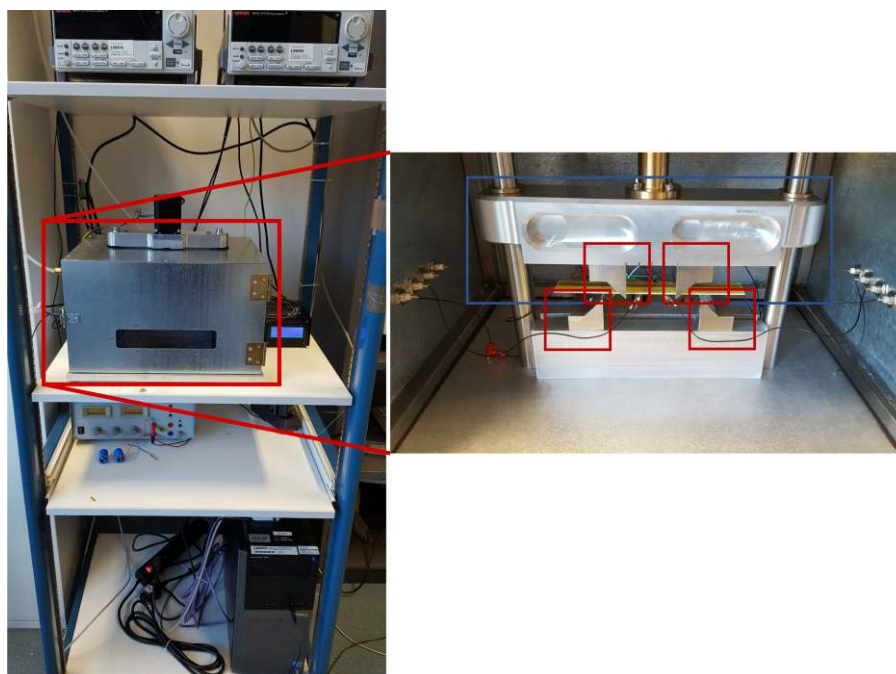


Figure A.2: Images of the overall flexural bending setup, as well as an inside view of the test chamber. Both SMUs are located above the test chamber. The power source for the stepper motor, as well as the computer to control the setup are located below the test chamber in the rack. The four pins as well as the moving metal plate are marked with red and blue squares, respectively, in the inside view image of the test chamber.

A.3 Strain Measurements of Rectangular Sensors with 400 μm and 800 μm Gap

In the following graph (figure A.3 b), strain measurements of rectangular sensors with 400 and 800 μm gaps at different angles are shown. The samples were fabricated similar to the sample described in the main document. Additionally, figure A.3 c) shows strain measurements performed up to strains of 0.26 %. These measurements show, that the direction dependency is preserved even at strains, where the commercial sensor and the simulation diverge from their linear behavior.

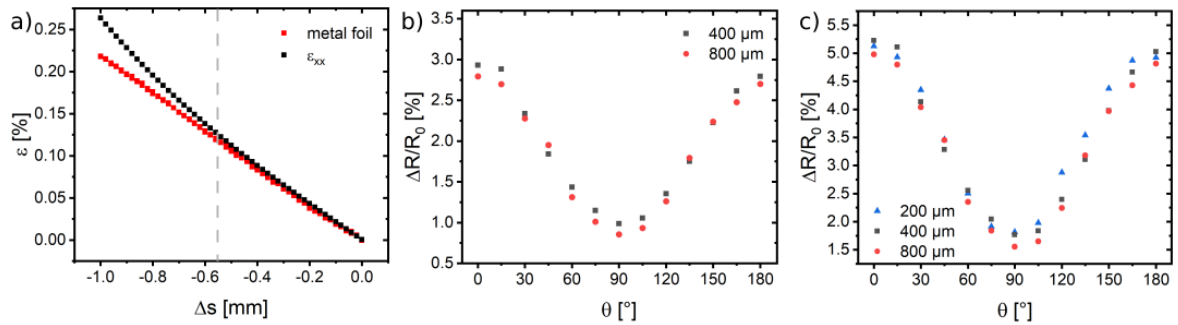


Figure A.3: a) Comparison showing a commercial sensor (SGT-1/350-TY11) and ϵ_{xx} plotted against the displacement Δs . Both graphs show a linear behavior up to a deflection of 0.55 mm, which corresponds to a strain of $\sim 0.12\%$. b) Angular dependent response curves at strains of 0.12 % for rectangular sensors with an electrode gap L of 400 and 800 μm , respectively. Measurements were performed at angles θ from 0° – 180° at steps of 15° . c) Similar measurements performed as shown in figure part b). The relative changes in resistance are plotted at strains of 0.26 %.

A.4 Comsol Strain Simulation for Shear Strain

The following graph shows the results of Comsol simulations for the shear strain ϵ_{xy} performed for an FR4 substrate disc used as described in the main document. It can be seen, that the shear strain is approximately three orders of magnitude smaller than the strains ϵ_{xx} and ϵ_{yy} , which are in the range of $\sim 10^{-3}$. Hence, this strain component can be neglected.

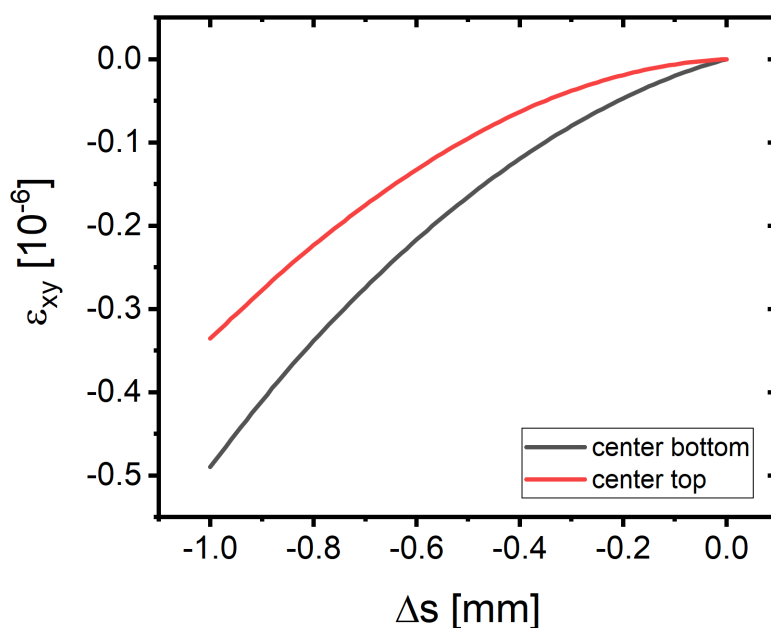


Figure A.4: Shear strain ϵ_{xy} at two points of the circular shaped FR4 substrate obtained from Comsol simulations plotted against the displacement Δs .

A.5 Response Transients Before and After Bending Fully Printed Chemiresistors

The following figure shows the resistive responses to toluene vapor after bending the fully printed sensor S-9DT at different radii of curvature (16 mm, 10 mm, 5 mm). For each radius the sensor was bent 100 times before the chemiresistor measurement was conducted. It can be clearly seen, that the repetitive bending has no significant influence on the sensor's sensitivity. According to optical micrographs, no delamination of the GNP transducer or the electrodes was observed.

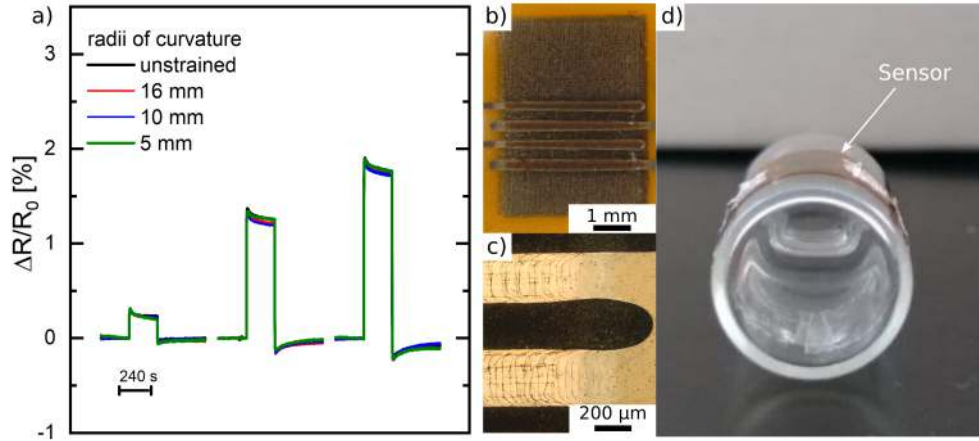


Figure A.5: Resistive responses to toluene vapor at concentrations of 100, 600 and 1000 ppm compared to a measurement performed before the sensor was bent. At each radius of curvature the sensor was bent 100 times. *b)*, *c)* Micrographs showing the sensor after bending it 100 times around a radius of curvature of 5 mm. No defects or delaminations were observed. *d)* Sensor fixated onto a vial with a radius of curvature of 5 mm. Adapted with permission from Ref. [81]

A.6 Custom-Built Multiplexer Setup for Chemiresistor Readout

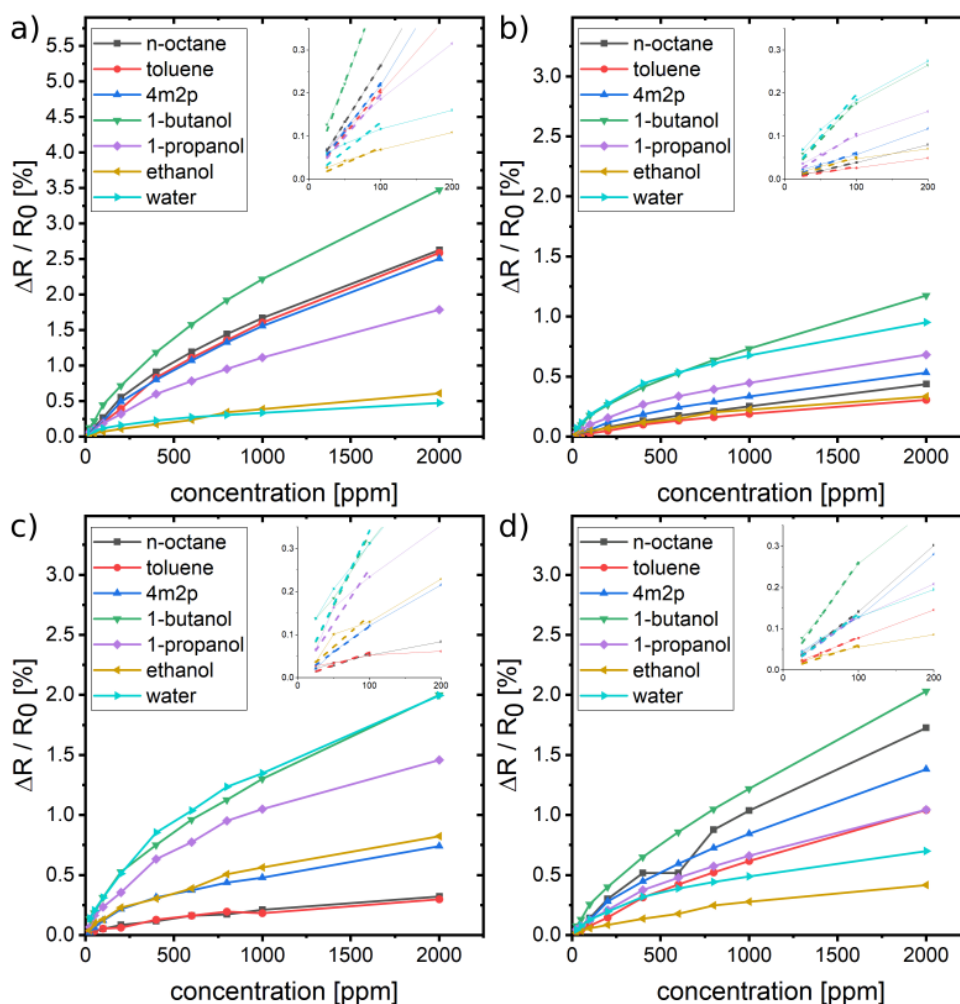
Each of the seven sensors was connected in series to a shunt resistor (tolerance: 0.1 %) and a constant bias of 5 V was applied to all sensor-shunt pairs using a Keithley 2601A. The shunt resistors are selected to have ~ 5 % of the printed sensor's baseline resistance. A multiplexer setup connects a Keithley 2002 multimeter to measure the voltage drop V_{shunt} at each of the seven shunt resistors. A measurement frequency of ~ 0.5 Hz was obtained using this setup. The measured voltage drops at the shunt resistors were used to calculate the resistance of the respective chemiresistor sample according to equation A.1

$$R_{\text{Sensor}} = \frac{V_{2601A} - V_{\text{Shunt}}}{V_{\text{Shunt}}/R_{\text{Shunt}}} \quad (\text{A.1})$$

Here, R_{Sensor} is the resistance of the sensor sample, V_{2601A} is the voltage provided by the Keithley 2601A. V_{Shunt} and R_{Shunt} are the voltage measured at the shunt resistor and the resistance of the shunt resistor, respectively.

A.7 Response Isotherms and Response Transients of Fully Printed Chemiresistors

Figure A.6 a)–g) shows the response isotherms of all fully printed chemiresistors to all used analyte vapors. The insets show linear fits to the data points at concentrations of 25, 50 and 100 ppm, which were used to obtain the sensitivities depicted in figure 7.13 b). The slopes are forced through the origin (0/0) and are shown as dashed lines.



(a)

Figure A.6: Response isotherms of sensors. a) S-9DT, b) S-TG.25, c) S-TG.50, d) S-3MPA.25. Adapted with permission from Ref. [81]

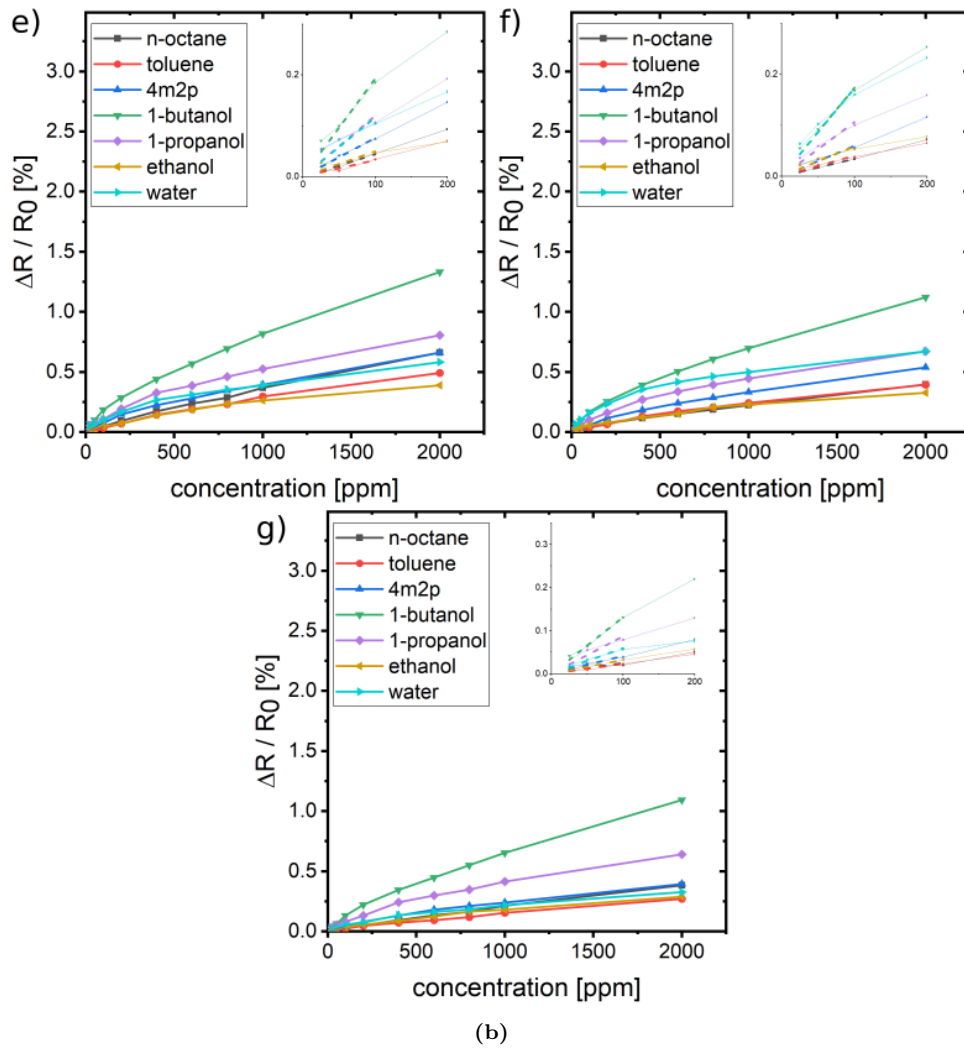


Figure A.6: Response isotherms of sensors. e) S-3MPA.50, f) S-4M1OH.25, g) S-4M1OH.50. Adapted with permission from Ref. [81]

Figure A.7 shows the response transients of all chemiresistors to analyte vapors at the concentration 100 ppm.

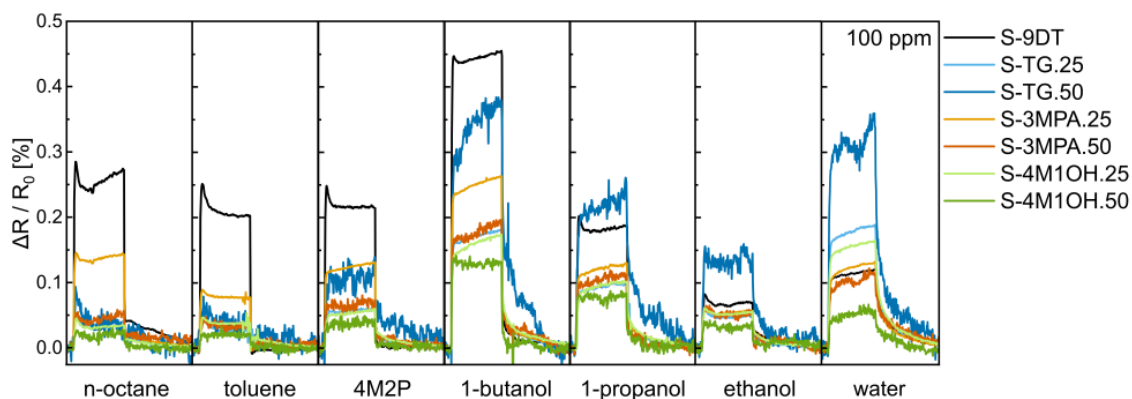


Figure A.7: Response transients of all sensors used in this work to analytes at a concentration of 100 ppm. Adapted with permission from Ref. [81].

A.8 Stress/Strain Curves

Figure A.8 and A.9 depict all stress strain curves used to obtain mean values for the critical strain and stress parameters shown in figure 7.17 as well as for the toughnesses of the nanomembranes presented in this work.

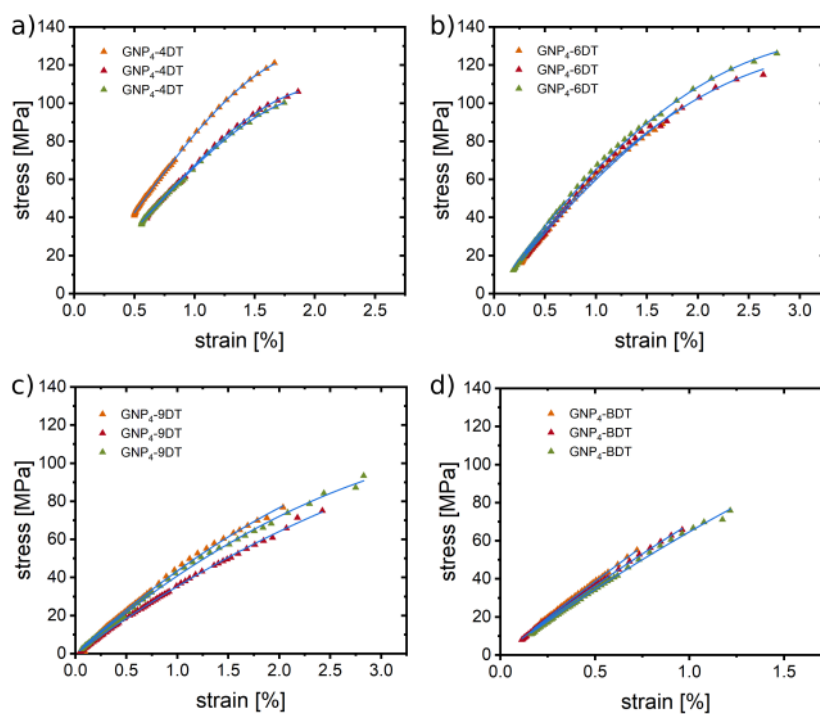


Figure A.8: Plots showing the stress/strain curves obtained for the $\text{GNP}_{4\text{nm}}$ particle system with different ligands. a) 4DT. b) 6DT. c) 9DT. d) BDT. The solid blue lines depict polynomial fits used for the calculation of toughnesses.

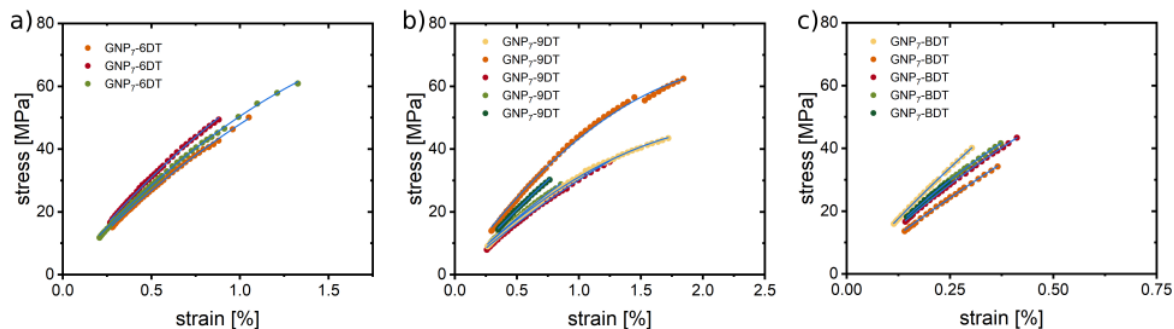


Figure A.9: Plots showing the stress/strain curves obtained for the GNP_{7nm} particle system with different ligands. a) 6DT. b) 9DT. c) BDT. The solid blue lines depict polynomial fits used for the calculation of toughnesses.

A.9 Validation of Climate Chamber Parameters

As can be seen from figure A.10 c), the properties of the GNPs show large deviations depending on which climate chamber (WKL34/40 or HCP50) was used to artificially age the particle systems. For each climate chamber two freshly prepared GNP_L-based samples were used to be aged for seven days (WKL_{1,2} and HCP_{1,2}, respectively). To validate that the temperature and humidity parameters for the artificial aging experiments were set correctly by the climate chamber, a commercially available temperature and humidity sensor (BME680, Bosch) was inserted in the climate chambers and both parameters were tracked for 24 h. The climate chambers were both set to 85 %rH and 85 °C. Figure A.10 a) and b) show that both parameters were set fairly well by the climate chambers with short readjustments periods. The values measured with the commercial sensor were increased by ~2 %rH and 2 °C, which is probably due to the fact, that this sensor was operated at its operating limits. Though the aging behavior obviously depends on the climate chamber used, the changes in conductivity for the freshly prepared GNP_L sample aged in the WKL34/40 (figure A.10 c) are similar to the values presented in the main document (cf. figure 7.19 b). Though a good reproducibility could be achieved for samples aged in the WKL34/40 climate chamber, these measurements, however, show, how highly complex the aging process of such GNP composites is.

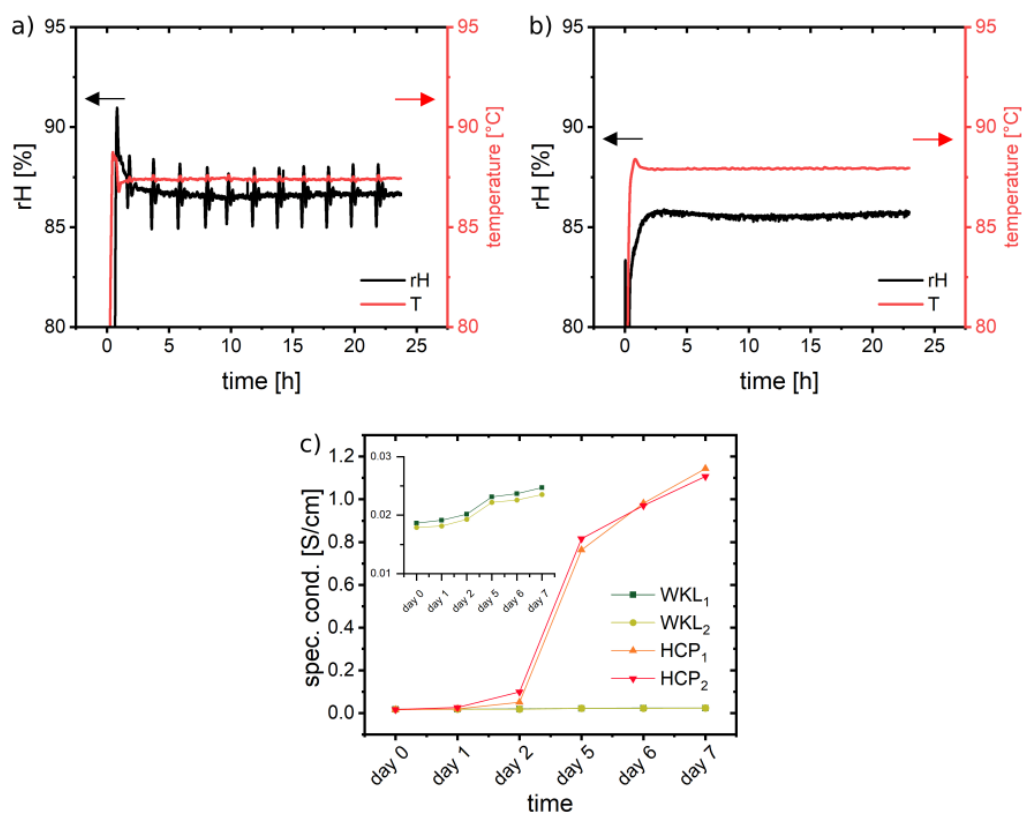


Figure A.10: Validation of climate chamber parameters at 85/85 conditions with a commercial temperature and humidity sensor (BME 680) and comparison of IV-measurements performed under 65/65 aging conditions in different climate chambers. *a)* Climate chamber parameters of WKL34/40. *b)* Climate chamber parameters of HCP50. *c)* Specific conductivities for freshly prepared GNP_L -based samples aged in the WKL34/40 and HCP50 climate chamber. The two samples aged in the HCP50 chamber exhibit greatly increased specific conductivities compared to the samples aged in the WKL34/40 climate chamber.

A.10 Informed Consent Form Template for Research with Human Participants

Informed consent form template for research with human participants

Information Sheet

1. Purpose of the research

The purpose of this work including human participants, is, to work on novel nanocomposite material sensors. These sensors should be checked on their applicability to be used as pulse wave and muscle motion detection sensors. The prototypes used in this study are all non-invasive sensors and are attached to the skin surface. For fixation of such sensors medical tape or wristbands are used. The sensor parts that get in contact with the skin are of skin-friendly polymer material. Polymers used are Dragon-Skin™ silicone and polydimethylsiloxane (PDMS). Both polymers are proven to be skin-friendly.[1,2] The sensors are finally connected via small cables to a voltage source and drained a maximum current of 1 μ A.

Videos of the working principle of the sensors will only include a close up zoom on the skin area where the sensor is attached to.

2. Benefits and risks of participating

As a benefit the participant helps to prove the working principle of such novel sensor probes to promote future applications as human health care devices.

As a risk, participants might suffer from intolerances to used polymers attached to the skin.

3. Withdrawal from the study

Any participant may withdraw his/her consent from the participation of the study by informing the authors in writing any time.

4. Collection of data

All data will be collected and saved digitally anonymously containing no relation to the participants the measurements were conducted with. All participants have the right to demand for the access and irreversible deletion of the collected data at any time.

5. Retention period

If not demanded otherwise the collected data will be retained for 10 years after recording until it will automatically be deleted irreversibly.

6. Contact Details of project supervisor

Dr. Tobias Vossmeier
Institut für Physikalische Chemie
Universität Hamburg
Grindelallee 117
D-20146 Hamburg
Germany
Phone: +49 40 42838-7069
email: tobias.vossmeier@chemie.uni-hamburg.de

7. References

[1] <http://www.ampolymer.com/SDS/PolydimethylsiloxaneSDS.html>, see section 11., last checked 06.12.2021.

[2] <https://www.smooth-on.com/tb/files/SkinSafeDocs/DragonSkinFX-ProSkinSafeCertification071519.pdf>, last checked 06.12.2021.

B Safety

Table B.1 lists the chemicals used in this study including their classification according to the globally harmonized system (GHS) as well as hazard and precautionary statements.

Table B.1: List of chemicals and GHS classifications.

Chemical	GHS symbol	Hazard Statements	Precautionary Statements
Aceton		H225, H319, H336	P210, P261, P305 + P351 + P338
1-Dodecylamine		H302, H314, H410	P273, P280, P305 + P351 + P338, P310, P501
1-Dodecanethiol		H314, H410	P273, P280, P305 + P351 + P338, P310, P501
1-Hexadecanethiol	(1)		
1,9-Nonanedithiol		H315, H319, H335	P261, P305 + P351 + P338
1,6-Hexanedithiol	(1)		
1,4-Butanedithiol	(1)		
1,4-Benzenedithiol	(1)		
Chloroauric acid		H314, H317	P280, P301 + P330 + P331, P302 + P352, P305 + P351 + P338, P309, P310
Ethanol		H225, H302, H371	P261, P305 + P351 + P338

Table B.1: List of chemicals and GHS classifications.

Chemical	GHS symbol	Hazard Statements	Precautionary Statements
Tetraoctyl-ammonium-bromide		H315, H319, H335	P261, P305 + P351 + P338
Sodium borohydride		H260, H301, H311, H314	P223, P231, P232, P280, P301 + P310, P370 + P378, P422
Sodium hydroxide		H314	P280, P305 + P351 + P338, P310
n-Heptane		H225, H304, H315, H336, H410	P210, P261, P273, P301 + P310, P331, P501
1-Propanol		H225, H318, H336	P210, P261, P305 + P351 + P338
2-Propanol		H225, H319, H336	P210, P261, P305 + P351 + P338
Toluene		H225, H304, H315, H336, H361d, H373	P210, P240, P280, P361, P281, P301 + P310 + P330, P302 + P352, P331, P403 + P233
Oleylamine		H302, H314, H335, H373, H304, H410	P260, P280, P301 + P310, P303 + P361 + P353, P261, P305 + P351 + P338, P405
4-Methylpentan-2-one		H255, H319, H332, H335	P210, P261, P305 + P351 + P338
Chlorobenzene		H226, H332, H315, H411	P260, P262, P273, P403

Table B.1: List of chemicals and GHS classifications.

Chemical	GHS symbol	Hazard Statements	Precautionary Statements
Methanol		H225, H331, H311, H301, H370	P210, P233, P280, P302 + P352, P304 + P340, P308 + P310, P403 + P235
Poly(methyl methacrylate)	(1)		
Hydrogen Peroxide		H271, H302, H314, H332, H335, H412	P280, P305 + P351 + P338, P310
Sulfuric Acid		H314	P260, P264, P280, P301 + P330 + P331, P303 + P361 + P353, P304 + P340, P305 + P351 + P338, P310, P321, P363, P405, P501
SYLGARD 184 Silicone Elastomere Kit (Base)	(1)		
SYLGARD 184 Silicone Elastomere Kit (Curing Agent)	(1)		
Dragon Skin silicon polymer	(1)		
Tert-butylamine borane complex		H301 + H311, H315, H319, H411	P264, P273, P280, P301 + P302 + P352 + P312, P305 + P338
4-Mercapto-1-butanol		H315, H319, H335	P261, P305 + P351 + P338

Table B.1: List of chemicals and GHS classifications.

Chemical	GHS symbol	Hazard Statements	Precautionary Statements
3-Mercaptopro- pionic acid		H290, H301, H314, H332	P234, P261, P280, P303 + P361 + P353, P304 + P340 + P310, P305 + P351 + P338
1-Thioglycerol		H302, H311, H315, H317	P280, P301 + P312 + P330, P302 + P352 + P312
n-Octane		H225, H304, H315, H336, H410	P210, P233, P273, P301 + P310, P303 + P361 + P353, P331
1-Butanol		H226, H302, H315, H318, H335, H336	P210, P233, P280, P301 + P312, P303 + P361 + P353, P305 + P351 + P338
Ammonium Solu- tion		H290, H314, H335, H410	P273, P280, P303 + P361 + P353, P305 + P351 + P338, P310
AZnLOF 2020		H225, H318, H334	P210, P243, P280
AZ 726 MF		H290, H302 + H312, H314, H371, H373	P260, P280, P308 + P311, P362 + P364
potassium iodide	(1)		
iodine		H312 + H332, H315, H319, H335, H372, H400	P273, P302 + P352, P305 + P351 + P338, P314
triammonium cit- rate		H315, H319, H335	P261, P305 + P351 + P338
TechniStrip NI555	-	H302, H312	-

(1) Not a hazardous substance or mixture according to Regulation (EC) No. 1272/2008. This substance is not classified as dangerous according to Directive 67/548/EEC.

Table B.2 lists all substances classified as cancerogenic, mutagenic or toxic to reproduction (CMR).

Table B.2: List of CMR classified substances.

Substance	CMR classification	Usage and amount
Sodium borohydride	R _f category 1B	reductant, 2g
Toluene	R _D category 2	solvent, 2L

C Danksagung

Zunächst möchte ich Herrn Prof. Dr. Horst Weller dafür danken, dass ich so freundlich in seine Arbeitsgruppe aufgenommen wurde und unter exzellenten Arbeitsbedingungen forschen konnte.

Des Weiteren gilt mein Dank Dr. Tobias Vossmeier für seine ausgezeichnete Betreuung meiner Doktorarbeit, sein stets offenes Ohr, die wertvollen Diskussionen und Anregungen sowie die vielen netten Gespräche. Außerdem möchte ich mich für die Übernahme des Erstgutachtens bedanken.

Herrn Prof. Dr. Alf Mews danke ich für die Übernahme des Zweitgutachtens.

Martina Krasa, Sigrid Zeckert und Marion Manin möchte ich für ihre stete Hilfsbereitschaft bei jeglichen organisatorischen Fragestellungen danken.

Außerdem gilt mein Dank meinem Masterstudenten Patrick Tjarks und meinen Bachelorstudenten Verena Schulze und Piet Hassenstein für ihre tatkräftige und erfolgreiche Unterstützung bei einer Vielzahl von Projekten.

Ich möchte mich ebenso bei der "Sensor-Gruppe" bedanken und besonders Hauke Hartmann, Dr. Hendrik Schlicke und Sophia Bittinger erwähnen. Diese standen mir in Beruf und Freizeit zuverlässig mit anregenden Diskussionen und ihrer Hilfsbereitschaft zur Seite und hatten auch abgesehen davon stets Zeit für mich.

Für die Unterstützung bei Problemen im Bereich Elektronik und Informatik möchte ich Hendrik Schlicke und Jan Flügge danken, Ersterem vor allem auch für seine Hilfsbereitschaft beim Optimieren diverser Experimentalaufbauten. Bedanken möchte ich mich weiterhin bei den Mitarbeitern der Forschungswerkstatt der Physikalischen Chemie um Siegfried Uselis für die Anfertigung diverser Prototypen und Apparaturen, ohne die diese Arbeit in diesem Umfang nicht hätte entstehen können.

Ferner gilt mein Dank Stefan Werner, Robert Schön, Andreas Kornowski und Almut Barck für die Anfertigung diverser elektronenmikroskopischer Aufnahmen und die Aufnahme von Röntgendiffraktogrammen.

Dr. Heshmat Noei und Dr. Michael Wagstaffe danke ich für das Durchführen der XPS Messungen, Dr. Andreas Meyer für die Durchführung der SAXS Messungen.

Für die Durchsicht dieser Arbeit möchte ich mich bei Hendrik Schlicke und Sophia Bittinger bedanken.

Meinen Kollegen Hauke Hartmann, Finn Dobschall und Roger Wu gilt für die angenehme

Zeit in Büro 347 ebenfalls mein Dank.

Für viele unterhaltsame Stunden und jede Menge Spaß möchte ich den ehemaligen Mitgliedern Gregor, Maik, Jil, Michael, Rieke, Daniel, Marius, Mazlum, Lasse, Markus und Clemens herzlich danken sowie den aktuellen Mitgliedern Lea, Sönke, Artur, Agnes, den beiden "Sebastianen", Steffen, Felix, Julian, Julia, Finn, Sophia, Svenja, Jana, Nancy, Elena, Ahir und Kathrin und dem gesamten AK Weller.

Für das Heranführen an das Dartspielen möchte ich mich beim Team TTS um Jan Niehaus, Sören Becker, Hauke Heller und Stefan Werner bedanken.

Schließlich möchte ich für die uneingeschränkte Unterstützung in allen Belangen auch meine Eltern Rosi und Hauke Ketelsen in meiner Danksagung nicht vergessen.

D Eidesstattliche Versicherung

Hiermit versichere ich an Eides statt, die vorliegende Dissertation selbst verfasst und keine anderen als die angegebenen Hilfsmittel benutzt zu haben. Die eingereichte schriftliche Fassung entspricht der auf dem elektronischen Speichermedium. Ich versichere, dass diese Dissertation nicht in einem früheren Promotionsverfahren eingereicht wurde.

Bendix Ketelsen

Hamburg, den 21. August 2022